



Review

Graphitic carbon nitride (g-C₃N₄) nanocomposites: A new and exciting generation of visible light driven photocatalysts for environmental pollution remediation



G. Mamba*, A.K. Mishra

Nanotechnology and Water Sustainability Research Unit, College of Science, Engineering and Technology, University of South Africa, Florida 1709, Johannesburg, South Africa

ARTICLE INFO

Article history:

Received 5 March 2016

Received in revised form 18 May 2016

Accepted 21 May 2016

Available online 28 May 2016

Keywords:

Graphitic carbon nitride

Heterostructures

Photocatalysis

Z-scheme mechanism

Nanostructures

ABSTRACT

Engineering photocatalytic materials for renewable energy generation and environmental decontamination has always been a very exciting prospect to counter the global energy demands and pollution challenges. Graphitic carbon nitride (g-C₃N₄), a polymeric, metal-free semiconductor with a mild band gap (2.7 eV) has become hot-spot in various scientific exploits such as environmental pollution mitigation, energy generation and storage, organic synthesis, sensors, etc. These applications exploit the interesting properties of g-C₃N₄ such as good visible light absorption, graphene-like structure, good thermal and chemical stability and photocatalytic properties. In this review we begin with an overview of the fundamental aspects of photocatalysis as a pollution remediation strategy. This is followed by an introduction to graphitic carbon nitride as a photocatalyst, preparation strategies and its properties. Subsequently, a comprehensive and critical discussion of the various most recent developments towards enhancing the visible light photocatalytic properties of g-C₃N₄ for pollution alleviation, selected results and important photocatalytic degradation mechanisms, is given. Summary remarks and future perspective conclude the review.

© 2016 Published by Elsevier B.V.

Contents

1. Introduction	348
1.1. Basic principles of photocatalysis	348
1.2. Mechanism of hydroxyl radical attack on organic pollutants	348
1.3. Key steps during pollutant degradation	349
2. G-C ₃ N ₄ as a photocatalyst	350
2.1. Modification of g-C ₃ N ₄ for improved photocatalytic activity	351
2.2. Metal decorated/doped g-C ₃ N ₄ (g-C ₃ N ₄ -M) nanostructures	352
2.3. Non-metal doped g-C ₃ N ₄ (g-C ₃ N ₄ -X) nanostructures	355
2.4. Coupling g-C ₃ N ₄ with carbon nanomaterials (g-C ₃ N ₄ /CNM heterojunctions)	357
2.5. Coupling g-C ₃ N ₄ with other semiconductors	359
2.5.1. Binary nanocomposites (g-C ₃ N ₄ /MO heterojunctions)	359
2.5.2. Ternary nanocomposites	365
3. Summary remarks and perspective	372
Acknowledgement	373
References	373

* Corresponding author.

E-mail address: gcmamba@gmail.com (G. Mamba).

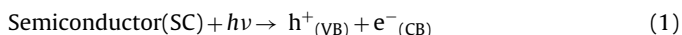
1. Introduction

Semiconductor photocatalysis is a fast emerging advanced oxidation process for organic pollution abatement and possess several advantages over other oxidation tools. One of the merits of this process is the provision of a fixed reaction environment by the photocatalyst surface on which a wide range of adsorbed organic and inorganic species can be chemically altered *via* light induced redox reaction. Moreover, the semiconductor which catalyses these redox reactions is often stable towards photolysis which allows for multiple oxidative conversions per active site of the photocatalyst [1,2]. Other advantages of semiconductor photocatalysis include the absence of fouling, lack of mass transfer limitations, applicability at ambient conditions (temperature and pressure) and ability to completely mineralise many organic pollutants into carbon dioxide, water and inorganic ions [3–7]. In textile effluent treatment where its toxicity hamper the applicability of biodegradation, semiconductor photocatalysis is immune to this toxicity. Furthermore, during degradation of azo dyes, the formed aromatic amines can be further degraded on the photocatalyst into carbon dioxide, water and inorganic ions [8,9].

1.1. Basic principles of photocatalysis

During photocatalysis, the semiconductor (photocatalyst) absorbs energy ($h\nu$) equal or above its band gap energy (E_g) leading to the excitation of electrons from the valence band (VB) to the conduction band (CB) of the semiconductor. At absolute zero, the valence band is fully occupied with electrons and has lower energy while the conduction band is empty and possesses higher energy [2,10–12]. The size of the band gap which is the energy gap (barrier) between the valence and the conduction bands of the semiconductor determines its optical properties and colour. For example, semiconductors with band gaps between 1.5 eV and below 3.0 eV absorb energy in the visible light region and have colours ranging from red to violet [10]. Some selected common semiconductors and their corresponding band gaps are presented in Table 1.

Following photoexcitation of the electrons, positive holes are created in the valence band and electrons occupy the conduction band. Subsequently, the valence band acquires a positive charge and it is oxidising while the conduction band attains a negative charge and it is reducing [7,16–19]. The photoexcitation reaction is depicted in Eq. (1).



There are a number of possible scenarios that could unfold following the generation of the electron/hole pairs. One of the most undesirable scenarios is the recombination of the generated charge carriers which occurs very fast (in nanoseconds) following photoexcitation. The holes and the electrons may recombine releasing the absorbed energy as heat and/light [3,7,11,16,20,21]. Of the photogenerated electron/hole pairs, up to 90% can recombine very fast (in less than 10 ns) resulting in fewer charge carriers available for the surface reactions [18]. This leads to poor photoactivity of the semiconductor. Alternatively, the electrons are trapped in defect

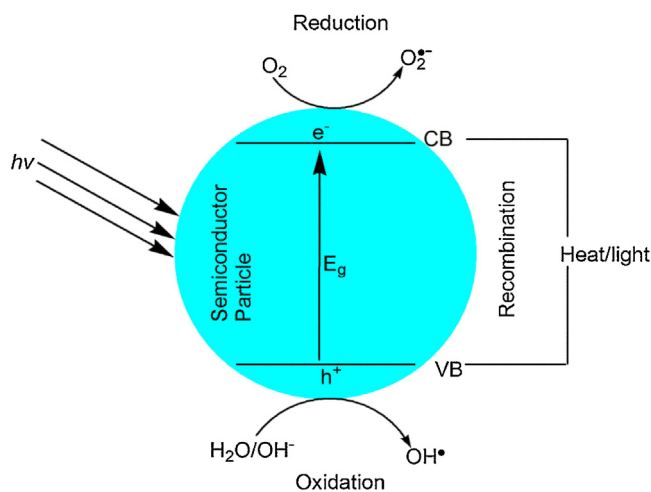


Fig. 1. Fate of the electron-hole pair following photoexcitation.

sites or surface states of slightly lower energy than the conduction band of the semiconductor particle [22,23]. This ensures separation of the charge carriers, availing them for the surface redox reactions. In an ideal scenario, the holes and electrons partake in redox reactions with electron acceptors and donors adsorbed on the semiconductor surface [18,24]. Reduction and oxidation of organic molecules adsorbed on the surface of the semiconductor by electrons and holes proceed *via* interfacial charge transfer to yield the radical species [23]. A simplified schematic showing the fate of the electron-hole pairs subsequent to excitation is illustrated in Fig. 1.

Basically, the valence band holes capture hydroxide ions (OH^-) or water (H_2O) to form the extremely powerful, non-selective, oxidising hydroxyl radical (OH^\bullet). Accordingly, the conduction band electrons are trapped by molecular oxygen (O_2) to form the superoxide radical ($\text{O}_2^{\bullet -}$), another important oxidising agent [25–31]. The hydroxyl and superoxide radicals partake in the degradation of the organic pollutants into carbon dioxide, water, and inorganic ions. Scavenging of the electrons by oxygen to yield the superoxide radical is a very important step which produces the oxidising species while also suppressing electron/hole recombination. This prolongs the life of the holes, leading to the formation of the hydroxyl radicals [22,32,33]. The various reactions responsible for the formation of these oxidising species are depicted in Eq. (2)–(8) and depends on the valence and conduction band potential positions relative to the redox potentials of the surface reactions. For example, if the oxidation potential of the surface reaction is more positive than the valence band potential, then oxidation cannot be accomplished. Likewise, if the reduction potential of the surface reaction is more negative than the conduction band, reduction will not be achieved [2]. This implies that there will be no formation of the hydroxyl and superoxide radicals from the valence band and conduction band, respectively.

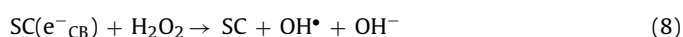
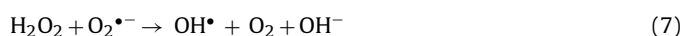
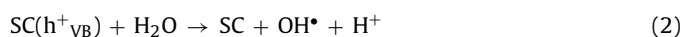


Table 1

List of selected semiconductors and their band gaps. [10,13–15].

Semiconductor	Band gap (eV)	Semiconductor	Band gap (eV)
Fe_2O_3	2.3	CdSe	1.7
CdS	2.5	$\text{g-C}_3\text{N}_4$	2.7
WO_3	2.8	Cu_2O	2.2
TiO_2 (rutile)	3.0	V_2O_5	2.4
TiO_2 (anatase)	3.2	CeO_2	2.94
ZnO	3.2	ZnS	3.6
SnO_2	3.5	SiC	3.0

Table 2
Oxidation potentials of some oxidising species. [36].

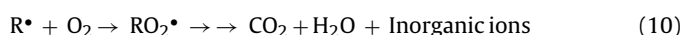
Oxidant	Oxidation potential (V_{NHE})	Oxidant	Oxidation potential (V_{NHE})
Fluorine	3.03	Hypobromous acid	1.59
Hydroxyl radical	2.80	Chlorine dioxide	1.57
Atomic oxygen	2.42	Hypochlorous acid	1.49
Ozone	2.07	Hypoiodous acid	1.45
Hydrogen peroxide	1.78	Chlorine	1.36
Perhydroxyl radical	1.70	Bromine	1.09
Permanganate	1.68	Iodine	0.54

1.2. Mechanism of hydroxyl radical attack on organic pollutants

The hydroxyl radical is the second strongest oxidising species after fluorine. Its strong oxidation potential ($E_{\text{ox}} = +2.8 V_{\text{NHE}}$) and non-selective nature enables it to oxidise a wide range of organic compounds including dyes which have a complex and stable structure. Table 2 gives the oxidation potentials of some common oxidising agents including ozone, atomic oxygen, chlorine and hydrogen peroxide with all having lower oxidation potentials than the hydroxyl radical. During photocatalysis, both the superoxide and hydroxyl radicals are important and they complement each other [2,23,34,35]. The superoxide radical can either oxidise the organic pollutants directly or undergo further reactions to form the hydroxyl radical as depicted in Eq. (7).

The degradation of organic compounds by the hydroxyl radical proceeds can either through hydrogen abstraction, electrophilic attack or electron transfer. However, hydrogen abstraction has been highlighted as the most common route for degradation of organic compounds [21,37]. During hydrogen abstraction, hydrogen is removed from the organic compound to form an organic radical as shown in Eq. (9). Subsequent reaction with oxygen, transforms the organic radical to peroxy radical. These peroxy radicals undergo a series of thermal reactions of oxidative degradation, leading to the complete mineralisation of the organic compound to carbon dioxide, water and inorganic salts (Eq. (10)) [21,36]. Electrophilic addition is another proposed mechanism whereby the hydroxyl radical is added to the organic compound's π -system to form the organic radical (Eq. (11)). In cases where hydrogen abstraction or electrophilic addition is unfavourable due to multiple halogen substitution or steric hindrance, electron-transfer is a possible route for initiating degradation of the organic compound. The hydroxyl radical is reduced to hydroxide ions by the organic compound while forming the organic radical (Eq. (12)) [36]. Thereafter, the organic radical undergoes the transformations depicted in Eq. (10). In addition to radical attack on organic compounds, direct

reduction by the conduction band electrons (Eq. (13)) and oxidation by the valence band holes (Eq. (14)) has been reported as other possible routes through which degradation of organic pollutants such as dyes is initiated during semiconductor photocatalysis [9,16,38].



Minimising recombination is the ultimate goal in any photocatalytic application which leads to efficient formation of the radical species and higher photocatalytic performance. Higher rates of recombination result to loss of the reactive species responsible for formation of the radical species, thereby lowering the photocatalytic activity, considerably. As a surface process, semiconductor photocatalysis requires both the electron donor and acceptor to be in contact with the photocatalyst [39–41]. Intimate contact between the photocatalyst and the electron donor/acceptor ensures efficient charge transfer and minimises recombination. A number of strategies have been exploited in order to improve charge transfer at the semiconductor/electrolyte interface. Such strategies include modification of the semiconductor surface with electron acceptors, electrostatic incorporation of the electron acceptors on the semiconductor surface and supporting photocatalysts in redox functionalised polymers [39,42–45].

1.3. Key steps during pollutant degradation

Semiconductor photocatalysis is a very complex process involving a lot of possible reaction pathways responsible for the eventual

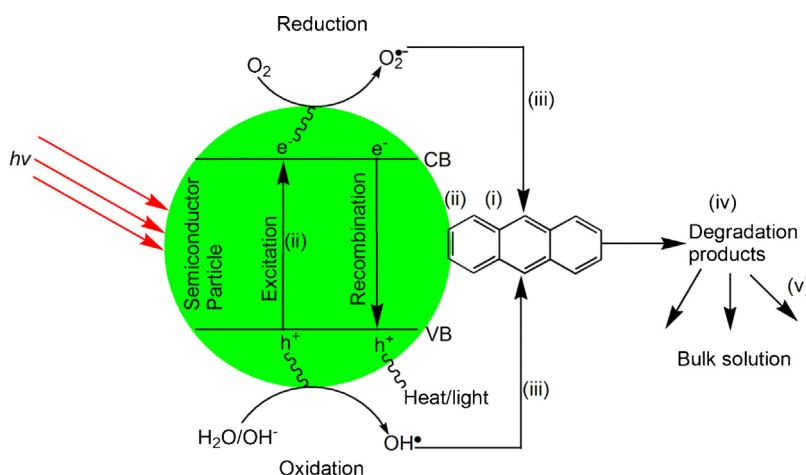


Fig. 2. Key steps in semiconductor photocatalysis.

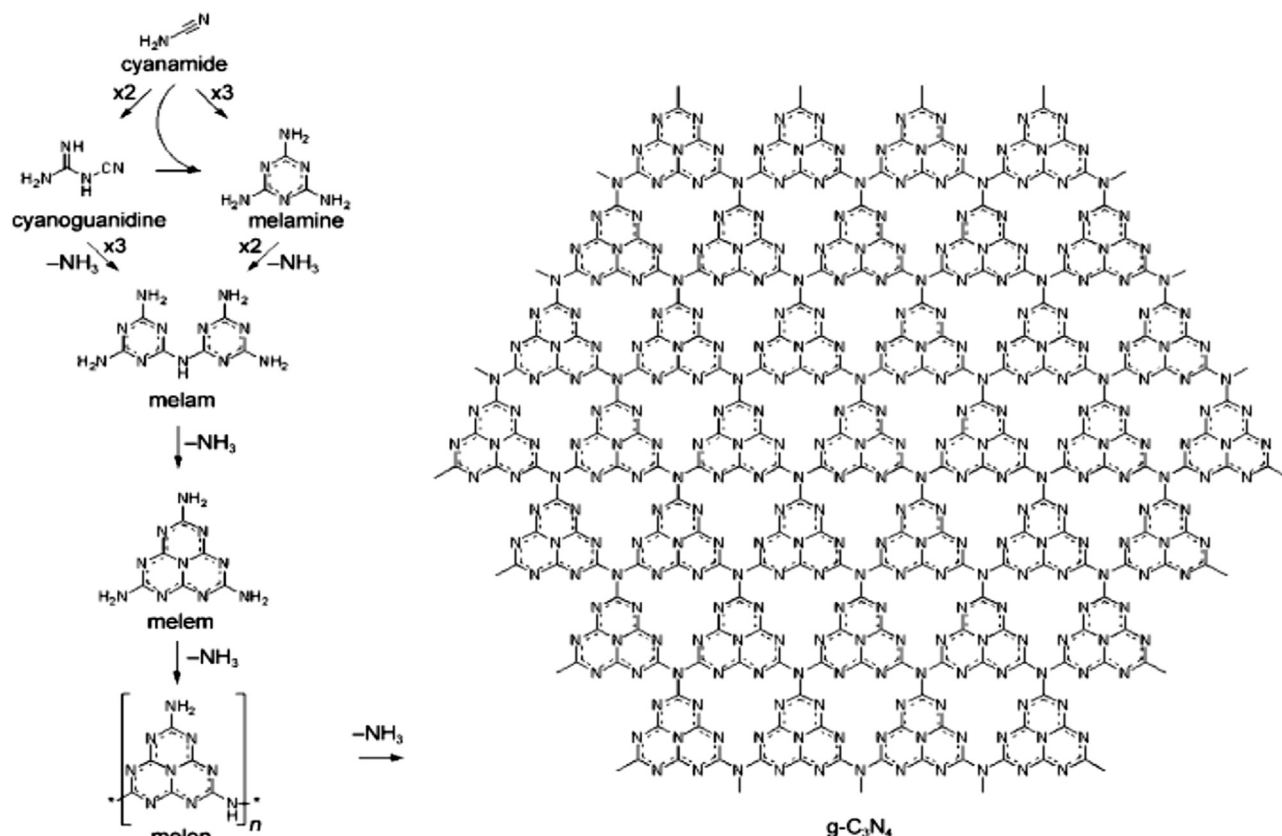


Fig. 3. Condensation sequence of cyanamide to form g-C₃N₄.

Reproduced with permission from Ref. [94]. Copyright 2008, Wiley.

decomposition of the pollutants. However, there is a general consensus that the process can be summarised into five key steps (Fig. 2) leading to the degradation of the organic pollutants. The first step is mass transfer of the organic pollutants through diffusion from then bulk solution onto the surface of the semiconductor (step (i)). In the second step there is simultaneous adsorption of the organic pollutant to the semiconductor surface and excitation of the semiconductor (step (ii)). This is followed by the degradation of the organic compound by the oxidising species (step (iii)). Subsequently, desorption of the degradation products from the photocatalyst's active surface occurs (step (iv)). Lastly, the degradation products diffuse from the photocatalyst interface into the bulk solution (step (v)) [25,46,47]. Notably, the overall degradation rate depends on the slowest step in the process [47]. For example, regardless how fast the adsorption of the organics on the semiconductor (ii) and their degradation (iii), if the desorption of the degradation products (iv) and their diffusion into the bulk solution (v) is slow, the whole process will depend on these two steps (iv and v).

2. G-C₃N₄ as a photocatalyst

Titanium dioxide (TiO₂) has over the years dominated research in various photocatalytic applications such as environmental pollution mitigation, hydrogen production from water splitting, solar cells, etc. However, its inherent wide band gap and high recombination rate of the photogenerated charge carriers have been lingering obstacles hindering the large scale, practical exploitation of this material. Consequently, a considerable amount of research effort has been channelled towards TiO₂ band gap engineering to improve charge separation and extend its response into the visible light region, while also searching for alternative visible light driven pho-

tocatalysts. Successful tailoring of such materials would allow the utilisation of sunlight as a source of energy to drive the photocatalytic processes. For the past few years, graphitic (graphite-like) C₃N₄ (g-C₃N₄), a 2-D π -conjugated polymeric, metal-free, mild band gap (2.7 eV) semiconductor has emerged as an attractive material for various scientific applications [48–50]. In 2015 alone, a host of publications on g-C₃N₄ and g-C₃N₄ heterostructures have emerged in a number of fields such as sensors [51–53], supercapacitors [54,55], adsorption [56–58], organic synthesis [59,60], hydrogen evolution from water splitting [61–64], photocatalytic degradation of microbial, organic and inorganic pollutants [65–68], bioimaging [69], oxygen reduction reactions [70,71], lithium-ion batteries [72,73] biofuel cells [74], lubrication [75], photo-chemo combination therapy [76], additive in FO membranes [77], etc.

Although C₃N₄ in the form of melon is one of the oldest synthetic polymers reported dating back in 1834 [78], research on this material remained dormant for over 150 years until Cohen and Liu predicted an ultra-hard material (harder than diamond) based on the β -Si₃N₄ structure where Si is substituted for C to form β -C₃N₄ [79]. Inspired by this work, Niu and Cohen successfully synthesised β -C₃N₄ via pulsed laser ablation which appeared to be a mixture of an amorphous and crystalline solid and showed good adhesion to both silicon and nickel substrates, superb hardness and high thermal stability [80]. There are several allotropes of C₃N₄ such as α -C₃N₄, β -C₃N₄, pseudocubic C₃N₄, cubic C₃N₄ and g-C₃N₄ [81,82]. However, g-C₃N₄ is considered as the most stable form of C₃N₄ under ambient conditions [83].

Several methods have been explored for the preparation of g-C₃N₄ with different architectures and electronic properties. Such methods include chemical vapour deposition (CVD), solvothermal, physical vapour deposition (PVD), ionothermal synthesis, single step nitridation, solid state, sonochemical and thermal conden-

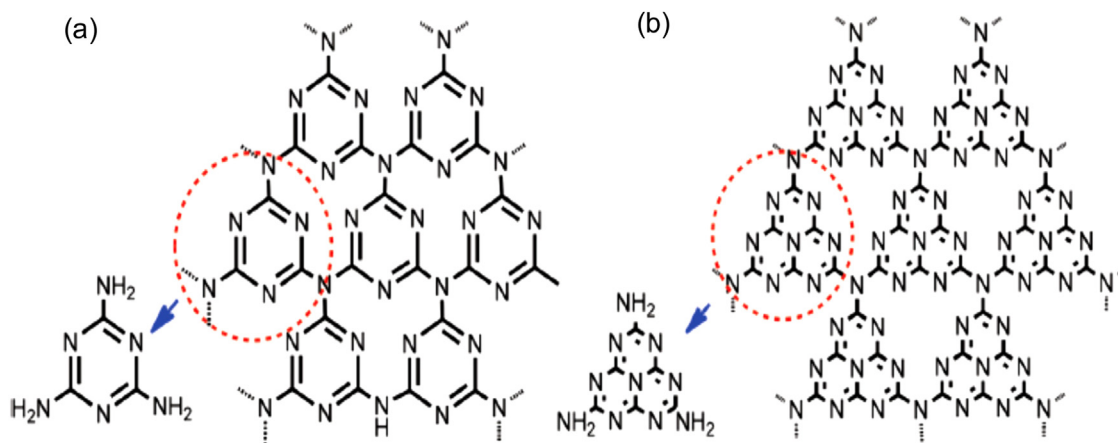


Fig. 4. Structure of (a) *s*-triazine and *s*-triazine based $g\text{-C}_3\text{N}_4$ and (b) tri-*s*-triazine and tri-*s*-triazine based $g\text{-C}_3\text{N}_4$. (For interpretation of the references to colour in the text, the reader is referred to the web version of this article.)

Reproduced with permission from Ref. [97]. Copyright 2014, RSC.

sation [84–87]. However, thermal condensation of nitrogen-rich precursors such as urea, cyanamide, dicyanamide, melamine, thiourea, trithiocyanuric acid, guanidine hydrochloride, triazoles, *etc.* has been the most attractive method for preparation of $g\text{-C}_3\text{N}_4$ due its simplicity and use of cheap, readily available precursors [88–93]. The transformation of the nitrogen-rich precursors to $g\text{-C}_3\text{N}_4$ has been proposed starting from cyanamide (Fig. 3) which condenses to dicyanamide then melamine. This is followed by loss of ammonia and polycondensation to form melam which is transformed into melem after loss of ammonia. Further polycondensation yields the polymeric melon, which undergoes rearrangement and polycondensation to yield $g\text{-C}_3\text{N}_4$ [85,94–96].

The stacked 2-dimensional architecture of $g\text{-C}_3\text{N}_4$ can be pictured as a graphite framework in which a nitrogen heteroatom has been substituted, consisting of π -conjugated graphitic planes formed by sp^2 hybridised carbon and nitrogen [97]. As a graphite analogue, the interlayer distance is smaller in $g\text{-C}_3\text{N}_4$, resulting in a more dense packing compared to graphite [98]. Both *s*-triazine (Fig. 4a, red circle) and tri-*s*-triazine (Fig. 4b, red circle) were thought as the building blocks of $g\text{-C}_3\text{N}_4$ giving rise to two possible forms of $g\text{-C}_3\text{N}_4$ with different degrees of stability. One form is based on condensed *s*-triazine units as the tectonic units (Fig. 4a) while the other form is built from tri-*s*-triazine as the fundamental units which are connected via planar tertiary amines (Fig. 4b) [85,90,98]. Although both forms of $g\text{-C}_3\text{N}_4$ can be prepared, it has been predicted from density functional theory (DFT) calculations that the structure based on tri-*s*-triazine units is more thermodynamically stable (30 kJ more stable) than the *s*-triazine based structure owing to the higher stability of the tri-*s*-triazine units [99]. Therefore, the tri-*s*-triazine is generally accepted as the tectonic unit for $g\text{-C}_3\text{N}_4$.

$g\text{-C}_3\text{N}_4$ has emerged as an attractive visible light driven photocatalyst, showing better visible light absorption than most metal oxide photocatalyst owing to its mild band gap (2.7 eV) [100,101]. Moreover, its band potentials are well suited for water splitting under visible light irradiation, making it an ideal candidate for renewable energy generation [102–104]. The polymeric nature of this material allows for multiple excitations from absorption of a single photon, leading to efficient generation of the reactive species responsible for pollutant degradation [105]. $g\text{-C}_3\text{N}_4$ possess fascinating chemical and thermal stability. It shows significantly high resistance to acidic and basic media and insoluble in a number of common solvents such as ethanol, water, tetrahydrofuran, toluene and diethyl ether. This chemical resistance emanates from the Van der Waals forces holding together the stacked graphitic

layers [106]. In terms of thermal stability, $g\text{-C}_3\text{N}_4$ is stable up to 600 °C and completely decomposes at 700 °C [106]. Furthermore, $g\text{-C}_3\text{N}_4$ is inexpensive, non-toxic, can easily be fabricated from readily available precursors and its polymeric structure allows for easy modification to improve its optical and electronic properties [107–110].

Despite all the interesting electronic and optical properties of $g\text{-C}_3\text{N}_4$, its photocatalytic activity remains unconvincing for practical applications owing to low efficiency of visible light utilisation, high recombination rate of the photo generated charge carriers, low electrical conductivity and smaller specific surface area ($<10\text{ m}^2\text{ g}^{-1}$) [55,109,111–113]. Charge recombination results to poor formation of the radical species responsible for the redox reaction during photocatalysis. A large surface area presents numerous reactive sites and improve light-harvesting. Moreover, the diffusion pathway for the photogenerated electron/hole pairs is greatly reduced in high surface area materials, thereby increasing the reaction kinetics [87,101]. The band gap of 2.7 eV for $g\text{-C}_3\text{N}_4$ which corresponds to a threshold wavelength of about 450 nm, is still considerably large for efficient visible light harvesting and leaves the larger portion of the visible light spectrum unexploited [93].

2.1. Modification of $g\text{-C}_3\text{N}_4$ for improved photocatalytic activity

Tailoring $g\text{-C}_3\text{N}_4$ photocatalysts with improved optical properties, surface area, charge separation and photodegradation kinetics has been a subject of intense research in recent times. Various nanoarchitectures of $g\text{-C}_3\text{N}_4$ such as nanoparticles, nanosheets, nanorods, hollow vessels, nanoribbons, nanobelts, nanowires, *etc.* have been engineered and showed improvements in terms of their photocatalytic properties [91,111,114–122]. Another approach towards improving the activity of $g\text{-C}_3\text{N}_4$ entails the introduction of porosity in its structure via hard and soft-templating procedures which remarkably improve the surface area [123–130]. In a recent review, Yang et al. discussed some of the recent advancements towards hard and soft templating approaches for enhancing the photocatalytic activity of $g\text{-C}_3\text{N}_4$. [131]. Despite the success in terms of improving specific surface area observed from the materials of various architectures and the introduction of porosity, the higher recombination rate and low conductivity persist in pure $g\text{-C}_3\text{N}_4$ and lower the photocatalytic efficiency. Modification of $g\text{-C}_3\text{N}_4$ using dyes, polymers and surface complexes is another strategy that has been explored to improve visible light utilisation, charge separation and the overall photoactivity of $g\text{-C}_3\text{N}_4$ [112,132–138]. However, introducing heteroatoms (metal

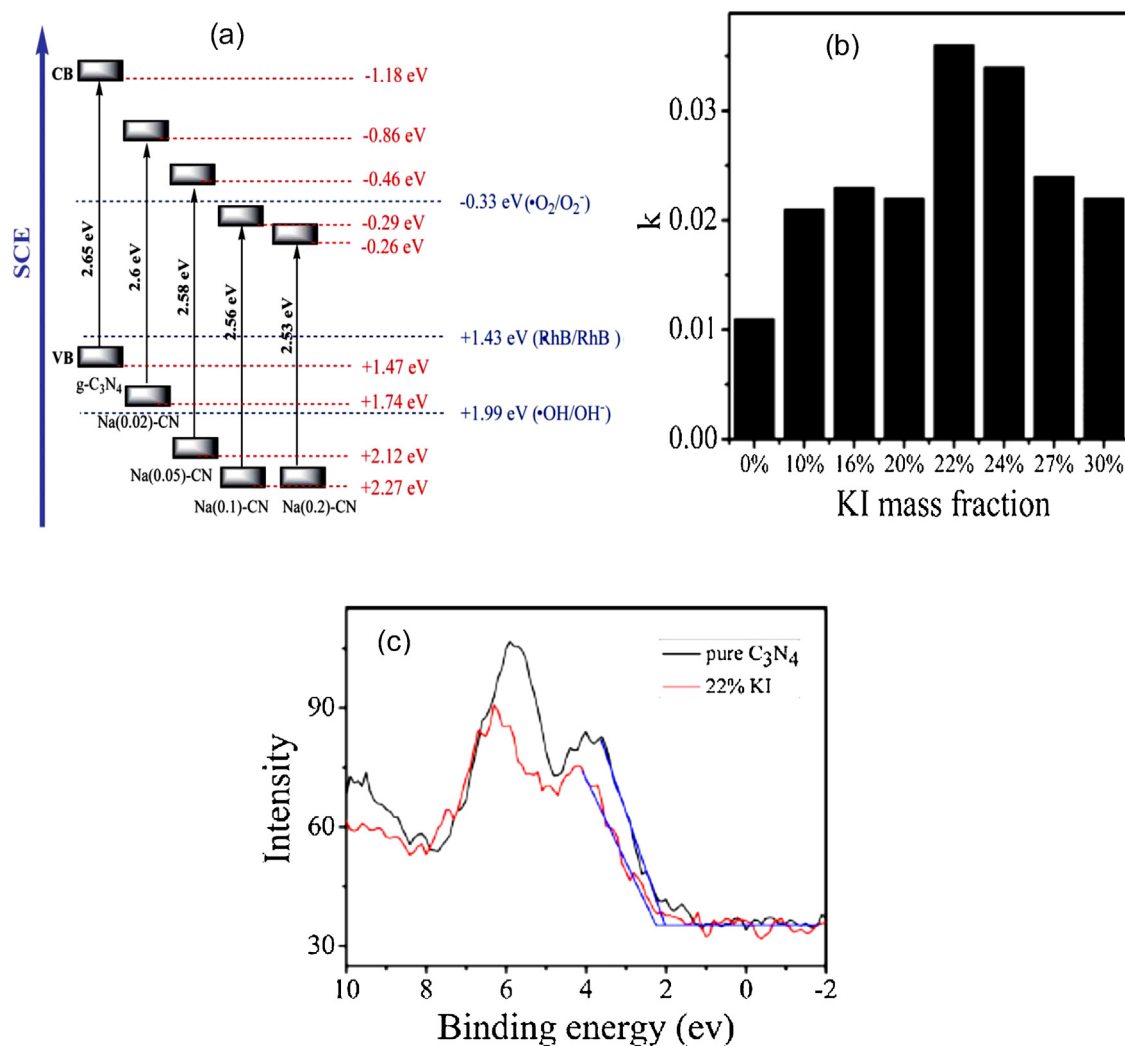


Fig. 5. (a) Band structures of pure and Na-g-C₃N₄ samples, (b) apparent rate constants for phenol degradation over pure and K-g-C₃N₄ samples with increasing KI loading and (c) valence band XPS spectra for pure and 22% K-g-C₃N₄.

(a) Reproduced with permission from Ref. [106], Copyright 2014, RSC. (b and c) Reproduced with permission from Ref. [144], Copyright 2015, Elsevier.

and non-metal doping) within the g-C₃N₄ framework, metal deposition, hybridising with carbon nanomaterials and coupling with other semiconductors have been the most attractive approaches towards fabricating heterostructures with improved photocatalytic activity [139–143].

In the preceding sections, we review the most recent advancements towards tailoring various g-C₃N₄ nanostructures for removal of a wide range of environmental pollutants. With the huge interest on g-C₃N₄ heterostructures in pollution control, it is necessary to put together a comprehensive review of the emerging materials in order to provide a perspective on the current status.

2.2. Metal decorated/doped g-C₃N₄ (g-C₃N₄-M) nanostructures

Doping of various metallic species such as the alkali metals, transition metals, rare earth metals and noble metals into g-C₃N₄ has been explored in an attempt to improve its photocatalytic efficiency towards removal of environmental pollutants. Sodium doped g-C₃N₄ (denoted as Na-CN) prepared by annealing of a mixture of sodium hydroxide and dicyandiamide as precursors, showed higher photocatalytic activity compared to pure g-C₃N₄ and a mixture of NaOH and g-C₃N₄ (NaOH/g-C₃N₄) towards decomposition of rhodamine B (RhB) under visible light illumination [106]. This was

credited to the inhibition of crystal growth by Na thereby improving the specific surface area, tunable valence and conduction band structure and efficient charge carrier separation. The sample prepared using 0.05 g NaOH designated as Na(0.05)-CN, showed the best performance among the Na doped samples and this can be explained in terms of the influence of the Na loading on the band structure of the doped samples (Fig. 5a). [106] Based on the calculated band potentials (Fig. 5a), Na(0.05)-CN has both the valence band (+2.12 eV) and conduction band (−0.46 eV) well positioned to hydroxide ions (OH•/OH[−] +1.99 eV) and adsorbed oxygen (O₂•[−]/O₂ −0.33 eV), respectively [106]. This results in efficient generation of both the hydroxyl and superoxide radicals which are responsible for the degradation of RhB. It was clear from this work that the Na loading play a crucial role in band gap narrowing, surface area improvement, charge separation and fine-tuning the band structure, which influence the photoactivity.

In a similar study, Zhang et al. observed higher photocatalytic activity towards phenol and methylene blue (MB) over potassium doped g-C₃N₄ (K-g-C₃N₄) compared to bulk g-C₃N₄ under visible light irradiation. Potassium iodide was used as a K source and at 22% KI loading (22%K-g-C₃N₄) the highest activity was observed and it was 3.3 and 5.8 times higher than that of bulk g-C₃N₄ for phenol and MB degradation, respectively (Fig. 5b) [144]. An increase in KI

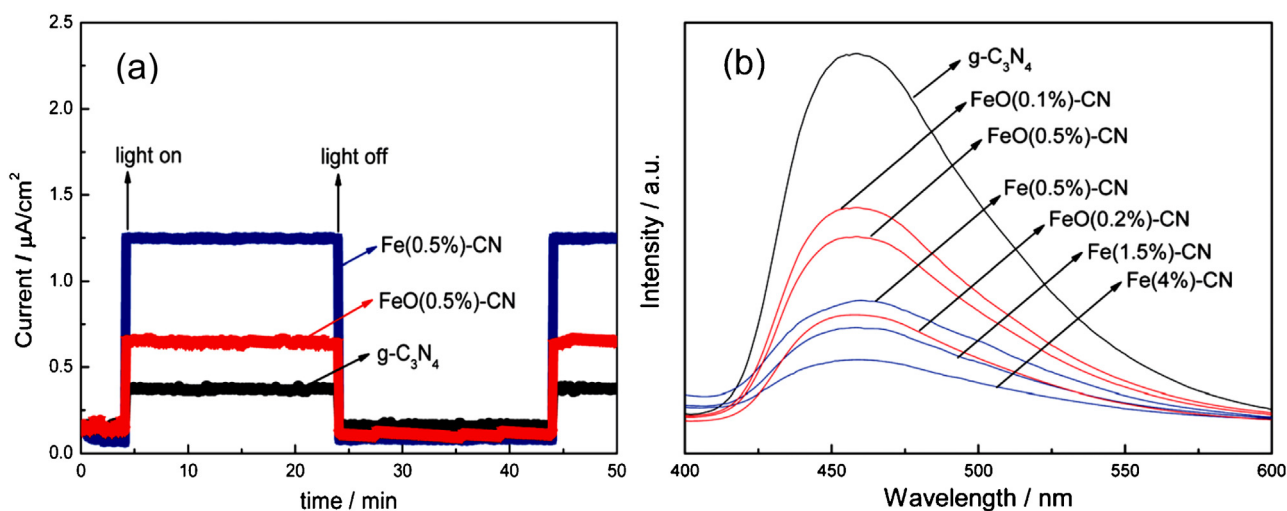


Fig. 6. (a) Photocurrent measurements and (b) PL spectra of $\text{g-C}_3\text{N}_4$, FeO-CN and Fe-CN samples.

Reproduced with permission from Ref. [145]. Copyright 2014, RSC.

loading beyond 22% was accompanied by a decrease in the photocatalytic activity and this could be attributed to the inhibition of polycondensation and increased defects in the $\text{g-C}_3\text{N}_4$ structure at higher KI levels. Interestingly, as observed in the case of Na doping, K doping also resulted in tuning of the band structure of $\text{g-C}_3\text{N}_4$ and valence band XPS revealed that K doping lowered the valence band position (Fig. 5c) [144].

Iron(III) doped $\text{g-C}_3\text{N}_4$ ($\text{Fe}^{3+}\text{-g-C}_3\text{N}_4$ denoted as Fe-CN) was prepared by annealing a mixture of melamine and $\text{Fe}(\text{NO}_3)_3 \cdot 9\text{H}_2\text{O}$ and its photocatalytic properties were investigated and compared to those of $\text{Fe}_2\text{O}_3/\text{g-C}_3\text{N}_4$ (denoted as FeO-CN) for the degradation of RhB under visible light irradiation. $\text{Fe}(0.5)\text{-CN}$ showed the highest activity which was 2.5 and 1.8 times that of pure $\text{g-C}_3\text{N}_4$ and $\text{Fe}_2\text{O}_3/\text{g-C}_3\text{N}_4$, respectively, indicating that 0.5% was the optimum $\text{Fe}(\text{III})$ loading [145]. The improved activity of the Fe-CN samples was ascribed to enhanced visible light absorption and efficient inhibition of the charge carrier recombination. Photocurrent measurements (Fig. 6a) revealed a higher response due to the $\text{Fe}(0.5)\text{-CN}$ compared to pure $\text{g-C}_3\text{N}_4$ and FeO-CN , indicating good separation of the electron/hole pairs. Similarly, photoluminescence measurements (Fig. 6b) confirmed good separation of the charge carriers in the $\text{Fe}(\text{III})$ doped samples [145]. However, at $\text{Fe}(\text{III})$ loadings above 0.5% there was a decline in the activity which could be linked to competition between electron trapping by Fe^{3+} and formation of the superoxide radicals which are the main oxidising species [145].

Similar results have been reported for zirconium doped $\text{g-C}_3\text{N}_4$ ($\text{Zr-g-C}_3\text{N}_4$) which displayed improved photocatalytic activity towards RhB with increasing Zr loading up to an optimum value of 0.5%. Beyond 0.5% Zr loading, the activity started decreasing which could be explained in terms of increased lattice defects, decreased crystallinity and the excess Zr acting as recombination centres [146]. Doping $\text{g-C}_3\text{N}_4$ with Zr induced a collaborative effect between improved visible light absorption due to band gap modification, enhanced charge separation, hierarchical mesoporous structure and large surface area which facilitate efficient mass transfer [146]. Wang et al. examined the photocatalytic reduction of CO_2 with H_2O over Mo-doped $\text{g-C}_3\text{N}_4$ nanostructures with varying Mo loadings, prepared using a simple pyrolysis route. The doped samples showed increasing surface areas and narrowing band gaps with increasing Mo content from 1 to 5% [147]. In terms of CO_2 reduction performance, the sample containing 4% Mo (Mo-CN-4) displayed the highest activity, reaching CO and CH_4 yields of 887

and $123 \mu\text{mol/g}$, respectively, after 8 h of UV exposure. Beyond 4% Mo loading, the activity of the catalyst decreased slightly which could be attributed to loss of crystallinity and increased defects which acted as recombination centres. The worm-like mesoporous architecture, large surface area, improved optical response and efficient charge separation, were cited as the core factors that contributed to the remarkable CO_2 reduction [147].

Dong et al. investigated the decomposition MB using europium doped $\text{g-C}_3\text{N}_4$ ($\text{Eu-g-C}_3\text{N}_4$) under visible light irradiation and the photocatalytic activity increased with increasing Eu^{3+} amounts up to 0.38% after which it declined. One possible explanation relates to the role of Eu^{3+} as an electron scavenger, minimising charge recombination [15]. However, when the concentration of Eu^{3+} exceeds the optimum level, the excess Eu^{3+} ions act as recombination centres. During electron trapping, Eu^{3+} is reduced to Eu^{2+} (Eq. (15)) which is oxidised back to +3 upon oxidation by oxygen which also result in the formation of the superoxide radical (Eq. (16)) responsible for dye decomposition. Besides the role as electron scavengers Eu^{3+} ions resulted in band gap modification and an increase in the specific surface area of the doped samples [15]. Both these factors contributed to the overall improved activity.



Doping cerium into $\text{g-C}_3\text{N}_4$ ($\text{Ce-g-C}_3\text{N}_4$ denoted as Ce-CN) showed a similar effect to Eu doping towards degradation of RhB under visible light illumination. High specific surface area, enhanced visible light absorption, band gap modification and efficient charge separation was observed upon Ce doping [148]. Valence band XPS and UV-vis well in confirming the modification of the band gap due to Ce^{3+} doping. Moreover, the Ce^{3+} ions were most likely occupying interstitial positions as opposed to substitutional positions in $\text{g-C}_3\text{N}_4$ due to the larger ionic radius of Ce^{3+} relative to carbon. At 0.5% Ce^{3+} levels, $\text{Ce}(0.5)\text{-CN}$ showed the highest activity, reaching 90% RhB degradation in 120 min of visible light exposure [148].

Noble metal deposition is another attractive approach towards improving the photocatalytic efficiency of $\text{g-C}_3\text{N}_4$. Li et al. used photodeposition to load Ag nanoparticles (5–20 nm in diameter, Fig. 7a) on $\text{g-C}_3\text{N}_4$ nanosheets and studied the photocatalytic properties of the doped samples (denoted as AGCNs) towards decomposition of RhB under visible light illumination. The photocatalytic activity increased with increasing Ag concentration with an optimum at 8%

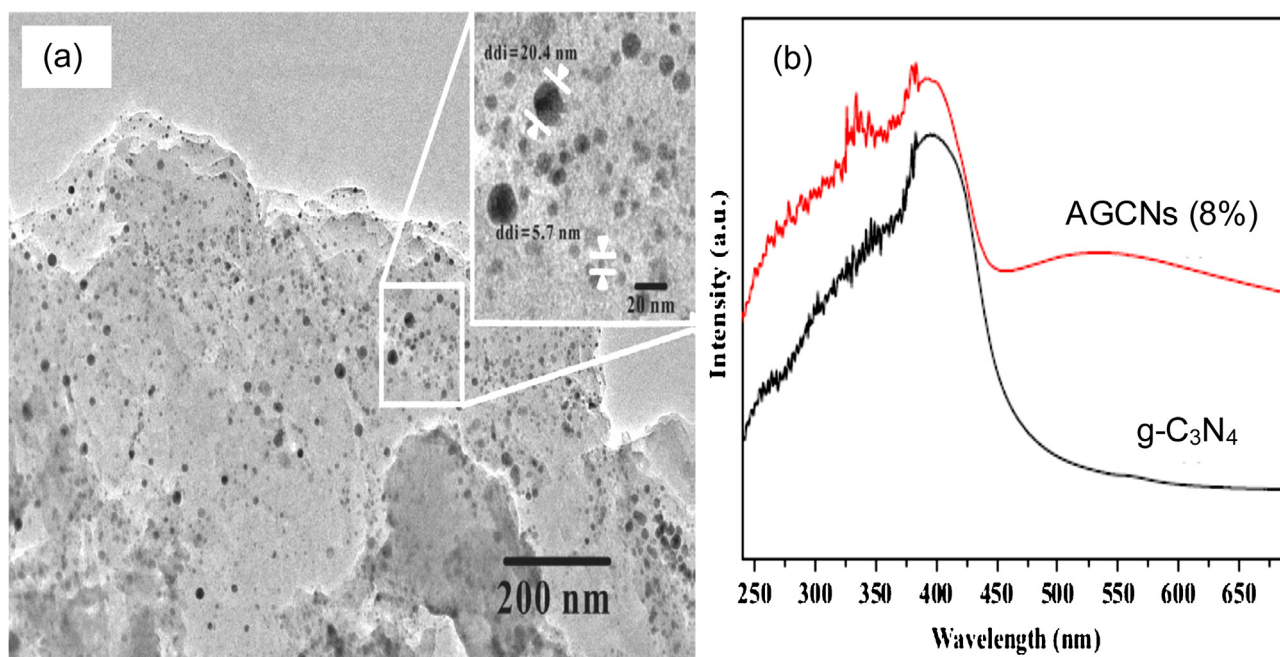


Fig. 7. (a) TEM image of AGCNs (8%) and (b) UV–vis diffuse reflectance spectra of pure and Ag loaded g-C₃N₄. Reproduced with permission from Ref. [149]. Copyright 2015, Elsevier.

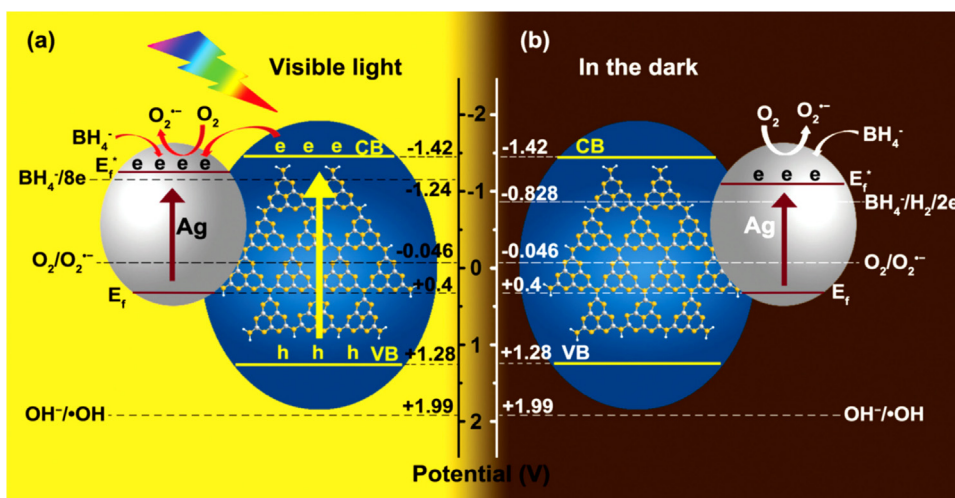


Fig. 8. Photocatalytic degradation mechanism over Ag/g-C₃N₄-4 in the presence of BH₄[−] ions (a) under visible light illumination and (b) in the dark. Reproduced with permission from Ref. [150]. Copyright 2015, RSC.

and a further increase resulted in a decrease in the activity due to electron/hole recombination occurring over the excess Ag [149]. At the optimum Ag concentration, the activity of AGCNs (8%) was 7 times that of pure g-C₃N₄ and this was due to a combined contribution of efficient utilisation of visible light (Fig. 7b) and improved charge separation efficiency. Fu et al. investigated the visible light photocatalytic degradation of methyl orange (MO), MB and neutral dark yellow GL (NDY-GL) over Ag/g-C₃N₄ fabricated through the reduction of AgNO₃ by sodium borohydride. The catalyst with the optimum Ag loading (4%) denoted as Ag-g-C₃N₄-4 showed the highest activity for all three dyes both in the presence of borohydride ions (BH₄[−]) as additives and in their absence. Interestingly, addition of BH₄[−] ions improved the photoactivity remarkably, and even enabled degradation in the dark [150]. In the presence of the BH₄[−] ions but in the dark, degradation efficiencies of 95.5% after 20 min, 96.0% after 120 min and 93.8% after 28 min of contact, were attained over Ag/g-C₃N₄-4 for MO, MB and NDY-GL, respectively.

Notably, these values were significantly higher than the values for degradation of the dyes under visible light irradiation but in the absence of BH₄[−] ions [150]. However, in the presence of BH₄[−] and visible light, the activity increased considerably, reaching 98.2% in 8 min, 99.3% in 45 min and 99.6% in 16 min of illumination, for MO, MB and NDY-GL, respectively. This observation demonstrates the synergy between the BH₄[−] ions, visible light and Ag-g-C₃N₄-4 towards the overall photocatalytic activity.

Fig. 8 shows the proposed mechanism for the degradation of the dyes in the presence of BH₄[−] ions. The superoxide radical was identified as the predominant oxidising species responsible for dye degradation. Under visible light irradiation (Fig. 8a), g-C₃N₄ is excited and electrons are pushed to the conduction band leaving holes in the valence band. Subsequently, the conduction band electrons of g-C₃N₄ are transferred to Ag where they are trapped by oxygen to form the superoxide radicals. Furthermore, BH₄[−] ions are oxidised on the surface of the catalyst, releasing electrons which are

trapped by oxygen to form additional radicals thereby speeding up the degradation kinetics [150]. In the dark (Fig. 8b), the observed degradation could be due to the hydrolysis of BH_4^- ions releasing H_2 which is then oxidised by hydroxide ions releasing two electrons. These electrons are trapped by oxygen to form the superoxide radicals [150].

Munoz-Batista et al. investigated the biocidal effect of Ag/g- C_3N_4 hybrid photocatalysts with varying Ag contents towards *Escherichia coli*, under UV and visible light illumination. It was observed that the photocatalytic activity increased with increasing Ag loading and the highest performance was recorded at 10% Ag loading [151]. Furthermore, the Ag/g- C_3N_4 nanostructures showed higher activity under UV exposure compared to visible light and the biocidal effect was as a result of the attack of the bacterial cell wall by the holes and superoxide radicals generated upon excitation of the photocatalyst [151]. Similarly, Ma et al. evaluated the photocatalytic inactivation of *E. coli* over Ag/g- C_3N_4 nanocomposites under visible light irradiation and at 3% Ag loading, the photocatalyst displayed the highest activity. The enhanced activity of the nanocomposite photocatalyst compared to Ag nanoparticles and g- C_3N_4 was ascribed to the combined contribution of the two components which resulted in rapid and efficient charge separation and transportation, and improved visible light utilisation [152]. Investigation of the effect of pH and humic acid revealed that there was not significant change in the activity of the photocatalyst within the studied pH range (6.2–8.2) and in the presence of humic acid at concentrations less than 2 ppm. However, at humic acid concentrations of 2 ppm and above, the activity towards *E. coli* decreased considerably, and this could be attributed to the humic acid acting as a protective shield to the bacteria by binding to the bacterial cell wall thereby protecting them from oxidation by the holes and superoxide radicals [152].

Liu et al. employed a green synthesis route to deposit Ag nanoparticles on g- C_3N_4 nanosheets using grape seed extract as reducing and stabilising agent [153]. As controls, the grape seed extract and pure g- C_3N_4 nanosheets did not show any significant inhibition zone towards *E. coli*, *Pseudomonas aeruginosa*, *Staphylococcus aureus* and *Bacillus subtilis*. Contrary, the Ag nanoparticles and Ag/g- C_3N_4 nanocomposite showed significant inhibition zone for all four pathogens with the nanocomposite showing the highest activity owing to the synergy between Ag and g- C_3N_4 [153]. It is generally accepted that in the Ag/g- C_3N_4 nanocomposites, the photogenerated holes and the superoxide radicals are the active species responsible for the photocatalytic inactivation of the microbial pollutants. Moreover, the mechanism of attack of the pathogens entails the oxidation of the bacterial cell wall and membrane by the holes and superoxide radicals resulting in porous cells, leakage of important cellular contents and eventual cell death [151–153].

Other reports are available on the synthesis and application of Ag/g- C_3N_4 in the removal a wide range of environmental pollutants such as toluene [154], MO and H_2 evolution [155], MO and para-nitrophenol (PNP) [156], *E. coli* and *S. aureus* biofilms [157] and MB and H_2 evolution [158]. These studies emphasise on the versatility of the material which is a desirable property in practical environmental applications. Although all the materials are Ag-g- C_3N_4 , they have been prepared under different experimental conditions and from different precursors, yielding materials with different morphologies and band structures which ultimately translates to differences in photocatalytic activity. In a recent study, Tian et al. demonstrated that the method of preparation/loading of the Ag nanoparticles on g- C_3N_4 had a bearing on the photocatalytic activity [159]. For example, Ag/g- C_3N_4 prepared using watermelon extract showed higher activity compared to Ag/g- C_3N_4 prepared using sodium hydride. This was ascribed to smaller Ag nanoparticle sizes and good dispersion on g- C_3N_4 due to the soluble enzymes, organic acids, vitamins and polysaccharides which as both reduc-

ing and capping agents [159]. Aggregation and larger particle sizes of the Ag nanoparticles was cited as the possible root cause of the lower photocatalytic activity observed for Ag/g- C_3N_4 prepared using sodium hydride [159].

Deposition of other noble metal nanoparticles such as Cu [160], Pt [161,162], Au [161,163–165] and Pd [166,167] on g- C_3N_4 yielded hybrid nanostructures with significantly superior photocatalytic activity compared to pure g- C_3N_4 under visible light illumination. For example, Bai et al. employed a solution phase route to grow single-faceted Pd nanocrystals on g- C_3N_4 nanosheets in an *in situ* process. Br^- and I^- ions were used to stabilise Pd(100) facets while HCHO and $\text{Na}_2\text{C}_2\text{O}_4$ were used in the formation of Pd(111) facets. The hybrid materials were examined for the photocatalytic reduction of CO_2 in the presence of water vapour to form various products such as CO, CH_4 and $\text{C}_2\text{H}_5\text{OH}$ [168]. Coupling g- C_3N_4 with Pd accelerated the formation of the CO_2 reduction products compared to pure g- C_3N_4 . Moreover, it was observed that the Pd facets endowed the hybrid nanostructures with remarkable selectivity, with CO_2 reduction favoured in the Pd(111) facets while the Pd(100) facets preferentially generated H_2 from oxidation of water. The selectivity of the Pd facets could be explained from theoretical calculations of the adsorption and activation energies [168]. Similarly, Pt decorated g- C_3N_4 showed elevated photocatalytic performance and selectivity towards CO_2 reduction to CH_4 , CH_3OH and HCHO, under simulated solar light [169]. CO_2 reduction efficiency was found to increase with increasing Pt loading up to an optimum level, beyond which no further enhancement could be observed. The Pt nanoparticles were responsible for trapping, transfer and accumulation of electrons from g- C_3N_4 to its surface where CO_2 reduction occurred. In addition, the Pt nanoparticles functioned as co-catalyst to facilitate the oxidation of the CO_2 reduction products [169].

In all the studies on metal decorated g- C_3N_4 , special emphasis has been on the metal concentration because the metal content positively influence the photocatalytic activity until the optimum loading is reached. Beyond the optimum metal loading, the excess metal ions act as recombination centres for the electron/hole pairs resulting to a decline in the degradation efficiency. Another setback of metal decoration relates to leaching of the metal nanoparticles into the water causing secondary pollution and unfortunately studies on the leaching of the metal ions are seldom conducted. In most cases stability of the whole catalyst is studied by recycling the material for a couple of times (usually 5 times) and different materials exhibit different stabilities but generally the activity does decline over time and leaching of the metallic species is rarely cited as a possible cause for the decline.

2.3. Non-metal doped g- C_3N_4 (g- C_3N_4 -X) nanostructures

Doping g- C_3N_4 with non-metals is another approach to improve its visible light utilisation and overall photocatalytic activity. Unlike metal doped g- C_3N_4 which can often cause secondary pollution due to leaching of the metal ions, non-metal doped g- C_3N_4 is a metal-free photocatalyst and the fact that the non-metal species does not take part in charge transportation, it does not form recombination centres. Man et al. theoretically studied the effect of P and S doping g- C_3N_4 using density functional theory (DFT) based calculations. Both interstitial and substitutional dopant models in order to determine the most energetically feasible form and the overall effect of non-metal doping on the visible light activity of g- C_3N_4 [170]. It was realised that the S atom most likely substituted the N atom at the edge of g- C_3N_4 while the P atom favoured interstitial positions in the in-planar of g- C_3N_4 . Moreover, the theoretical studies showed that the doping of g- C_3N_4 with S and P improved visible light absorption by altering the band gap, enhanced charge carrier separation and transfer [170]. Experimental results confirmed that P doping does improve visible light absorption as observed

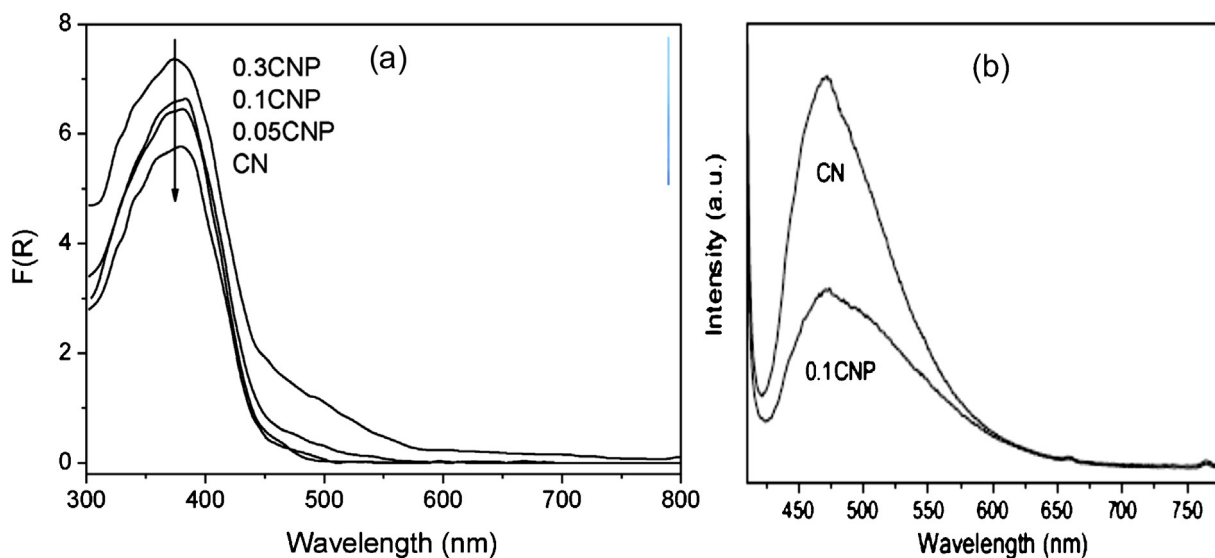


Fig. 9. (a) UV-vis absorption spectra and (b) PL spectra of pure and P doped g-C₃N₄.

Reproduced with permission from Ref. [171]. Copyright 2013, Elsevier.

from the UV-vis diffuse reflectance spectra (Fig. 9a) and charge separation which was confirmed by the low PL signal (Fig. 9b). The overall result was improved visible light photocatalytic degradation of MB and MO over the P doped g-C₃N₄ samples (denoted CNP) compared to pure g-C₃N₄ (denoted CN) [171]. The highest activity was observed from 0.1CNP which was prepared by adding 0.1 g (25 wt%) of the P precursor which shows that the optimum P level can be obtained using small amounts.

Similar results have been reported for the degradation of RhB over P/g-C₃N₄ prepared from two different P sources. Interestingly, when (NH₄)₂HPO₄ was used, P was interstitially doped but when the ionic liquid [Bmim]PF₆ was used, substitutionally doped P was obtained. Additionally, higher photocatalytic activity was recorded for interstitial doped P/g-C₃N₄ compared to its substitutional counterpart [172]. P doping inhibited g-C₃N₄ crystal growth, lead to band gap narrowing and improved separation of the photogenerated charge carriers [172]. In a recent study, Zhou et al. P/g-C₃N₄ could be used for both organic pollutants degradation and hydrogen evolution under visible irradiation. Improved surface chemistry, efficient visible light harvesting and charge separation were cited as the possible reasons behind the higher activity of P/g-C₃N₄ compared to pure g-C₃N₄ [173].

Calcining thiourea at 520 °C yielded sulphur doped g-C₃N₄ (S-g-C₃N₄) with a narrower band gap (2.63 eV) than melamine derived g-C₃N₄ (2.7 eV). The two samples were evaluated for the reduction of CO₂ to methanol under visible light irradiation. S-g-C₃N₄ displayed superior photocatalytic activity over g-C₃N₄ owing to S-doping which enhanced visible light response and introduced defects which aid in the separation of the charge carriers [174]. Despite theoretical calculations predicting equal band gaps for S-doped and pure g-C₃N₄, S-g-C₃N₄ had an impurity level within the g-C₃N₄ band gap (Fig. 10b) which allowed easy excitation of electrons from the valence band to the impurity level. Alternatively, electrons could be excited from the impurity level into the conduction band of g-C₃N₄, where they are captured by CO₂ and facilitate its reduction to form methanol as summarised in Eq. (17)–(20). The holes remained in the valence band and could facilitate oxidation of water to form oxygen and protons [174]. The absence of the impurity state in pure g-C₃N₄ (Fig. 10a) result to lower visible light utilisation and higher rate of recombination of the charge carriers.

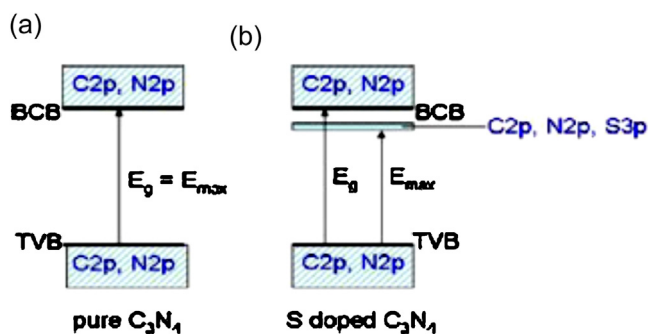
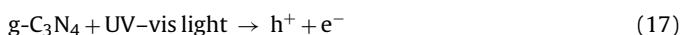
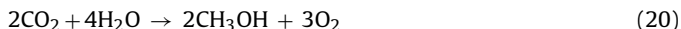
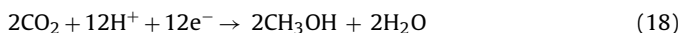


Fig. 10. Band structure of (a) pure g-C₃N₄ and (b) S-g-C₃N₄.

Reproduced with permission from Ref. [174]. Copyright 2015, Elsevier.



Li et al. fabricated carbon doped g-C₃N₄ (C/g-C₃N₄) with varying C loadings using a hydrothermal approach and glucose (0–0.3 g) as a carbon source. At the optimum glucose concentration (0.005 g), the C-doped sample showed the highest photocatalytic performance towards MB owing to good visible light absorption, efficient adsorption of MB and improved charge separation [175]. It has been predicted from theoretical calculations that C-doping induced band gap narrowing and improved visible light response in C/g-C₃N₄. The band gap narrowed with increasing C loading until it almost closed at a C loadings of 2.609% thereby inducing transition from semiconductor to metal phase [176]. Degradation of RhB and MO over boron-doped g-C₃N₄ (B-g-C₃N₄) was investigated under visible light illumination and B-doping resulted in improved activity. MO degradation proceeded mainly via photoreduction by the superoxide radicals while RhB degradation was mainly due to photooxidation by the valence band holes [177]. Oxygen-doped g-C₃N₄ (O/g-C₃N₄) showed remarkable visible light photocatalytic degradation of RhB, MO and pentachlorophenol (PCP) under anoxic conditions [178]. Improved pollutant adsorption properties, hydrophilicity, enhanced optical response in the visible range and charge separation efficiency collectively contributed to the higher activity of O/g-C₃N₄ compared to pure g-C₃N₄.

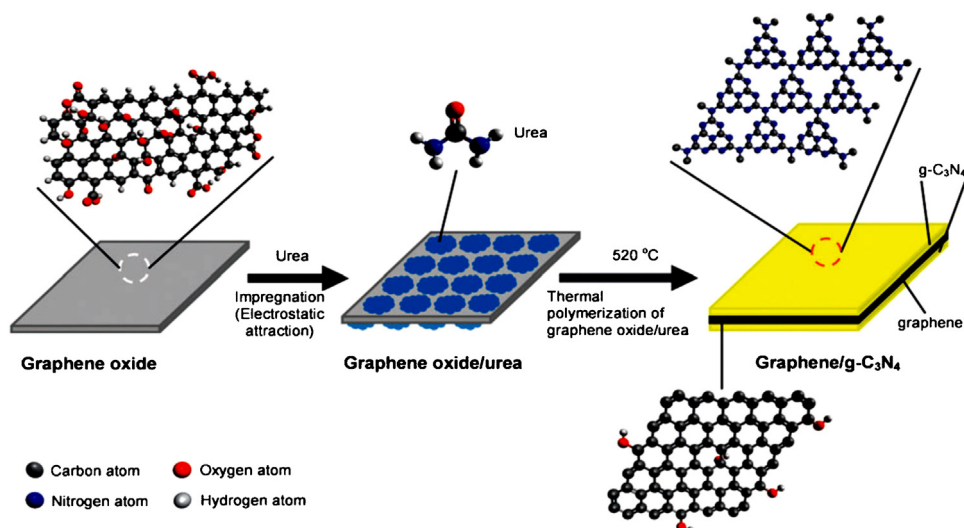


Fig. 11. Schematic showing the one-pot synthesis of GCN via impregnation-reduction route.

Reproduced with permission from Ref. [186]. Copyright 2014, RSC.

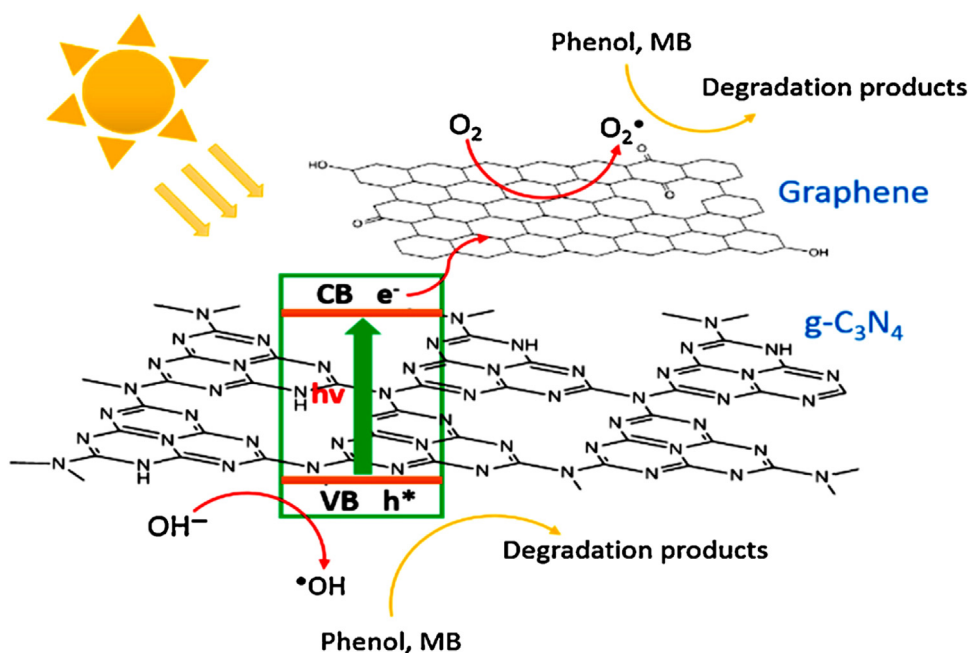


Fig. 12. Charge transfer mechanism in RGO/g-C₃N₄ for the photocatalytic degradation of MB and phenol.

Reproduced with permission from Ref. [185]. Copyright 2015, Elsevier.

[178]. Likewise, codoping g-C₃N₄ with P and O (P-O-g-C₃N₄) significantly enhanced the photocatalytic properties towards RhB compared to pure g-C₃N₄ and O-g-C₃N₄. This was credited to synergy between P and O codoping resulting to a large specific surface area, improved optical properties and efficient charge separation [179].

2.4. Coupling g-C₃N₄ with carbon nanomaterials (g-C₃N₄/CNM heterojunctions)

Carbon nanomaterials such as carbon nanotubes (CNTs), carbon nanospheres (CNS), graphene oxide (GO) and reduced graphene oxide (RGO) have received considerable interest in various scientific fields due to their intrinsic properties. Such properties include high thermal and electronic conductivity, chemical and

thermal stability, excellent mechanical properties, high specific surface area and remarkable adsorption properties for both organic and inorganic compounds [180–182]. Graphene is one of the most popular CNMs in tailoring semiconductor-CNMs hybrids owing to its ballistic electronic transport and ultrahigh electron mobility ($200000\text{ cm}^2\text{ V}^{-1}\text{ s}^{-1}$), high transparency (97% optical transmittance), high thermal conductivity ($\sim 5000\text{ W m}^{-1}\text{ K}^{-1}$), massless fermions, flexible structure and large specific surface area ($\sim 2600\text{ m}^2/\text{g}$) [182,183].

G-C₃N₄ hybridised with GO (g-C₃N₄/GO) via a sonochemical route showed improved photocatalytic properties towards RhB and 2,4-dichlorophenol (2,4-DCP) degradation under visible light exposure [184]. For RhB degradation, the activity of the hybrid material was 3.80 times that of g-C₃N₄, reaching 94.4% RhB removal in 150 min while for 2,4-DCP the activity was 2.08 times that of g-

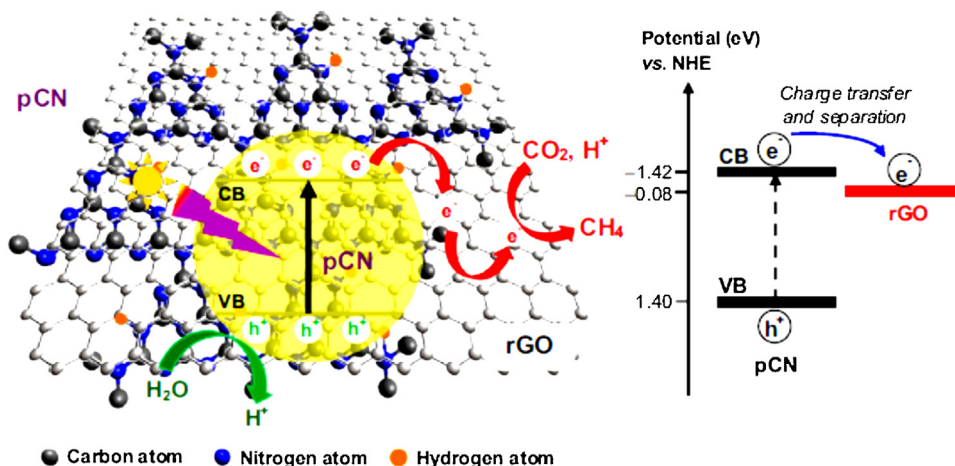


Fig. 13. Schematic for the charge transfer and separation mechanism in RGO/pCN during CO₂ reduction.

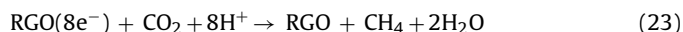
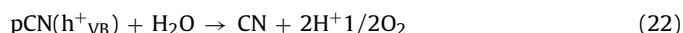
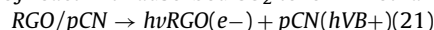
Reproduced with permission from Ref. [187]. Copyright 2015, Elsevier.

C₃N₄, reaching 87.1% removal in 240 min of irradiation [184]. Ai et al. prepared RGO-g-C₃N₄ hybrids (denoted as G-CN) with varying RGO loadings using a one-pot thermal condensation of melamine and RGO and studied its visible light photocatalytic degradation of MB and phenol. Under optimised conditions, the sample containing 0.4 g RGO (G-CN-0.4) showed the highest activity, reaching 100% MB degradation in 180 min and 87% phenol removal in 210 min [185]. Ong et al. used GO as structure directing agent for tailoring sandwich-like GO-g-C₃N₄ heterostructures (denoted as GCN) with varying GO loadings as shown in Fig. 11. The prepared materials were evaluated for the reduction of CO₂ to methane under visible light irradiation and the activity increased with increasing GO concentration up to an optimum GO concentration of 15 wt%, reaching 5.87 μmol g⁻¹ which was 2.3 times higher than that of pure g-C₃N₄ [186]. Additionally, all the GCN samples maintained a reactivity of 90% after 10 h of irradiation which showed good stability of the photocatalysts [186]. Similarly, protonation of g-C₃N₄ prior to electrostatic self-assembly of 2D/2D RGO/g-C₃N₄ yielded nanostructures (denoted RGO/pCN) with remarkable photoactivity towards reduction of CO₂ to methane under visible light illumination [187].

Coupling g-C₃N₄ with GO/RGO resulted to improved photoreponse in the visible region, prolonged life of the photogenerated charge carriers, enhanced adsorption properties and increased specific surface area [184–187]. Theoretical calculations based on DFT have predicted the positive contribution of GO/RGO towards tuning the optical properties and charge separation and transportation in GO/RGO/g-C₃N₄ hybrid photocatalysts [188]. Strong and intimate RGO/g-C₃N₄ interface is a prerequisite in order to exploit the synergistic effect of both materials [186,187]. In a typical visible light driven photocatalytic degradation mechanism (Fig. 12), electrons are excited from the valence band of g-C₃N₄ to its conduction band upon visible light absorption. Subsequently, the conduction band electron are transferred to RGO/GO where they are captured by adsorbed oxygen to form the superoxide radicals responsible for pollutant decomposition [184,185]. This leaves abundant positive holes in the valence band of g-C₃N₄ which can abstract an electron from the dye molecule forming an unstable organic radical which undergoes a series of oxidative reduction reactions to form the degradation products such as CO₂, H₂O, inorganic ions and other smaller organic intermediates [184,185]. Notably, the valence band hole is less positive (+1.57 eV vs NHE) compared to the redox potential for oxidation of hydroxide ions to form the hydroxyl radical (OH⁻/OH• +1.99 eV vs NHE) making it extremely difficult to form the hydroxyl radicals [189]. Therefore, the formation of the

hydroxyl radicals depicted in Fig. 12 is insignificant and could not easily be accomplished. Instead, the holes are directly involved in the degradation of the pollutants.

The photocatalytic reduction of CO₂ to methane over g-C₃N₄/RGO proceeded in a similar mechanism to organic pollutants degradation. Ong et al. proposed a mechanism for the charge transfer and separation in RGO/pCN and GCN nanocomposites for CO₂ reduction with water under visible light irradiation (Fig. 13) [186,187]. Upon visible light absorption, electrons are excited from the valence band to the conduction band of g-C₃N₄ (Eq. (21)). Subsequently, the conduction band electrons are transferred to RGO due to its lower Fermi level (−0.08 eV vs NHE) compared to the conduction band of g-C₃N₄ (−1.42 eV vs NHE) [187]. Meanwhile, the valence band holes oxidise water to form oxygen and protons. (Eq. (22)). Both the protons and electrons accumulate on RGO where they react with adsorbed CO₂ to form methane (Eq. (23)) [186,187].



Although the incorporation of RGO/GO into g-C₃N₄ enhanced the activity, this holds true until an optimum GO/RGO loading is reached. An increase in the carbon nanomaterial content beyond the optimum concentration results to a decrease in the photocatalytic activity due to insufficient light reaching g-C₃N₄ since some of the light is absorbed by the excess carbon nanomaterials. Moreover, in the case of organic dyes, the excess GO/RGO facilitate adsorption of large amounts of the dye molecules onto the catalyst surface thereby reducing light penetration to the photocatalyst. Therefore it is necessary to carefully control the GO/RGO contents in order to strike a balance between good dye adsorption, visible light absorption by the photocatalyst and charge separation and transportation efficiency.

CNTs are other attractive carbon nanomaterials for tailoring hybrid nanostructures with g-C₃N₄ for photocatalytic applications such as water splitting, environmental decontamination, oxygen reduction reactions, etc. [190–193]. A composite photocatalyst of white g-C₃N₄ and multiwalled carbon nanotubes (MWCNTs) (denoted as CNT/white C₃N₄) was obtained via electrostatic driven self-assembly of the protonated white C₃N₄ in a hydrothermal reaction. CNT/white C₃N₄ showed remarkable visible light photocatalytic activity towards MB degradation and its activity was almost 8 times that of pure white C₃N₄ [192]. Incorporation of the CNTs was credited with the improved visible light response, effi-

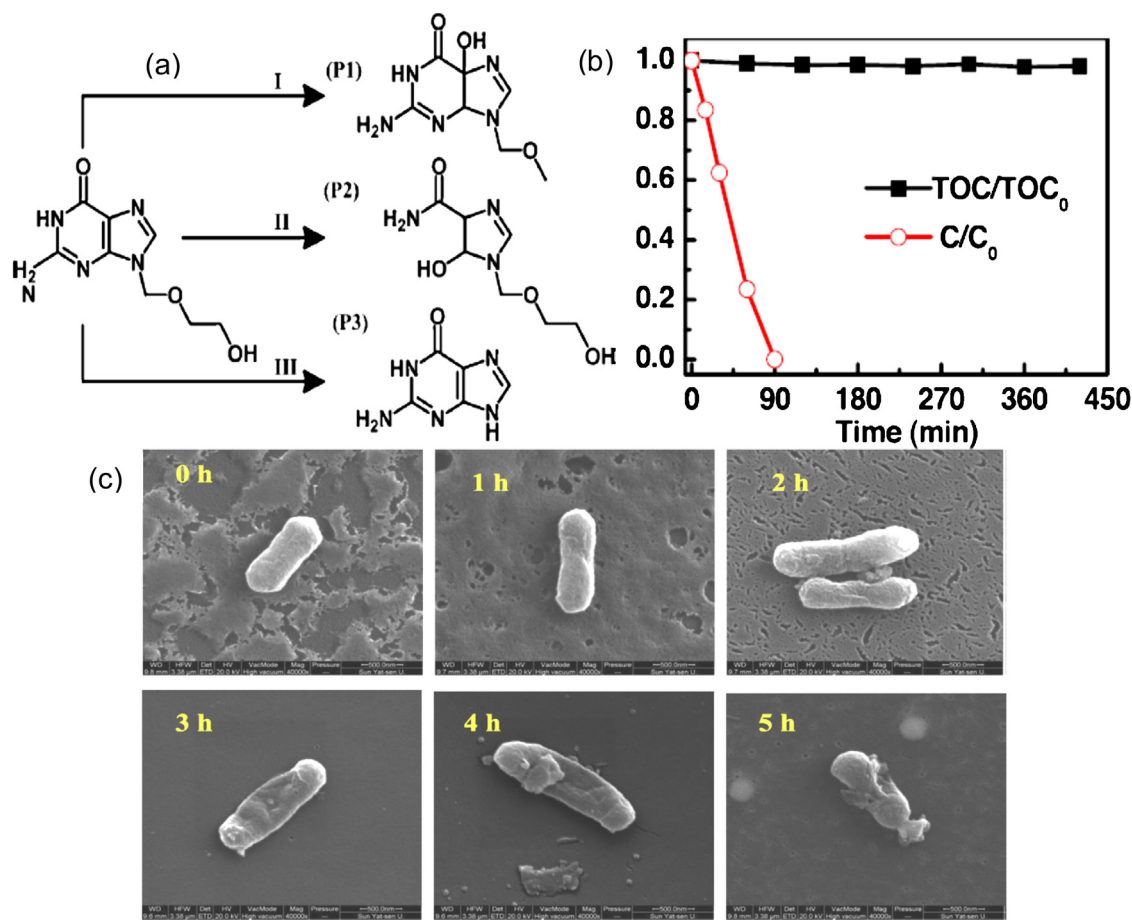
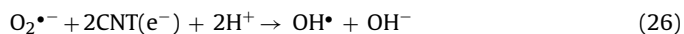
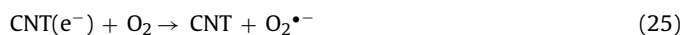
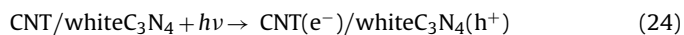


Fig. 14. (a) Acyclovir degradation products, (b) TOC removal during acyclovir degradation and (c) SEM images of *E. coli* K12 after being treated using g-C₃N₄/TiO₂ for different durations.

(a and b) Reproduced with permission from Ref. [204], Copyright 2016, Elsevier. (c) Reproduced with permission from Ref. [67], Copyright 2015, Elsevier.

cient charge carrier separation and transfer and the concentration of MB molecules onto the photocatalyst surface [192].

According to the proposed photocatalytic degradation mechanism by CNT/white C₃N₄, the electrons and holes occupy the conduction band and valence band, respectively, upon excitation by visible light. The electrons transfer to CNT via the CNT/white C₃N₄ interface while the holes remain in the valence band of white C₃N₄ (Eq. (24)) [192]. On the CNT skeleton, the electrons are trapped by adsorbed molecular oxygen to form the superoxide radicals which are responsible for dye degradation (Eq. (25)). Alternatively, the superoxide radicals may further react with protons and electrons to form the hydroxyl radicals which are stronger oxidising agents (Eq. (26)). the valence band holes can directly oxidise dye molecules via hydrogen abstraction leading to their degradation to form smaller degradation intermediates, CO₂, H₂O and inorganic ions [192].



Other carbon nanomaterial/g-C₃N₄ heterostructures such as sulphur doped g-C₃N₄/sulphur, selenium codoped graphene (CNS/S-Se-Gr)[194], carbon quantum dots (CQDs)/g-C₃N₄ [195,196], carbon nanospheres/g-C₃N₄ (CN-CS)[197], fullerene/g-C₃N₄ (C₆₀/C₃N₄)[198,199], biochar/g-C₃N₄ (BC-C₃N₄)[200], nanodiamond/g-C₃N₄ (ND/CN_x)[201] and GO/porous g-C₃N₄ [202] have been fabricated and showed improved photocatalytic activity towards various organic pollutants under visible light irradiation.

The CNM/g-C₃N₄ hybrid photocatalyst are attractive materials due to their metal-free nature. However, with the fate of some of these CNMs in the environment not fully understood, the risk of secondary pollution is still a challenge. Therefore is necessary to monitor the leaching of these materials in order to establish how much is lost/released during the degradation process.

2.5. Coupling g-C₃N₄ with other semiconductors

Coupling two or more semiconductors to form a semiconductor/semiconductor heterojunctions is one of the most promising strategies towards tailoring more efficient photocatalysts. This enhancement in photocatalytic properties emanates from the synergy between the two semiconductors resulting to improved stability, visible light utilisation, charge separation and transfer and more efficient formation of the oxidising species.

2.5.1. Binary nanocomposites (g-C₃N₄/MO heterojunctions)

Titania is one of the popular choices to couple with g-C₃N₄ due to its well-known photocatalytic properties. TiO₂ nanoparticles (5.5 nm in diameter) were anchored g-C₃N₄ nanosheets using a facile and environmentally friendly biomimetic synthesis strategy. The obtained composite photocatalyst (g-C₃N₄/TiO₂) exhibited improved photoactivity towards RhB degradation compared to g-C₃N₄, TiO₂ and their mixture [203]. At a g-C₃N₄ loading of 25.9%, the composite photocatalyst showed the highest activity, reaching 100% RhB degradation in 50 min of simulated solar light irradiation [203]. Li et al. evaluated the visible photocatalytic degradation of

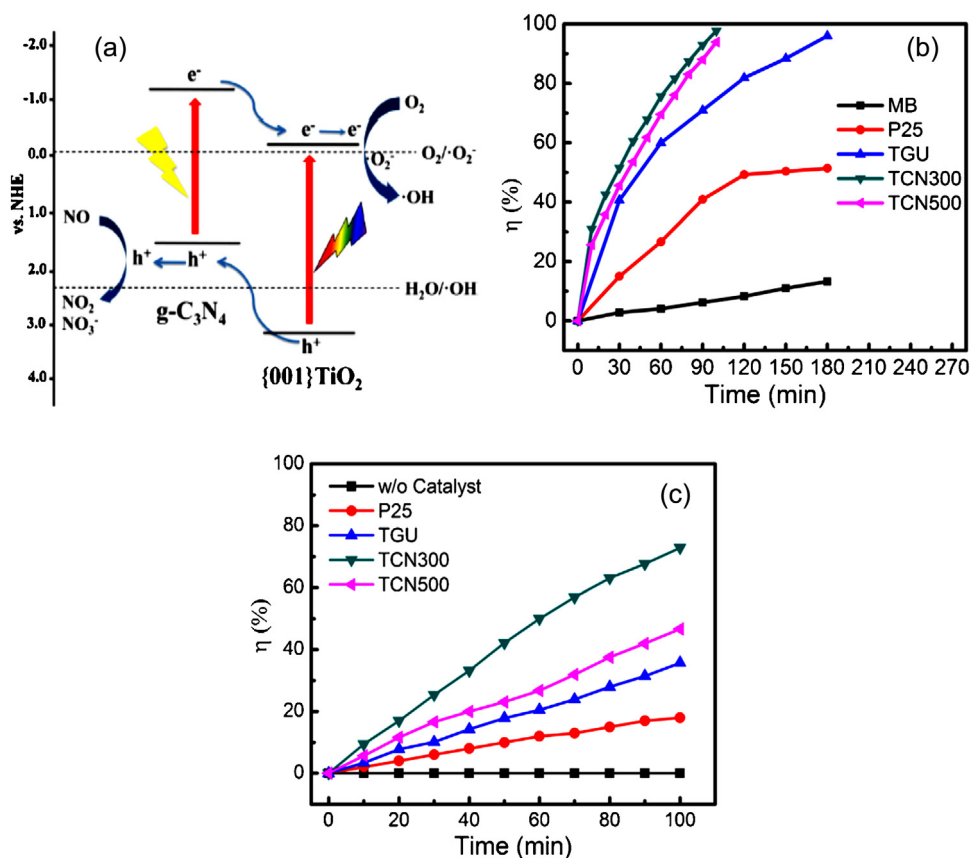


Fig. 15. (a) Charge transfer mechanism in g-C₃N₄/TiO₂ during NO oxidation, (b) degradation of MB and (c) Cr(VI) reduction. (a) Reproduced with permission from Ref. [207], Copyright 2016, Elsevier. (b) Reproduced with permission from Ref. [210], Copyright 2013, Elsevier.

environmental pharmaceutical, acyclovir which is an antiviral drug, over hydrothermally prepared g-C₃N₄/TiO₂. Despite the nanocomposite photocatalyst being able to completely decompose acyclovir in 90 min, three persistent degradation products were formed (Fig. 14a) [204]. These degradation products showed remarkable stability towards photocatalytic degradation (Fig. 14b) and this could be attributed to the low oxidation potential of the holes and superoxide radicals which were the main oxidising species. It was further predicted that one of the persistent intermediates (P3, guanidine, Fig. 14a) was more toxic than acyclovir [204].

Huang et al. demonstrated that g-C₃N₄ hybridised with hollow titania nanobox (g-C₃N₄/TiO₂-HNB) via TiO₂ (101) facets is more photocatalytic active compared to g-C₃N₄ contacted to TiO₂ via (001) facets, towards degradation of Brilliant Red X 3B (BRX3B) under UV light irradiation [205]. The (101) contact favoured efficient removal of electrons from the conduction band of TiO₂, thereby improving charge separation [205]. Efficient bacterial inactivation was reported under visible light using g-C₃N₄/TiO₂ obtained by a hydrothermal-calcination route [67]. Irreparable bacterial cell damage (Fig. 14c) was observed upon exposure of bacterial cultures to g-C₃N₄/TiO₂ under visible light irradiation for 3 h. This could lead to acute loss of the important intracellular components, resulting to bacterial death [67]. In another work, g-C₃N₄/TiO₂ obtained through annealing a mixture of melamine and P25 was investigated for photocatalytic oxidation of NO to NO₃⁻ both under visible and UV light illumination [206]. The sample containing 15% g-C₃N₄ denoted as M400, showed the highest activity reaching 27% compared to P25 (7%) and pure g-C₃N₄ (17%) [206]. Song et al. employed a simple solvent-free *in situ* route to prepared g-C₃N₄/TiO₂ composite photocatalysts with varying g-C₃N₄ loadings and evaluated their photocatalytic properties towards ox-

idation of NO under UV and visible light irradiation. Maximum activity was realised when using the photocatalyst containing 10% g-C₃N₄ under both irradiation conditions, reaching 59.4% and 12.6% NO removal after 60 min of UV and visible light exposure, respectively [207]. Upon integration of the NO instantaneous concentration over time, it was revealed that the photocatalyst with 10% g-C₃N₄ loading, removed 2.4 and 4.1 times more NO under UV illumination compared to TiO₂ and pristine g-C₃N₄, respectively, and 5.8 times more NO compared to g-C₃N₄ under visible light exposure. Good contact between TiO₂ and g-C₃N₄ allowed efficient charge separation and transfer, resulting to improved activity [207]. In a similar study, Giannakopoulou et al. engineered the band gap and band positions of g-C₃N₄/TiO₂ nanocomposites by varying the ratios of melamine/TiO₂ during synthesis. The hybrid nanostructures were investigated for the oxidation of NO under UV and visible light illumination [208]. It was observed that at a melamine/TiO₂ ratio of 1:4, the resultant composite photocatalyst (designated M0.2) showed the highest activity towards NO removal. Moreover, under UV irradiation its performance was comparable to that of TiO₂ while a significant enhancement was evident under visible light irradiation. This could be explained in terms of the band gap and fine-tuned band positions which allowed efficient separation of the charge carriers and minimised recombination [208].

Under visible light illumination, only g-C₃N₄ is excited and the electrons promoted to its conduction band are transferred to the conduction band of TiO₂ (Fig. 15a) where they are captured by adsorbed oxygen to form the superoxide radicals. The superoxide radicals alongside the valence band holes in g-C₃N₄ are involved in a series of reactions resulting in the oxidation of NO [207]. Accordingly, under UV light irradiation, both g-C₃N₄ and TiO₂ are excited

Table 3Summary of the photocatalytic properties of other g-C₃N₄/TiO₂ nanostructures towards pollution mitigation.

Material	Preparation method	Application	Optimum g-C ₃ N ₄ loading	Degradation efficiency	Enhancement factor over control	Reference
g-C ₃ N ₄ /TiO ₂ (TCN)	Solvothermal	Degradation of MB, RhB and ciprofloxacin (CIP)/Vis	66.7 wt%	99.3% in 150 min/RhB, 97.3% in 150 min/CIP, No data for MB	8.2/g-C ₃ N ₄ /RhB, 1.8/g-C ₃ N ₄ /MB, 14.8/g-C ₃ N ₄ /CIP	[219]
g-C ₃ N ₄ /TiO ₂	Calcination	Degradation of Acid orange 7/UV and Vis	No data	100% in 2 h/UV, 100% in 5 h/Vis	No data	[220]
g-C ₃ N ₄ nanosheets/TiO ₂	Wet chemical	Degradation of acetaldehyde/UV and Vis	94%	10% in 4 h/Vis, 45% in 4 h/UV	3/g-C ₃ N ₄ /Vis, 20/g-C ₃ N ₄ /UV	[221]
g-C ₃ N ₄ /TiO ₂	Calcination	Degradation of MB/Vis	20%	92% in 160 min	1.78/g-C ₃ N ₄	[222]
g-C ₃ N ₄ /TiO ₂ nanofiber	Self-assembly	Degradation of RhB/Simulated solar light	70%	82% in 80 min	4/TiO ₂ , 2.2/g-C ₃ N ₄	[218]
g-C ₃ N ₄ /seed grown mesoporous TiO ₂	Seed induced solvothermal	Degradation of MO/Vis	No data	No data	2–4/g-C ₃ N ₄ /direct grown meso. TiO ₂ , 29–37/g-C ₃ N ₄	[215]
g-C ₃ N ₄ /TiO ₂	solvothermal	Degradation of phenol/Simulated solar light	88.8 wt%	100% in 50 min	2.2/TiO ₂ , 2.8/g-C ₃ N ₄	[217]
g-C ₃ N ₄ /TiO ₂	Wet impregnation	Degradation of phenol/UV	2%	85% in 120 min	70%/TiO ₂	[223]
g-C ₃ N ₄ /TiO ₂ (Brookite)	Calcination	Degradation of MO and As ³⁺ oxidation	35 wt%	55% MO and As ³⁺ in 180 min	3.5/g-C ₃ N ₄ /MO	[212]
g-C ₃ N ₄ /TiO ₂ (B) nanofibers	Solvent evaporation	Degradation of sulforhodamine B (SRB)/Vis	1%	56.3% in 5 h	5.09/TiO ₂ (B), 4.96/g-C ₃ N ₄	[224]
g-C ₃ N ₄ /TiO ₂ (Anatase)	Solvent evaporation	Degradation of MB, RhB, acridine orange (AO) and 2,4-DCP/Vis	No data	No data	No data	[225]
Exfoliated g-C ₃ N ₄ /TiO ₂	Sol-gel	Degradation of RhB/Vis	5 wt%	No data	2.4/TiO ₂ , 7.0/N-TiO ₂	[226]
Mesoporous g-C ₃ N ₄ /TiO ₂	Hard templating	Degradation of RhB/Vis	No data	96.5% in 100 min	1.6/mp-g-C ₃ N ₄	[213]
g-C ₃ N ₄ /TiO ₂	Sonication	Degradation of MB/Vis and UV	1.5 g	95.32% in 120 min/UV, No data for Vis	6.92/g-C ₃ N ₄ /UV, 9.27/g-C ₃ N ₄ /Vis	[227]
g-C ₃ N ₄ /TiO ₂ (Anatase)	Wet impregnation	Degradation of toluene/Vis and UV	1 wt%	2.0 × 10 ^{−10} mols ^{−1} m ^{−2} /UV and Vis	1.3/g-C ₃ N ₄ /Vis, 1.4/g-C ₃ N ₄ /UV	[228]
g-C ₃ N ₄ /TiO ₂ nanotube array	Electrochemical	Degradation of MO/Vis	No data	100% in 2.5 h	No data	[100]

and the electrons transfer to the conduction band of TiO₂ while the holes transfer to the valence band of g-C₃N₄ [208]. The superoxide radicals and holes partake in the oxidation of NO and some of the important reactions are summarised in Eq. (27)–(31) [208,209].



Sridharan et al. employed a thermal transformation synthesis route whereby hydrothermally obtained C and N co-doped TiO₂ (TGU) using urea and D-glucose as C and N sources, respectively, was transformed to g-C₃N₄/TiO₂ via pyrolysis at 300 °C (TCN300) and 500 °C (TCN500) in air. The prepared heterostructures were examined for the visible light photocatalytic degradation of MB and reduction of Cr(VI) in aqueous solutions [210]. For the removal of both MB (Fig. 15b) and Cr(VI) (Fig. 15c), the nanocomposite pyrolysed at 300 °C displayed the highest activity, reaching ≈98% and 72% in 100 min for MB and Cr(VI) removal, respectively. This could be attributed to the formation of heterojunctions between g-C₃N₄ and TiO₂, promoting efficient visible light absorption and charge separation. During MB degradation, both the superoxide radicals and holes played an important role while for Cr(VI) reduction, the conduction band electrons on TiO₂ are responsible for reducing the toxic Cr(VI) to the less harmful Cr(III) [210]. Similarly, Mohini and Lakshminarasimhan recently used a hydrothermal

route to grow mesoporous TiO₂ nanoparticles on g-C₃N₄ sheets and investigated the photocatalytic performance of the resultant nanocomposites for the degradation of MO and reduction of Cr(VI) under visible light exposure [211]. It was observed that at a 2:1 weight ratio of g-C₃N₄/TiO₂, the composite photocatalyst showed the highest activity for both pollutants and the photocatalyst showed better Cr(VI) removal compared MO. Further enhancement in activity was realised when the photocatalytic experiments were performed at pH 3 and this could be ascribed to better interaction of the photocatalyst and the pollutant as a result of electrostatic forces at low pH [211]. Coupling g-C₃N₄ with mesoporous TiO₂ resulted in improved surface area, formation of the active species and efficient separation of the charge carriers. The holes accumulate on g-C₃N₄ while the electrons accumulate of TiO₂ where they are trapped by Cr(VI) and reduce it to Cr(III) and in the case of MO degradation, the electrons react with oxygen to form the radical species which alongside the holes decompose MO [211].

Zang et al. examined the visible light photocatalytic behaviour of brookite TiO₂ coupled with g-C₃N₄ (br-TiO₂/g-C₃N₄) towards MO degradation, water splitting and oxidation of As(III). The hybrid photocatalyst displayed superior activity over br-TiO₂ and g-C₃N₄, individually, and the photocatalyst containing 35% g-C₃N₄ showed the highest activity compared to anatase/rutile TiO₂/g-C₃N₄ hybrids [212]. After 180 min of visible light irradiation, 55% of MO and As(III) were removed while hydrogen generation reached 1058 μmol/g. Good contact between br-TiO₂ and g-C₃N₄ enabled the formation of heterojunctions and the band structure of the heterojunction is well positioned to facilitate degradation of MO by the holes and superoxide radicals on g-C₃N₄ and TiO₂, respectively.

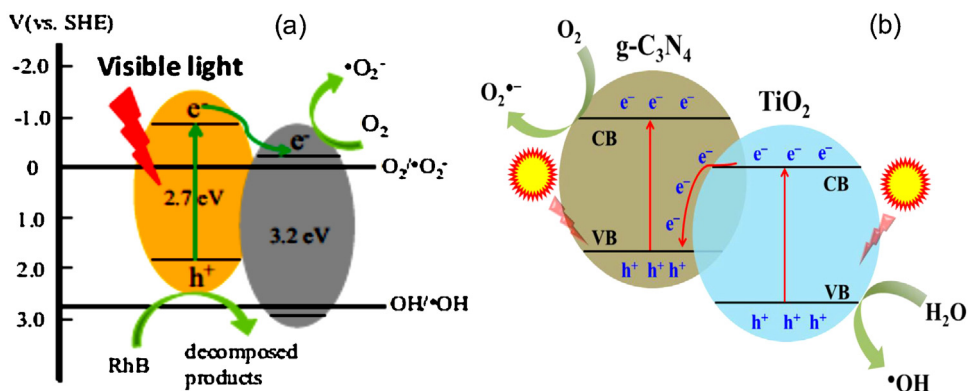


Fig. 16. Charge transfer mechanism in g-C₃N₄/TiO₂ under (a) visible light and (b) UV light irradiation.

(a) Reproduced with permission from Ref. [203], Copyright 2015, Elsevier. (b) Reproduced with permission from Ref. [216], Copyright 2015, Elsevier.

Meanwhile, the valence band holes of g-C₃N₄ are positive enough to oxidise the toxic As(III) to the less harmful As(V) [212]. Table 3 summarises the photocatalytic properties of other g-C₃N₄/TiO₂ nanocomposites obtained using various methods for application in the decontamination of the environment. Although all the materials are composed of g-C₃N₄ and TiO₂, they show different photocatalytic properties towards various pollutants and morphologies owing to the different preparation methods and starting materials.

In terms of the photocatalytic degradation mechanism of the organic pollutants, it is generally accepted that the combined contribution of TiO₂ and g-C₃N₄ is essential for the improved activity. Under visible light illumination (Fig. 16a), only g-C₃N₄ absorbs visible light and electrons are promoted to the conduction band leaving holes in the valence band [203,204]. The well-matched band potentials of g-C₃N₄ and TiO₂ allows for the transfer of electrons from the conduction band of g-C₃N₄ (−1.12 eV vs NHE) which is more negative, to the conduction band of TiO₂ (−0.4 eV vs NHE) which is less negative. The TiO₂ conduction band electrons are then trapped by adsorbed oxygen to form the superoxide radicals which then attack the pollutant molecules [203,213,214]. Accordingly, the valence band holes remain in g-C₃N₄ where they directly oxidise the pollutant molecules since they are not positive enough to oxidise water to form the hydroxyl radicals [213,215]. Efficient charge separation is attained in the g-C₃N₄/TiO₂ heterojunction since the electrons and holes are located on different parts of the nanocomposite. Similar mechanisms have been proposed for NO oxidation and bacterial inactivation over g-C₃N₄/TiO₂ nanocomposites under visible light irradiation [67,206].

Under UV irradiation (Fig. 16b), both g-C₃N₄ and TiO₂ are activated and electrons are promoted from their valence bands to the conduction bands. TiO₂ conduction band electrons are subsequently transferred to the valence band of g-C₃N₄ in a typical Z-scheme mechanism [205,216]. The holes remain in valence band of TiO₂ which is positive enough to oxidise water to form the hydroxyl radicals which are strong oxidising agents towards pollutants. Similarly, the electrons in the conduction band of g-C₃N₄ are trapped by adsorbed oxygen to form the superoxide radicals [205,216]. Other reports have proposed a typical heterojunction type of mechanism whereby the electrons from the conduction band of g-C₃N₄ are transferred to the conduction band of TiO₂ where they are trapped by oxygen to form the superoxide radicals. Meanwhile, the holes in TiO₂ transfer to the valence band of g-C₃N₄ where they are directly involved in the oxidation of the pollutants [203,206,217,218]. Compared to the Z-scheme mechanism which results in the formation of both hydroxyl and superoxide radicals, the heterojunction type of mechanism yields holes and superoxide radicals which are both weaker oxidising agents compared to the hydroxyl radical. Therefore, this means that higher photocat-

alytic activity is likely to be attained via the Z-scheme mechanism compared to the heterojunction type.

Zinc oxide (ZnO) is another important and prominent wide band gap (3.2 eV) semiconductor with good oxidation potential, relatively inexpensive and often shows higher photocatalytic activity than TiO₂ towards some pollutants [229,230]. However, poor visible light utilisation, high recombination rate of charge carriers and photocorrosion are the major drawbacks associated with pure ZnO [230–232]. It seems reasonable to couple ZnO with g-C₃N₄ in order to benefit from the combined properties of the two semiconductors towards improvement of the photocatalytic performance of the composite photocatalyst. Dumbbell and cone shaped ZnO nanostructures were hybridised with g-C₃N₄ under refluxing conditions to form g-C₃N₄/ZnO (D) (dumbbell shaped) and g-C₃N₄/ZnO (C) (cone shaped) heterostructures and their photocatalytic behaviour was investigated through visible light photocatalytic degradation of MB and phenol [233]. Both heterostructures displayed superior photocatalytic activity over pure g-C₃N₄ for both MB and phenol decomposition. About 99% MB degradation was attained by both heterostructures after 140 min, however, the activity for g-C₃N₄/ZnO (D) was 4 times higher while that of g-C₃N₄/ZnO (C) was 3 times higher than that of pure g-C₃N₄. For phenol degradation, 100% degradation was reached in 150 min and 170 min by g-C₃N₄/ZnO (D) and g-C₃N₄/ZnO (C), respectively [233]. The slightly higher photocatalytic activity of g-C₃N₄/ZnO (D) could be due to the higher surface area of g-C₃N₄/ZnO (D) (45.35 m²/g) compared to g-C₃N₄/ZnO (C) (23.67 m²/g) which provide a larger reaction environment and increased interaction with the pollutant molecules [233].

Mesoporous ZnO nanotriangles (ZnO-nt) were coupled with varying amounts of g-C₃N₄ using a sono-chemical impregnation method to form hybrid nanostructures (g-C₃N₄/ZnO-nt). Graphitic-C₃N₄/ZnO-nt heterostructures were evaluated for RhB decomposition under simulated solar light exposure. RhB degradation reached 100% after 60 min when the sample with a 20% g-C₃N₄ loading (g-C₃N₄/ZnO-nt (20%)) was used [234]. Yu et al. observed enhanced CO₂ reduction to methanol over g-C₃N₄/ZnO heterostructures prepared via a simple calcination approach. An enhancement factor of 2.3 was observed from the photocatalytic activity of the heterostructures over pure g-C₃N₄ [235]. Most importantly, these heterostructures showed higher CO₂ reduction while maintaining their selectivity towards conversion of CO₂ to methanol [235]. Equally, g-C₃N₄/ZnO nanocomposite prepared via a simple impregnation route, showed improved photocatalytic CO₂ conversion to fuel under simulated solar light compared to g-C₃N₄ and P25. The photocatalytic active of g-C₃N₄/ZnO was 4.9 and 6.4 times higher than that of g-C₃N₄ and P25, respectively [236].

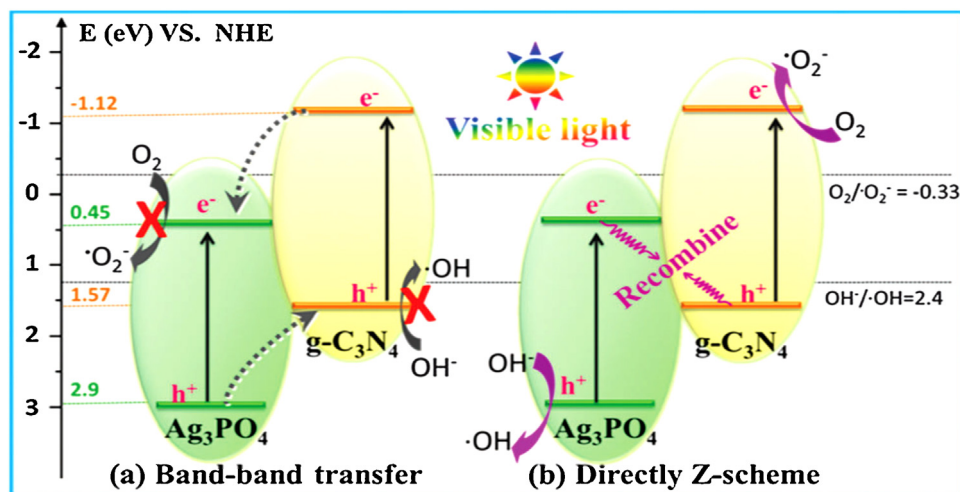


Fig. 17. Schematic of the possible charge transfer mechanisms in $g\text{-C}_3\text{N}_4/\text{Ag}_3\text{PO}_4$.

Reproduced with permission from Ref. [240]. Copyright 2015, RSC.

In terms of the photocatalytic degradation mechanism, it has been proposed that under visible light illumination, the heterojunction type of mechanism prevails, since only $g\text{-C}_3\text{N}_4$ absorbs in the visible region and the conduction band electrons are transferred to ZnO conduction band due to its lower band potential (-0.28 eV). Meanwhile, the holes remain in the valence band of $g\text{-C}_3\text{N}_4$ and directly oxidise pollutants to form the degradation products [233]. However, the ZnO conduction band electrons are not negative enough to reduce oxygen to form the superoxide radicals but they can be involved in direct reduction of the pollutants, therefore the main active species would be the holes and to a very small extent, the superoxide radicals [232]. Under simulated solar light which contains small amounts of UV, both ZnO and $g\text{-C}_3\text{N}_4$ are excited and electron transfer follow a typical Z-scheme mechanism. Instead of the $g\text{-C}_3\text{N}_4$ conduction band electrons transferring to the conduction band of ZnO , the ZnO conduction band electrons are transferred to the valence band of $g\text{-C}_3\text{N}_4$. At the ZnO valence band, holes react with water to form the hydroxyl radicals while at the conduction band of $g\text{-C}_3\text{N}_4$, superoxide radicals are formed [234]. A similar mechanism has also been put forward for CO_2 reduction over $g\text{-C}_3\text{N}_4/\text{ZnO}$ under simulated solar light [235]. A heterojunction type of mechanism has also been proposed for CO_2 conversion to fuel over $g\text{-C}_3\text{N}_4/\text{ZnO}$ under simulated solar light [236]. Unfortunately, the authors did not provide any experimental evidence that points in the direction of a heterojunction type of mechanism. Only the band structure of $g\text{-C}_3\text{N}_4$ and ZnO was used to formulate the proposed mechanism, which lacks convincing evidence since any of the two mechanisms would still be possible. With the mechanism under visible light irradiation unanimously accepted, careful analysis needs to be done when proposing the mechanism under simulated solar light.

Silver containing compounds form another important category of candidates to couple with $g\text{-C}_3\text{N}_4$. High utilisation of visible light is one of the most important properties of most silver containing compounds and it is often extensively exploited in photocatalytic applications. Silver phosphate (Ag_3PO_4) has been an interesting development towards improving the activity of $g\text{-C}_3\text{N}_4$ through formation of binary nanocomposites. On its own, Ag_3PO_4 is a visible light active, mild band gap ($\sim 2.45\text{ eV}$) semiconductor with good photocatalytic activity but its poor photostability and large usage of silver, hinders its practical exploitation [237,238]. Graphitic carbon nitride/ Ag_3PO_4 nanocomposites ($g\text{-C}_3\text{N}_4/\text{Ag}_3\text{PO}_4$) with varying $g\text{-C}_3\text{N}_4:\text{Ag}_3\text{PO}_4$ ratios were fabricated using simple solvent evaporation and studied for the degradation of ethylene

under visible light exposure [239]. Highly enhanced activity and good photostability was observed from the sample containing 70% $g\text{-C}_3\text{N}_4 + 30\% \text{Ag}_3\text{PO}_4$, showing 3.47 and 12.38 times the activity of Ag_3PO_4 and $g\text{-C}_3\text{N}_4$, respectively. Additionally, the sample was found to be stable over five cycles, showing a very small decline in activity [239]. A direct Z-scheme mechanism was proposed to explain the enhanced activity in the nanocomposites. Meng et al. studied the charge carriers' transfer mechanism in $g\text{-C}_3\text{N}_4/\text{Ag}_3\text{PO}_4$ heterostructures during MB degradation under visible light irradiation and observed that the charge transfer mechanism depends on the major component of the nanocomposite [240]. If Ag_3PO_4 was the major component, the mechanism favoured the heterojunction type of mechanism (band–band transfer) (Fig. 17a) whereby the electrons accumulate in the conduction band of Ag_3PO_4 while the holes are located in the valence band of $g\text{-C}_3\text{N}_4$. In this case there is no direct formation of the hydroxyl and superoxide radicals from oxidation of H_2O and O_2 , respectively, leading to lower photocatalytic activity [240]. However, if $g\text{-C}_3\text{N}_4$ was the major component, the transfer mechanism favoured the Z-scheme route (Fig. 17b) whereby the both the superoxide and hydroxyl radicals are formed at the conduction band of $g\text{-C}_3\text{N}_4$ and valence band of Ag_3PO_4 , respectively. The formation of these strong oxidising agents lead to the higher photocatalytic activity observed [240].

Silver carbonate (Ag_2CO_3) is another mild band gap ($\sim 2.3\text{ eV}$) silver containing semiconductor with good visible light activity which has been explored for hybridisation with $g\text{-C}_3\text{N}_4$. Silver carbonate nanoparticles were loaded on $g\text{-C}_3\text{N}_4$ nanosheets and the hybrid photocatalyst showed remarkable activity towards MO and RhB under visible light irradiation [241]. The sample containing 30% Ag_2CO_3 (MN-30) showed the highest activity for both dyes, suggesting that 30% was the optimum loading. Complete degradation of RhB was observed after just 30 min of irradiation over MN-30 and this could be due to its large specific surface area, efficient charge separation and visible light utilisation [241]. Shi et al. recorded 100% RhB degradation in 40 min of visible light illumination over $g\text{-C}_3\text{N}_4/\text{Ag}_2\text{CO}_3$ nanocomposite. Its photocatalytic activity was nearly 8 times the activity of pure $g\text{-C}_3\text{N}_4$ under the same experimental conditions [242]. An *in situ* growth strategy was used to deposit Ag_2CO_3 nanoparticles on $g\text{-C}_3\text{N}_4$ nanosheets and the nanocomposite photocatalyst was investigated for RhB degradation under visible light irradiation [243]. The composite photocatalyst showed the highest activity which was 5.5 and 4 times higher than the activity of Ag_2CO_3 and $g\text{-C}_3\text{N}_4$, respectively. This was credited to the combined contribution of $g\text{-C}_3\text{N}_4$ and Ag_2CO_3 resulting to strong

visible light absorption, high photostability, large specific surface area and efficient electro/hole separation and transfer [243].

A typical heterojunction type of mechanism (similar to Fig. 17a) has been proposed for the degradation of pollutants over $g\text{-C}_3\text{N}_4/\text{Ag}_2\text{CO}_3$ under visible light irradiation. Electrons transfer from the conduction band of $g\text{-C}_3\text{N}_4$ to the conduction band of Ag_2CO_3 while the holes migrate to the valence band of $g\text{-C}_3\text{N}_4$ upon absorption and excitation by visible light [241,243–245]. According to this mechanism, the electrons in the conduction band of Ag_2CO_3 cannot reduce oxygen due to the positive band potential (+0.37 eV) while the holes in the valence band of $g\text{-C}_3\text{N}_4$ are also not positive enough to oxidise water to form the hydroxyl radicals, instead they are directly involved in oxidation of the pollutants [241,243–245]. Therefore, the only active species should be the holes. However, radical scavenging experiments have detected the presence of holes, hydroxyl and superoxide radicals as active species during degradation. Moreover, PL studies have also confirmed the generation of hydroxyl radicals during degradation [241,244,245]. These observations could possibly suggest that there could be another underlying mechanism for electron transfer in the $g\text{-C}_3\text{N}_4/\text{Ag}_2\text{CO}_3$ heterojunctions. One such possibility would be a Z-scheme mechanism (similar to Fig. 17b) whereby the electrons in the conduction band of Ag_2CO_3 migrate to the valence band of $g\text{-C}_3\text{N}_4$. Consequently, the valence band holes in Ag_2CO_3 can be trapped by H_2O to form the hydroxyl radicals while the conduction band electrons in $g\text{-C}_3\text{N}_4$ are negative enough to reduce oxygen to form the superoxide radicals. In this case not only will charge separation be attained but the activity will also be greatly enhanced. Another point of consideration concerning the heterojunction type of mechanism proposed is the issue of photocorrosion of Ag_2CO_3 , which is most likely to occur faster in this case since there are electrons accumulating in its conduction band. However, in the Z-scheme mechanism, electrons will be kept away from Ag_2CO_3 , thereby minimising the rate of photocorrosion and improved photostability. Therefore, careful analysis still needs to be done to ascertain the actual electron transfer mechanism in these heterostructures.

Silver halides (AgCl , AgI and AgBr) are well known photosensitive materials with a long history of applications in photography (AgBr/I) and also display interesting photocatalytic behaviour. Coupling $g\text{-C}_3\text{N}_4$ with silver halides to form heterostructures such as $g\text{-C}_3\text{N}_4/\text{AgBr}$ [246–248], $g\text{-C}_3\text{N}_4/\text{AgI}$ [247,249] and $g\text{-C}_3\text{N}_4/\text{AgCl}$ [248,250,251] has been found to enhance the photocatalytic activity of these materials towards various organic and inorganic pollutants under visible light irradiation. The well-matched band potentials between the silver halides and $g\text{-C}_3\text{N}_4$ allows for efficient separation and transfer of the photogenerated charge carriers. Additionally, the hybrid materials also showed good photostability and improved utilisation of visible light due to the synergy between the silver halide and $g\text{-C}_3\text{N}_4$ achieved via formation of the heterojunction [246,248,251]. During pollutant degradation, charge transfer proceeds via the heterojunction type of mechanism. Both $g\text{-C}_3\text{N}_4$ and the silver halide are excited by visible light, with electrons promoted to their conduction bands leaving the holes in the valence band. The holes and electrons transfer in the opposite directions depending on the band structure of the materials in question but the overall result is efficient separation of the charge carriers [248,249]. Several other silver based photocatalyst/ $g\text{-C}_3\text{N}_4$ heterostructures such as $g\text{-C}_3\text{N}_4/\text{Ag}_2\text{O}$ [252,253], $g\text{-C}_3\text{N}_4/\text{Ag}_2\text{WO}_4$ [254] and $g\text{-C}_3\text{N}_4/\text{AgVO}_3$ [255] have shown improved photocatalytic properties towards various pollutants under visible light illumination owing to the collaborative effect of the coupled materials. Coupling the silver based semiconductors with $g\text{-C}_3\text{N}_4$ ensures sustainable utilisation of silver since only small amounts are used in the nanocomposites compared to when these silver based semiconductors are used on their own.

Iron oxides (Fe_2O_3 and Fe_3O_4) have been explored to modify $g\text{-C}_3\text{N}_4$ and the hybrid photocatalyst have shown remarkable photocatalytic activity compared to the individual materials [256,257]. Magnetically separable $g\text{-C}_3\text{N}_4/\text{Fe}_3\text{O}_4$ nanocomposites with 77–92.5% $g\text{-C}_3\text{N}_4$ loadings were fabricated by an *in situ* growth mechanism of Fe_3O_4 nanoparticles on $g\text{-C}_3\text{N}_4$ nanosheets [258]. The highest activity towards RhB degradation was observed from the sample containing 84.8% $g\text{-C}_3\text{N}_4$ and its activity was 7 times higher than the activity of $g\text{-C}_3\text{N}_4$. Lin et al. prepared ultrafine Fe_2O_3 nanoparticles decorated on $g\text{-C}_3\text{N}_4$ ($g\text{-C}_3\text{N}_4/\text{Fe}_2\text{O}_3$) via a facile thermal polymerisation and deposition-precipitation route and studied the photocatalytic properties of the hybrid material for the decomposition of RhB under simulated solar light illumination [259]. At a loading of 0.1 wt% Fe_2O_3 , the nanocomposite displayed the highest activity which was 3 and 69 times higher than the photocatalytic activity of $g\text{-C}_3\text{N}_4$ and Fe_2O_3 , respectively [259]. Incorporation of the iron oxide nanoparticles into $g\text{-C}_3\text{N}_4$ had been found to greatly enhance charge separation and transfer and enhanced the stability of the photocatalyst. Moreover, the magnetic properties of the iron oxide nanoparticles allows for easy separation of the photocatalyst from the treated water using an external magnetic field [256,258,260]. This does not only make recycling the photocatalyst easy but also minimise secondary pollution by the photocatalyst particles.

Ferrites such as NiFe_2O_4 , CuFe_2O_4 and ZnFe_2O_4 with narrow band gaps of 2.19, 1.4 and 1.9 eV, respectively, are other useful iron oxide based p-type semiconductors with good adsorption in the visible light region and strong magnetic properties [261,262]. Prompted by these fascinating properties, $g\text{-C}_3\text{N}_4/\text{NiFe}_2\text{O}_4$ [262], $g\text{-C}_3\text{N}_4/\text{CuFe}_2\text{O}_4$ [261] and $g\text{-C}_3\text{N}_4/\text{ZnFe}_2\text{O}_4$ [263] nanostructures have been prepared and investigated for the decomposition of various pollutants under visible light exposure. The $g\text{-C}_3\text{N}_4$ /ferrite composite photocatalysts showed significantly improved photocatalytic activity compared to the ferrite and $g\text{-C}_3\text{N}_4$ individually. This could be ascribed to strong visible light utilisation (Fig. 18a) and charge separation and transfer due to the *p-n* junction formed at the $g\text{-C}_3\text{N}_4$ /ferrite interface [261–263]. Under visible light illumination, both the ferrite and $g\text{-C}_3\text{N}_4$ are excited and electrons are promoted to their conduction bands while leaving holes in the valence bands. Depending on the band structures of the materials involved, the charge carriers will transfer in the opposite direction, thereby ensuring efficient charge separation and formation of the active species [261–263]. Additionally, the magnetic nature of the ferrites facilitates easy separation of the photocatalyst from solution as shown in Fig. 18b [262].

Cadmium sulphide (CdS) is another important, mild band gap semiconductor (2.4 eV) with good visible light response but its poor photostability, high recombination rate of the charge carriers and aggregation are some of the major setbacks of using pure CdS in photocatalytic application such as pollutant degradation [264]. Xu and Zhang reported that $g\text{-C}_3\text{N}_4/\text{CdS}$ nanohybrids with a $g\text{-C}_3\text{N}_4:\text{CdS}$ ratio of 1:0.8 (denoted CNCd0.8) showed higher photocatalytic activity towards RhB and metronidazole (MTZ) degradation compared to $g\text{-C}_3\text{N}_4$, CdS and their physical mixture [265]. It was observed that for RhB, over 95% was decomposed after 80 min while 98% of MTZ was degraded after 5 h of visible light irradiation over CNCd0.8 [265]. Wang et al. observed that small amounts of CdS (1%) significantly enhanced the activity of the hybrid nanostructure towards RhB degradation under visible light irradiation. Furthermore, the hybrid material showed remarkable stability with no significant loss of photoactivity in the five cycles that it was reused [266]. Similar results have been reported elsewhere [267,268]. Since both $g\text{-C}_3\text{N}_4$ and CdS are visible light responsive, both are excited upon illumination with visible light and electrons are excited from their valence bands to the conduction bands. Electrons will transfer from the conduction band

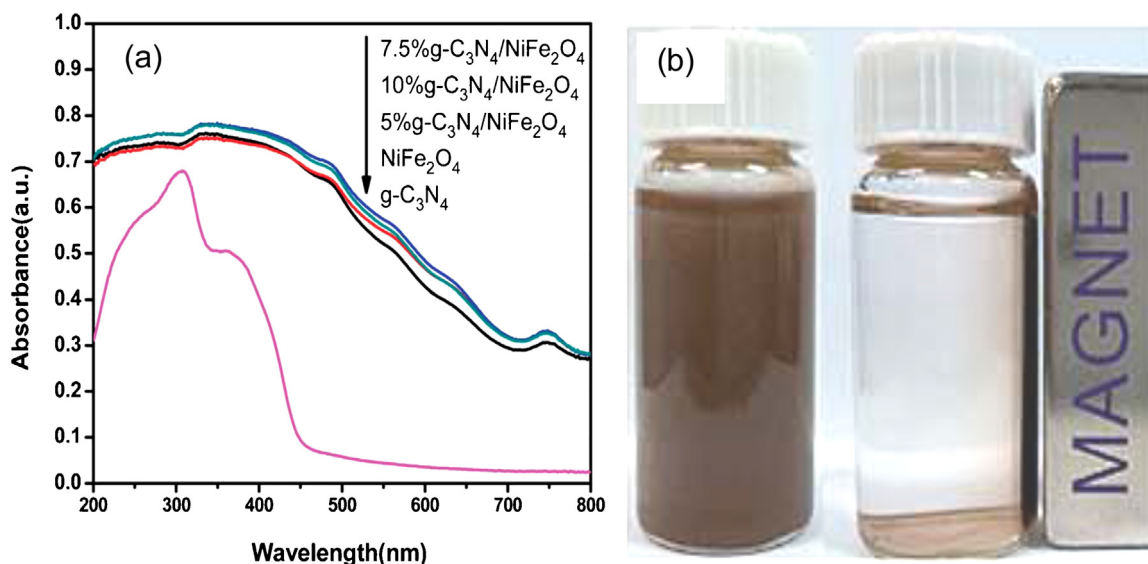


Fig. 18. (a) UV-vis diffuse reflectance spectra and (b) magnetic separation of 7.5% g-C₃N₄/NiFe₂O₄ from solution.

Reproduced with permission from Ref. [262]. Copyright 2015, RSC.

of g-C₃N₄ to the conduction band of CdS which is less negative (−0.48 eV) where they are trapped by oxygen to form the radical species. Meanwhile, the holes will transfer from CdS (+1.75 eV) to the valence band of g-C₃N₄ where they directly oxidise the organic pollutants [264,266–268]. The efficient separation of the charge carriers ultimately results to improved photocatalytic activity. Moreover, coupling g-C₃N₄ and CdS improve the stability of the material and minimise aggregation of CdS nanoparticles [268].

In recent years, bismuth based semiconductors such as Bi₂CO₃, Bi₂S₃, Bi₂O₃, BiOX (X = Br, Cl and I), BiVO₄, BiWO₆, BiOI₄, Bi₂MoO₆ and Bi₂O₂CO₃ have emerged as attractive materials in various photocatalytic applications. Among these materials, the bismuth oxyhalides (BiOX) have shown interesting photocatalytic properties [107]. Graphitic carbon nitride/bismuth oxyhalides hybrid nanostructures such as g-C₃N₄/BiOCl [269–274], g-C₃N₄/BiOBr [107,275–278] and g-C₃N₄/BiOI [279] have been prepared and showed remarkable improvement in photocatalytic activity compared to g-C₃N₄ and the oxyhalides individually, towards removal of organic and inorganic pollutants. For example, g-C₃N₄ hybridised with nanosized BiOCl showed remarkable visible light photocatalytic activity towards RhB, reaching 99.5% RhB removal in just 30 min of irradiation and this was 44 times higher than the activity of pristine g-C₃N₄ [269]. Meanwhile, (2D) g-C₃N₄/BiOBr nanojunctions displayed improved visible light-driven photocatalytic removal of NO compared to BiOBr and g-C₃N₄, individually. The activity of the hybrid photocatalyst was found to be 2 times that of pure BiOBr [278]. This enhancement was credited to efficient separation and transfer of the charge carriers owing to the well-matched band structure, layered 2D nanojunctions and perfectly hybridised crystal planes. Moreover, coupling g-C₃N₄ with BiOBr increased the surface area of the nanocomposite, which played a positive role during NO removal [278].

Although g-C₃N₄/BiOI₃ [280] and g-C₃N₄/BiOI₄ [281] hybrids displayed enhanced photocatalytic activity, g-C₃N₄/BiOI was shown to be less active due to the poorly matched band potentials which limit charge separation and transfer [282]. However, in a recent study, Wang et al. demonstrated that g-C₃N₄/BiOI heterostructures prepared *via* simple deposition route could be useful in the photocatalytic reduction of CO₂ to yield CO, H₂ and/or CH₄, under visible light illumination [283]. The heterostructures displayed higher activity towards CO₂ removal compared to pristine g-C₃N₄ and BiOI, individually. This could be ascribed to the forma-

tion of a heterojunction between the two materials which allowed efficient charge transfer in an indirect Z-scheme mechanism. I[−]/I₃[−] ions were detected as intermediates and were found to act as transport agents for charge across the g-C₃N₄/BiOI heterojunctions which minimised recombination and improved the photocatalytic reduction of CO₂ [283].

It is unanimously accepted that the charge carrier transfer mechanism in g-C₃N₄/BiOX nanostructures follow a typical heterojunction route under visible light exposure as depicted in Fig. 19a. The holes accumulate on g-C₃N₄ where they oxidise the organic pollutants on the photocatalyst surface while the electrons transfer to the conduction band of the oxyhalides. Efficient charge separation is attained since the electrons and holes are kept at different parts of the hybrid nanostructure [271,273,276].

A typical Z-scheme mechanism (Fig. 19b) was proposed to explain the charge transfer mechanism in g-C₃N₄/BiOCl during RhB degradation under UV light illumination. In this case, both g-C₃N₄ and BiOCl are excited upon UV light absorption and electrons are promoted to their conduction bands leaving holes in the valence bands. Subsequently, the electrons in the conduction band of BiOCl are transferred to the valence band of g-C₃N₄. This results in the formation of superoxide radicals at the conduction band of g-C₃N₄ upon reaction with oxygen [270]. Both the BiOCl holes and superoxide radical are the important oxidising species responsible for pollutant decomposition.

Other bismuth based semiconductor/g-C₃N₄ heterostructures such as g-C₃N₄/Bi₂O₂CO₃ [284–286], g-C₃N₄/BiVO₄ [287–290], g-C₃N₄/Bi₂MoO₆ [291–293], g-C₃N₄/Bi₂O₃ [294,295], g-C₃N₄/Bi₄O₅I₂ [296], g-C₃N₄/BiWO₆ [297–299], g-C₃N₄/Bi₂S₃ [300,301], g-C₃N₄/BiFeO₃ [302], g-C₃N₄/Bi₅Nb₃O₁₅ [303] and g-C₃N₄/tz-Bi_{0.92}Gd_{0.08}VO₄ [304] have been investigated for the photocatalytic degradation of various pollutants under both UV and visible light illumination. It was observed that the coupled nanostructures were more photocatalytic active compared to the individual materials which could be ascribed to the formation of the heterojunction that allowed a collaborative effect to be realised between the hybridised materials. A host of other binary nanocomposites (Table 4) have been prepared and evaluated for the degradation of various organic and inorganic pollutants.

Table 4
Summary of the photocatalytic properties of other g-C₃N₄ based binary heterostructures.

Material	Preparation method	Application	Optimum g-C ₃ N ₄ loading	Degradation efficiency	Enhancement factor over control	Reference
g-C ₃ N ₄ /g-C ₃ N ₄ (Type I and Type II)	Calcination	NO removal/Vis	No data	41.3% in 30 min	No data	[305]
g-C ₃ N ₄ /Al ₂ O ₃	<i>In situ</i> thermal route	NO removal/Vis	11.99%	71.1% in 30 min	No data	[209]
g-C ₃ N ₄ /PdCl ₂	Wet impregnation/reduction	NO removal/Vis	99 wt%	65% in 40 min	33%/g-C ₃ N ₄	[306]
g-C ₃ N ₄ /Formate (F-g-C ₃ N ₄)	Hydrothermal	Cr(VI) reduction/Vis	98 wt%	55% in 4 h	3.32/g-C ₃ N ₄	[307]
g-C ₃ N ₄ /WO ₃	Mixing-calcination	Degradation of acetaldehyde/Vis	20 wt%	100% in 24 h	No data	[308]
g-C ₃ N ₄ /In ₂ O ₃	Hydrothermal	H ₂ generation and CO ₂ reduction/Vis	90 wt%	3.95 μmol in 4 h/H ₂ , 76.7 ppm CH ₄ in 4 h/CO ₂	3.0/g-C ₃ N ₄ , 4/In ₂ O ₃ /CO ₂ and 5/g-C ₃ N ₄ /H ₂	[309]
g-C ₃ N ₄ /BiPO ₄	Ultrasonic dispersion	Degradation of MB/UV	4 wt%	90% in 5 min	4.5/P25, 2.5/BiPO ₄	[310]
ZnO/mpg-C ₃ N ₄	Ultrasonic dispersion	Degradation of MB/UV/Vis	4 wt%/UV, 20 wt%/Vis	No data	2.0/ZnO/UV, 5/mpg-C ₃ N ₄ /Vis	[311]
g-C ₃ N ₄ /SrFeO _{3-x}	Sintering	Degradation of chloramphenicol (CAP) and crystal violet (CV)/Vis	96 wt%	91.3% in 96 h/CAP, 99.9% in 12 h	No data	[312]
g-C ₃ N ₄ /SnNb ₂ O ₆	Two-step wet chemistry	Degradation of MB/Vis	70 wt%	99% in 4 h	3.9/g-C ₃ N ₄ , 3.2/SnNb ₂ O ₆	[313]
g-C ₃ N ₄ /CeO ₂	Hard templating	CO ₂ reduction/Vis	97 wt%	0.694 μmol/h/CH ₄	No data	[314]
g-C ₃ N ₄ /SnS ₂	Ion-exchange	Degradation of MO/Vis	96 wt%	95.3% in 25 min	2.4/g-C ₃ N ₄	[315]
mpg-C ₃ N ₄ /Co ₃ O ₄	Hard templating-impregnation	Degradation of bisphenol/Vis	98.5%	93.6% in 180 min	No data	[316]
g-C ₃ N ₄ /WO ₃	Planetary milling	Oxidation of acetaldehyde/Vis	40%	60% in 48 h	2.0/g-C ₃ N ₄	[317]
g-C ₃ N ₄ /SnNb ₂ O ₆	3-step wet chemistry	Degradation of MB/Vis	70%	99% in 240 min	3.9/g-C ₃ N ₄ , 3.3/SnNb ₂ O ₆	[318]
g-C ₃ N ₄ /CeO ₂	Hydrothermal	Degradation of MB/Vis	95%	99% in 210 min	7.8/g-C ₃ N ₄	[319]
g-C ₃ N ₄ /Cu ₂ (OH)PO ₄	Hydrothermal	Degradation of RhB/Vis	70%	No data	12/Cu ₂ (OH)PO ₄ , 2.4/g-C ₃ N ₄	[320]
g-C ₃ N ₄ /GdVO ₄	Milling and heating	Degradation of RhB/Vis	90%	96.7% in 90 min	3.1/g-C ₃ N ₄ , 36/GdVO ₄	[321]
g-C ₃ N ₄ /BaTiO ₃	Mixing and calcination	Degradation of MO/Simulated solar light	12%	76% in 360 min	No data	[322]
g-C ₃ N ₄ /MoO ₃	Mixing-calcination	Degradation of MO/Vis	78.1%	No data	10.4/g-C ₃ N ₄	[323]
g-C ₃ N ₄ /Zn ₂ SnO ₄	Calcination	Degradation of RhB/Vis	89.6 wt%	No data	3.2/g-C ₃ N ₄ , 38/Zn ₂ SnO ₄	[324]
g-C ₃ N ₄ /ZnS	Anion exchange	Degradation RhB/Vis	86%	100% in 75 min	37.8/ZnS, 2.8/g-C ₃ N ₄	[325]
g-C ₃ N ₄ /ZnIn ₂ S ₄	Hydrothermal	Degradation of phenol and MO/Vis	40 wt%	95.3% in 120 min/MO, 73.2% in 240 min/phenol	No data	[326]
g-C ₃ N ₄ /SiO ₂	Mixing-calcination	Degradation of RhB/Vis	40%	94.3% in 150 min	3.5/g-C ₃ N ₄	[327]
g-C ₃ N ₄ /HSbO ₃	Mixing-calcination	Degradation of RhB/Vis	12.5 wt%	90% in 240 min	No data	[328]
g-C ₃ N ₄ /WO ₃	Mixing-calcination	Degradation of RhB/Simulated solar light	30%	91% in 90 min	2.5/g-C ₃ N ₄ , 52.2/WO ₃	[329]
g-C ₃ N ₄ /Cd _{0.2} Zn _{0.8} S	Hydrothermal	Degradation of phenol and RhB/Vis	20%	95.8% in 80 min/RhB, 76.1% in 180 min/phenol	No data	[330]
g-C ₃ N ₄ /In ₂ S ₃	Hydrothermal	Degradation of RhB/Vis	60%	96% in 30 min	1.4/g-C ₃ N ₄ and In ₂ S ₃ mixture	[331]
g-C ₃ N ₄ /NiO	Calcination	Degradation of MB	93.7%	100% in 40 min	2.3/NiO	[332]
g-C ₃ N ₄ /V ₂ O ₅	<i>In situ</i> growth	Degradation of RhB/Vis	99 wt%	95.5% in 60 min	7.3/g-C ₃ N ₄ , 13.0/V ₂ O ₅	[333]
g-C ₃ N ₄ /CeO ₂	Hard templating-calcination	CO ₂ reduction/Vis	97%	0.694 μmol/h in 60 min	No data	[314]
g-C ₃ N ₄ /Zn _{1-x} Cd _x S	Calcination-hydrothermal	Degradation of RhB/Vis	No data	97.9% in 90 min min	37.7/0.1 g-C ₃ N ₄ /ZnS	[334]
g-C ₃ N ₄ /V ₂ O ₅	Solvent evaporation-calcination	Degradation of RhB/Vis	60.3%	No data	No data	[335]
g-C ₃ N ₄ /NiTiO ₃	Calcination	Degradation of nitrobenzene/Vis	18.4 wt%	80% in 120 min	16/NiTiO ₃	[336]
g-C ₃ N ₄ /B ₄ C	Solvent evaporation	CO ₂ reduction/Vis	83.3%	0.84 mol g ⁻¹ h ⁻¹	6/g-C ₃ N ₄ , 8/B ₄ C	[337]
g-C ₃ N ₄ /SnO ₂	Mixing-calcination	Degradation of MO/Vis	52.5%	73% in 180 min	6/g-C ₃ N ₄	[338]
g-C ₃ N ₄ /ZrO ₂	Calcination	Degradation of RhB/Vis	79.1%	No data	2.33/g-C ₃ N ₄	[339]
g-C ₃ N ₄ /NaNbO ₃	Solid phase calcination	Degradation of RhB, MO and tetracycline (TC)/Vis	No data	93.6% in 120 min/RhB, 77.2% in 180 min/MO, 73.3% in 180 min/TC	2.7/g-C ₃ N ₄	[340]
g-C ₃ N ₄ /V ₂ O ₅	Wet-impregnation	Degradation of Direct Red 81 (DR81)	No data	No data	No data	[341]
g-C ₃ N ₄ /ZnS	Hydrothermal	Degradation of MO/Simulated solar light	10 wt%	93% in 100 min	4.3/g-C ₃ N ₄ , 3.6/ZnS	[342]

Table 4 (Continued)

Material	Preparation method	Application	Optimum g-C ₃ N ₄ loading	Degradation efficiency	Enhancement factor over control	Reference
g-C ₃ N ₄ /SnS ₂	Ultrasonic dispersion	Degradation of RhB and phenol/Vis	95 wt%	99.8% in 20 min/RhB, 95% in 40 min/MO, 31.3% in 120 min/phenol	4/g-C ₃ N ₄ , 8/SnS ₂	[343]
g-C ₃ N ₄ /HWO ₄	Impregnation	Degradation of RhB/Vis	90%	81.3% in 50 min	20/g-C ₃ N ₄	[344]
g-C ₃ N ₄ /Zn ₃ (OH) ₂ V ₂ O ₇ ·2H ₂ O	Hydrothermal	Degradation of MB/Vis	95 wt%	No data	1.9/g-C ₃ N ₄	[345]
g-C ₃ N ₄ /SnO ₂	Calcination	Degradation of RhB, MO, MB, phenol and CO ₂ reduction/Vis	57.8 wt%	40% in 90 min/phenol, No data for MB, MO and RhB, 27.7 μmol h ⁻¹ /CO ₂	8.8/g-C ₃ N ₄ /RhB, 4.3/g-C ₃ N ₄ /CO ₂	[346]

2.5.2. Ternary nanocomposites

Ternary nanocomposites based on g-C₃N₄ have gained popularity in recent years due to the possibility of exploiting the combined multiple properties from the three components resulting to improved photocatalytic performances over g-C₃N₄ and the corresponding binary heterostructure. Depending on the components of the ternary heterostructure, we have grouped these nanocomposites into four categories: g-C₃N₄/MO/X, g-C₃N₄/MO/M, g-C₃N₄/MO/CNM and g-C₃N₄/MO1/MO2 heterostructures where MO is a semiconductor, X is a non-metal, M is a metal, CNM is a carbon nanomaterial and MO1 and MO2 are two different semiconductors.

2.5.2.1. G-C₃N₄/MO/X ternary heterostructures. In this category, the heterostructures consist of g-C₃N₄, a non-metal and another semiconductor to complete the ternary nanocomposite. Wu et al. reported improved MB visible light photocatalytic degradation over g-C₃N₄/C-TiO₂ prepared by a simple heating method. At the optimum g-C₃N₄ loading (4.1 wt%), the nanocomposite displayed the highest activity which was 4 times higher than the activity of C-TiO₂ [347]. The synergistic effect of C-TiO₂ and incorporation of g-C₃N₄ towards improved visible light response, efficient charge separation and enhanced photocatalyst-dye interaction was responsible for the higher photocatalytic activity of g-C₃N₄/C-TiO₂ compared to g-C₃N₄ and C-TiO₂ [347]. Successful hybridisation of g-C₃N₄ nanosheets with nitrogen doped titania nanofibers (N-TiO₂ NF) using an electrospinning technique coupled with a modified heat-

etching strategy. The hybrid material (denoted as GCN/NT NF) showed significantly improved photoactivity towards RhB degradation and H₂ evolution under visible light illumination [348]. Complete degradation of RhB was observed after 120 min of irradiation using the sample containing 0.1 g g-C₃N₄ (GCN/NT-0.1) which showed the highest activity. Moreover, the optimised hybrid nanostructure displayed activity that was 7.3 and 3.6 times higher than the performance of TiO₂ NFs and g-C₃N₄, respectively [348]. Wang et al. studied the photocatalytic behaviour of g-C₃N₄/N-TiO₂ ternary nanostructures prepared using a microwave assisted method for the decomposition of MB and RhB under visible light exposure. It was observed that the ternary nanostructures showed the highest activity and at an optimum N-TiO₂ loading of 40%, the optimised sample completely degraded both MB and RhB in 60 min [349]. However, total organic carbon (TOC) analysis revealed very low removal, indicating that the dyes were not completely mineralised but partially broken down into smaller, colourless organics, hence the disappearance of the colour [349]. In another work, enhanced visible light photocatalytic degradation of RhB was observed over sheet-like g-C₃N₄/N-TiO₂ heterostructures with excellent stability [350]. The sample containing 78% g-C₃N₄ and 22% N-TiO₂ showed the highest activity which was 19 and 5.3 times higher than that of N-TiO₂ and g-C₃N₄, respectively [350]. Zhou et al. investigated the photocatalytic performance of g-C₃N₄/N-TiO₂ towards CO₂ reduction to CO under visible light illumination [351]. The ternary nanostructure showed good selectivity

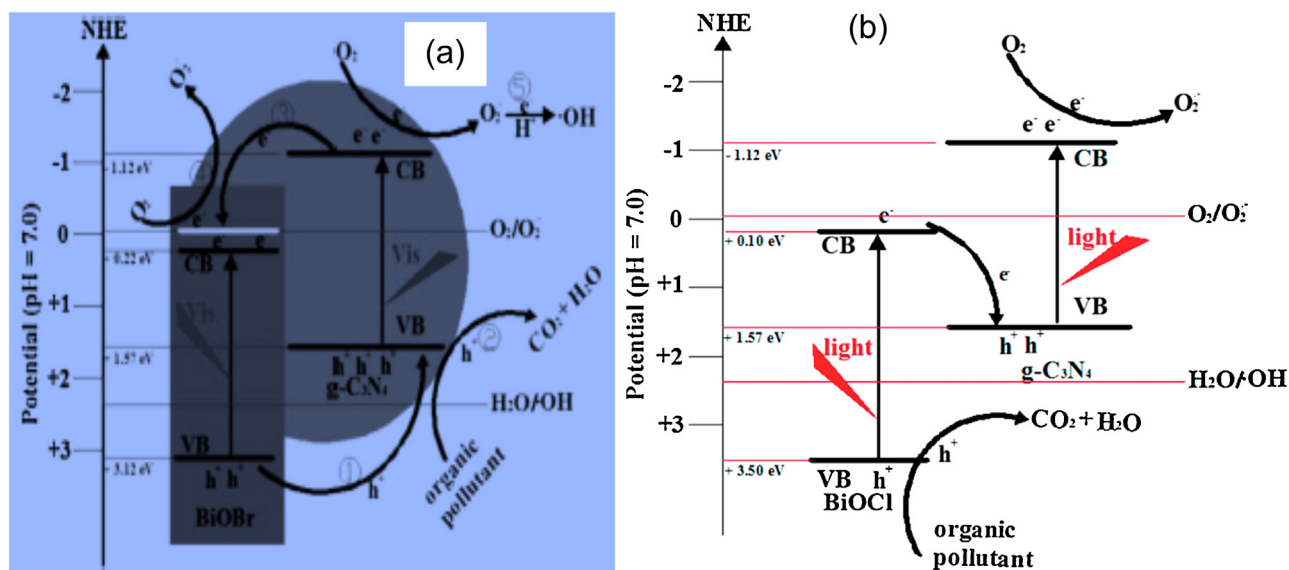


Fig. 19. Charge transfer mechanism (a) under visible light and (b) UV light for g-C₃N₄/BiOBr and g-C₃N₄/BiOCl, respectively. (a) Reproduced with permission from Ref. [276], Copyright 2013, Elsevier. (b) Reproduced with permission from Ref. [270], Copyright 2014, RSC.

Table 5
Summary of the photocatalytic properties other g-C₃N₄/MO/X ternary nanocomposites.

Material	Preparation method	Application	Optimum g-C ₃ N ₄ loading	Degradation efficiency	Enhancement factor over control	Reference
P-g-C ₃ N ₄ /ZnLn ₂ S ₄	Solvothermal	Degradation of 4-nitroaniline (4-NA)/Vis	80 wt%	99.4% in 90 min	No data	[359]
g-C ₃ N ₄ /C-ZnO	Evaporation-calcination	Degradation of MB/Vis	50.7%	78.6% in 120 min	7.3/g-C ₃ N ₄ , 15.3/ZnO	[352]
g-C ₃ N ₄ /N-ZnO	Ultrasonic dispersion	Degradation of RhB/Vis	5 wt%	No data	40/ZnO, 5/g-C ₃ N ₄	[360]
g-C ₃ N ₄ /S-TiO ₂	Planetary milling	Degradation of acetaldehyde/Vis	33.3 wt%	No data	4/S-TiO ₂	[353]
g-C ₃ N ₄ /N-Bi ₂ O ₃	Ultrasonic dispersion	Degradation of RhB/Vis	66.7 wt%	94.4% in 15 min	4.6/g-C ₃ N ₄ , 8.2/Bi ₂ O ₃	[354]
g-C ₃ N ₄ -P/CeO ₂	Mixing-calcination	Degradation of MO/Vis	86.2 wt%	74% in 120 min	7.4/CeO ₂ , 4.9/g-C ₃ N ₄	[355]
g-C ₃ N ₄ /F-TiO ₂	Hydrothermal	Degradation of MB/410 nm LED light	30 wt%	89% in 60 min	4.5/F-TiO ₂ , 13.9/P25	[356]
g-C ₃ N ₄ /N-SrTiO ₃	Thermal exfoliation	Degradation of RhB and 4-chlorophenol (4-CP)/Vis	85 wt%	No data	5/g-C ₃ N ₄	[357]

towards reduction of CO₂ to CO and under optimised conditions the highest amount of CO produced was 14.73 μ mol after 12 h of visible light irradiation. This was 4 times higher than the conversion of P25 under the sample experimental conditions [351]. Table 5 highlights other interesting ternary nanocomposites that have been developed in recent years for environmental pollution remediation. Ternary nanocomposites such as g-C₃N₄/C-ZnO [352], g-C₃N₄/S-TiO₂ [353], g-C₃N₄/N-Bi₂O₃ [354], g-C₃N₄-P/CeO₂ [355], g-C₃N₄/F-TiO₂ [356] and g-C₃N₄/N-SrTiO₃ [357] have shown improved photocatalytic properties compared to their components, individually.

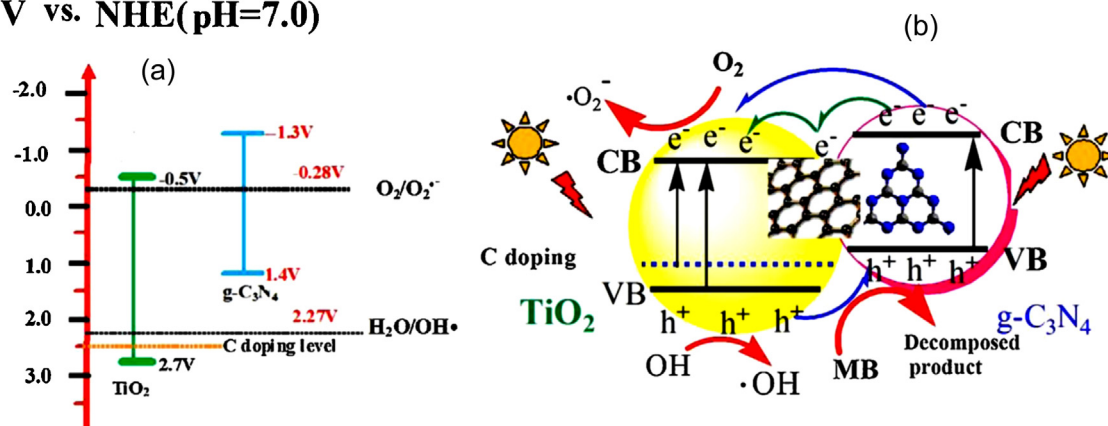
It is well-documented that doping TiO₂ with non-metals causes a red-shift in its absorption edge and improves visible light photocatalytic properties. In the ternary nanocomposites, doping TiO₂ with non-metals such as S, N, C, F, etc. resulted the modification of its band gap due to formation of sub-band gap/impurity states within the TiO₂ band gap [347,350,353,356,358]. These sub-band gap states allows excitation of electrons by visible light from these states into the conduction band of TiO₂. Meanwhile electrons are also excited on g-C₃N₄ and promoted to its conduction band. Fig. 20a shows the diagram of g-C₃N₄/C-TiO₂ and it can be seen that the band potentials of g-C₃N₄ are −1.3 eV (conduction band, CB) and +1.4 eV (valence band, VB) while those of C-TiO₂ are −0.5 eV (CB) and +2.7 eV (VB) [347]. this indicates that the band potentials are well-matched for charge transfer to take place. Consequently, electrons in the conduction band of g-C₃N₄ transfer to the conduction band of TiO₂ where superoxide radicals are formed upon reaction with adsorbed oxygen. The holes migrate to the valence band of g-C₃N₄ and directly oxidise the organic pollutants. Therefore, the holes and superoxide radicals are the main active species responsible for pollutant degradation in these heterostructures [348,350,351]. The ternary nanostructure benefit from increased utilisation of visible light and efficient charge separation since the electrons accumulate on TiO₂ while the holes are located in g-C₃N₄ as depicted in Fig. 20b [347].

2.5.2.2. G-C₃N₄/MO/M ternary heterostructures. This is the category of ternary nanostructures whereby g-C₃N₄ is coupled with another semiconductor and a metallic species as the third component of the nanocomposite. Novel plasmonic ternary nanocomposites are popular in this category and have recently emerged as attractive materials for visible light photocatalytic applications due to their impressive visible light absorption and charge separation

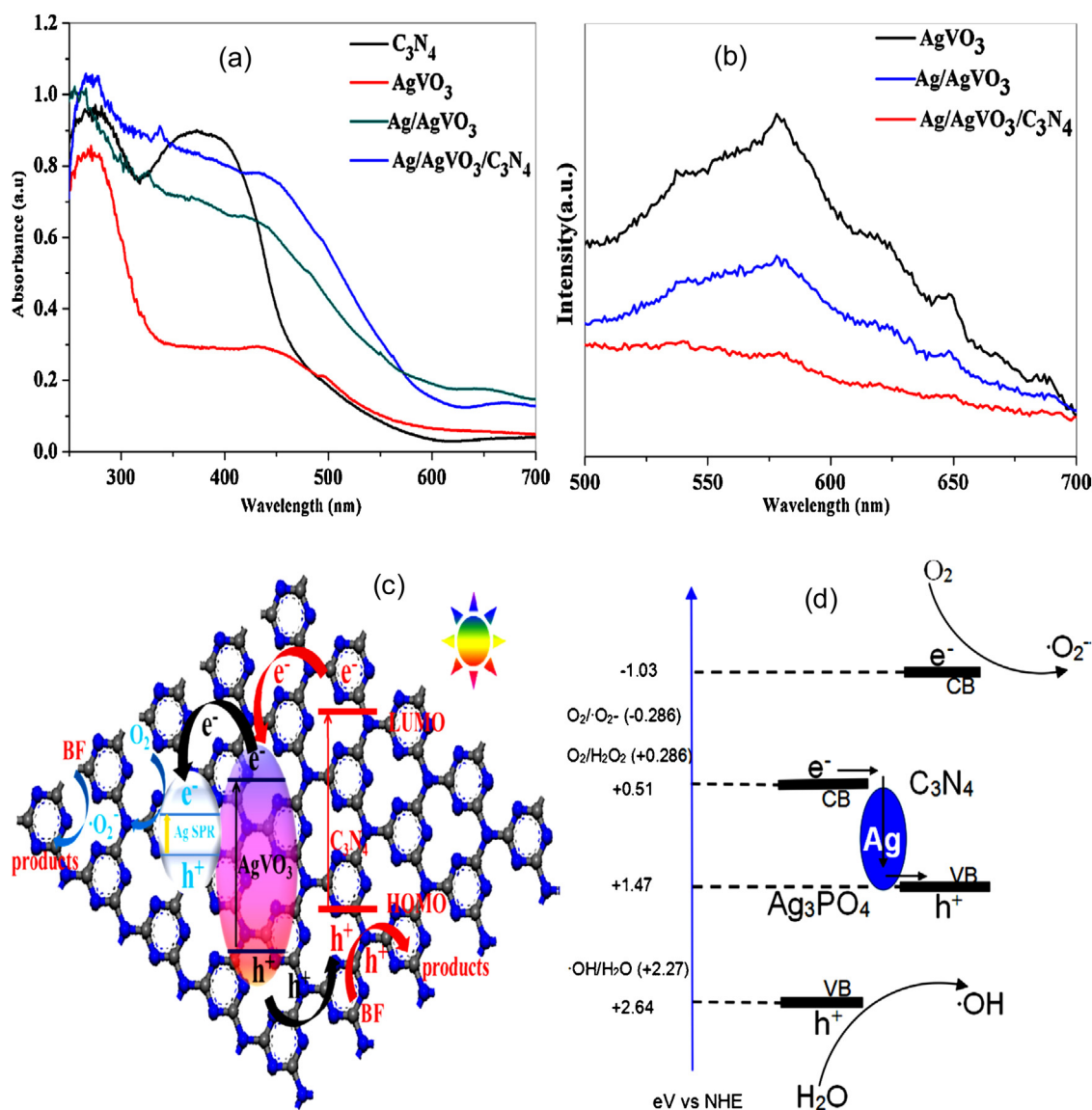
efficiency. Zhao et al. prepared Ag/AgVO₃/g-C₃N₄ nanocomposite (denoted as Ag/AgVO₃/C₃N₄) via a hydrothermal approach and investigated its photocatalytic behaviour towards degradation of basic fuchsin (BF) under visible light illumination. Improved visible light response was revealed by UV–vis diffuse reflectance measurements (Fig. 21a) and PL analysis showed a very low PL peak (Fig. 21b) for the ternary nanocomposite which indicates efficient charge carrier separation [361]. The ternary heterostructure exhibited good photocatalytic degradation efficiency reaching 99.3% BF removal in just 70 min of visible light exposure and its photocatalytic activity was 12.5 and 3.1 times higher than that of g-C₃N₄ and Ag/AgVO₃, respectively. Also, the nanocomposite photocatalyst showed sufficiently high stability without any significant loss of activity after 5 cycles (92.5% BF removal after 5 cycles) [361]. Yang et al. reported improved photocatalytic performance of Ag/AgBr/g-C₃N₄ with an optimum Ag/AgBr loading of 50 wt%, towards visible light photocatalytic degradation of both MO and RhB [362]. A decrease in activity was observed with increasing Ag/AgBr concentration beyond 50 wt% which could be related to lack of contact between the excess Ag/AgBr and g-C₃N₄, leading to accelerated photocorrosion. Over 93% degradation was recorded for both dyes in 10 min of visible light illumination [362]. Wang et al. observed enhanced visible light photocatalytic degradation of MO over Ag/Ag₃PO₄/g-C₃N₄ and the photocatalyst exhibited sufficiently high stability and could be recycled 3 times without any obvious loss of its photocatalytic activity [363]. Its photocatalytic performance was 1.9 and 22.5 times higher than the photocatalytic activity of Ag₃PO₄ and g-C₃N₄, respectively [363].

In the Ag/AgVO₃/g-C₃N₄, Ag/AgBr/g-C₃N₄ and Ag/Ag₃PO₄ heterostructures, both semiconductors absorb in the visible light region and holes are formed in their valence bands while the electrons occupy the conduction bands, upon visible light excitation. Likewise, the Ag nanoparticles also contribute to visible light absorption due to the SPR effect. A typical heterojunction type of charge transfer mechanism (Fig. 21c) was proposed for the Ag/AgVO₃/g-C₃N₄, whereby the electrons in the conduction band of g-C₃N₄ transfer to the conduction band of AgVO₃ where they are subsequently trapped by the Ag nanoparticles [361]. On the Ag nanoparticles, the electrons are trapped by adsorbed oxygen to form the superoxide radicals which then attack the organic pollutants on contact. Meanwhile, the holes in the valence band of AgVO₃ transfer to the valence band of g-C₃N₄ where they directly oxidise the pollutant molecules [361]. It is worth noting that the

V vs. NHE(pH=7.0)

Fig. 20. (a) Band diagram and (b) charge transfer mechanism in $\text{g-C}_3\text{N}_4/\text{C-TiO}_2$.

Reproduced with permission from Ref. [347]. Copyright 2016, Elsevier.

Fig. 21. (a) UV-vis diffuse reflectance spectra, (b) PL spectra, (c) heterojunction type of charge transfer in $\text{Ag/AgVO}_3/\text{g-C}_3\text{N}_4$. (d) Z-scheme charge transfer mechanism in $\text{Ag/Ag}_3\text{PO}_4/\text{g-C}_3\text{N}_4$.

(a–c) Reproduced with permission from Ref. [361]. Copyright 2015, Elsevier. (d) Reproduced with permission from Ref. [363]. Copyright 2014, Elsevier.

Table 6Summary of the photocatalytic properties of various g-C₃N₄/M/MO ternary nanostructures.

Material	Preparation method	Application	Optimum g-C ₃ N ₄ loading	Degradation efficiency	Enhancement factor over control	Reference
g-C ₃ N ₄ /Ag/Ag ₂ O	Hydrothermal	RhB/Vis	No data	No data	3.0/g-C ₃ N ₄ , 7.0/P25	[369]
g-C ₃ N ₄ /Cr-SrTiO ₃	Mixing-calcination	Degradation of MO/Vis	60%	100% in 240 min	No data	[378]
g-C ₃ N ₄ /Ag/Sr _{0.25} H _{1.5} Ta ₂ O ₆ ·H ₂ O	Ultrasonication/precipitation-deposition	Cr(IV) reduction and MO degradation/Vis	50%	89.5% in 50 min/Cr(IV), 96.5% in 50 min/MO	4.7/g-C ₃ N ₄ /Cr(IV), 14.2/g-C ₃ N ₄ /MO	[377]
g-C ₃ N ₄ /Ag-BiOF	Solvothermal	Degradation of MB/Vis	No data	78% in 6 h	No data	[370]
g-C ₃ N ₄ /Ag/Fe ₃ O ₄	Photodeposition	Degradation of tetracycline/Vis	No data	88% in 90 mins	1.55/Ag/g-C ₃ N ₄	[372]
Pt-g-C ₃ N ₄ /KNbO ₃	Ultrasonic dispersion-heat treatment	CO ₂ reduction/Vis	75 wt%	0.25 μmol h ⁻¹	4.2/Pt-g-C ₃ N ₄	[373]
g-C ₃ N ₄ /Ag-TiO ₂	Photodeposition-ultrasonication	Degradation of RhB/Vis	50%	No data	6.3/TiO ₂ , 1.63/g-C ₃ N ₄	[374]
g-C ₃ N ₄ /Ag-ZnO	Hydrothermal	Degradation of MB and destruction of gram negative <i>E. coli</i> /Vis	No data	No data	No data	[375]
g-C ₃ N ₄ /Ti ³⁺ -TiO ₂	Hydrothermal-sonication	Degradation of RhB and Cr(IV) reduction/Vis	6 wt%	97% in 120 min/RhB, No data for Cr(IV)	No data	[379]
g-C ₃ N ₄ /Ag/MoS ₂	<i>In situ</i> thermal condensation	Degradation of RhB/Vis	No data	98.6% in 60 min	3.83/g-C ₃ N ₄	[380]

bands. Subsequently, the electrons in the conduction band of g-C₃N₄ transfer to the less negative conduction band of ZnO (−0.5 eV) and the electrons further transfer to GO which is more electropositive (−0.08 eV). These electrons are trapped by adsorbed oxygen to form the superoxide radicals while the ZnO valence band holes oxidise water to form the hydroxyl radicals. Accordingly, the holes on g-C₃N₄ oxidise the dye molecules directly to form the degradation products [381]. Under visible light illumination, only g-C₃N₄ is excited, so there is no generation of hydroxyl radicals in the valence band of ZnO, the superoxide radicals and holes are the only active species.

Wang et al. reported on the visible light photocatalytic properties of Ag₃PO₄ nanoparticles wrapped with GO sheets supported on g-C₃N₄ sheets (GO/Ag₃PO₄/g-C₃N₄) towards degradation of RhB [382]. Significantly higher photocatalytic activity was observed from the ternary nanostructure compared to single component and binary nanocomposite photocatalyst. This was ascribed to the combined contribution of the three components resulting to increased visible light utilisation, good adsorption properties and improved charge separation and transfer. In terms of degradation kinetics, the activity of GO/Ag₃PO₄/g-C₃N₄ was 162 and 8 times higher than the activity of g-C₃N₄ and Ag₃PO₄, respectively [382]. Pawar et al. studied the photocatalytic properties of g-C₃N₄/CdS/RGO ternary nanocomposite for the degradation of RhB and Congo Red under both UV and visible light illumination. The hybrid nanostructure displayed superior photocatalytic activity for both dyes over g-C₃N₄, g-C₃N₄/CdS and g-C₃N₄/RGO under both light conditions [383]. In another work, a hybrid nanostructure consisting of g-C₃N₄, ultrathin GO and MoS₂ nanosheets (g-C₃N₄/GO/MoS₂) was fabricated using a sonochemical route and explored for the decomposition of RhB under visible light irradiation [384]. It was observed that the ternary nanostructure was significantly more photocatalytic active (89.5% RhB removal in 2.5 h) compared to g-C₃N₄, g-C₃N₄/GO and g-C₃N₄/MoS₂ [384].

In GO/Ag₃PO₄/g-C₃N₄, g-C₃N₄/CdS/RGO and g-C₃N₄/GO/MoS₂ ternary nanostructures, all three components of each material absorb visible light resulting in the excitation of electrons and formation of holes. Subsequently, the electrons in the conduction band of g-C₃N₄ transfer to the conduction band of Ag₃PO₄/CdS/MoS₂ and

in the case of Ag₃PO₄ and CdS, these electrons transfer to GO/RGO where they are captured by adsorbed molecular oxygen to form the radical species [382,383]. On the contrary, for MoS₂, the electrons in its conduction band could react with oxygen to form the radical species [384]. Moreover, the matching band potentials of GO and MoS₂ allows electrons to be transferred from GO to the conduction band of MoS₂. Similarly, electrons are transferred from the conduction band of g-C₃N₄ to GO where they can be captured by oxygen to form the superoxide radicals [384]. Meanwhile, in all three ternary nanocomposites, the holes transfer to g-C₃N₄ and directly oxidise the dye molecules [382–384]. It is generally observed that in these ternary nanostructures the electrons accumulate on GO/RGO and MoS₂/Ag₃PO₄/CdS while the holes occupy the valence band of g-C₃N₄. Recently, Ma et al. proposed a Z-scheme electron transfer mechanism in g-C₃N₄/RGO/Bi₂WO₆ where by the electrons in the conduction band of Bi₂WO₆ transfer to RGO and subsequently to the valence band of g-C₃N₄ to recombine with the holes. The holes are preserved in the valence band of Bi₂WO₆ while the electrons are located in the conduction band of g-C₃N₄ [385]. This arrangement ensures efficient separation of the photogenerated charge carriers. The presence of GO/RGO ensures improved electron scavenging and transportation in the nanocomposite which fast-track formation of the radical species responsible for dye degradation. Additionally, pollutant-photocatalyst interaction is improved upon incorporation of the carbon nanomaterials which is essential for the photodegradation process.

The growing interest in g-C₃N₄ based ternary nanostructures containing carbon nanomaterials has recently seen the emergence of interesting nanostructures such as g-C₃N₄/CNTs/Au [64], Ag/g-C₃N₄/RGO [386], g-C₃N₄-Fe(III)/graphene [387], g-C₃N₄/RGO/α-S₈ [388] and g-C₃N₄/NRGO/MoS₂ [389] which have been investigated for degradation of various pollutants under visible light exposure. Grafting Fe(III) on g-C₃N₄ prior to incorporation of graphene increased the photocatalytic activity of the ternary nanostructure towards MO decomposition owing to efficient interfacial charge transfer and separation of the photogenerated charge carriers [387]. The Fe(III) species and graphene acted as electron sinks and facilitated the formation of the superoxide radicals via reaction of the captured electrons and adsorbed oxygen [387]. In the case

of Ag/g-C₃N₄/RGO and Au/g-C₃N₄/CNTs, upon visible light irradiation, electrons are excited to form the charge carriers. Accordingly, the electrons in the conduction band of g-C₃N₄ are transferred to RGO/CNT and are subsequently trapped by Ag/Au where they react with oxygen to form the oxidising species [64,386]. Meanwhile, the Ag/Au nanoparticles are also excited by visible light and the plasmon resonance generated electrons are trapped by oxygen to form the superoxide radicals. The holes left in Ag/Au are filled with electrons from g-C₃N₄ and RGO/CNTs while the valence band holes in g-C₃N₄ facilitate degradation of the organic pollutants [64,386].

2.5.2.4. G-C₃N₄/MO1/MO2 ternary nanocomposites. Under this category, g-C₃N₄ is coupled with two other semiconductors (MO1 and MO2) to form the ternary nanostructure. These nanocomposites benefit from the collaborative contribution of the coupled semiconductors towards increased generation of the oxidising species, efficient charge separation and transfer via the heterojunctions formed and improved exploitation of visible light [390,391]. Munoz-Batista et al. fabricated g-C₃N₄/CeO₂/TiO₂ nanocomposites with varying g-C₃N₄ concentrations using a combination of microemulsion and impregnation routes and probed the photocatalytic degradation of toluene under UV and sunlight type of radiation [391]. The sample containing 1 wt% g-C₃N₄ showed the highest activity compared to the single and binary nanostructures both under both illumination conditions [391]. A phase transformation method was employed to tailor a Ag₂O/Ag₂CO₃/g-C₃N₄ heterostructure which then studied for the UV and visible light photocatalytic degradation of phenol [390]. Phenol degradation using Ag₂O/Ag₂CO₃/g-C₃N₄ was almost complete after 30 min of UV light exposure and in terms of kinetics, the activity of the ternary nanostructure was 11.0 and 19.1 times higher than the activity of g-C₃N₄ under UV and visible light irradiation, respectively [390]. Akhundi and Habibi-Yangjeh reported photocatalytic activity towards MB over g-C₃N₄/ZnO/AgCl under visible light irradiation [392]. The photocatalytic activity of the sample containing 60% g-C₃N₄ was found to be the highest and was 9.5, 7.5 and 6 times higher than the activity of g-C₃N₄, g-C₃N₄/ZnO and g-C₃N₄/AgCl, respectively. Moreover, the ternary nanostructure showed good stability over 5 cycles of progressive use, showing insignificant loss of photoactivity [392].

A heterojunction type of charge transfer (Fig. 23a) mechanism was highlighted as the most plausible charge transfer route in g-C₃N₄/ZnO/AgCl nanostructures. The wide band gaps of ZnO and AgCl (3.2 eV) means that only g-C₃N₄ is excited in the visible region forming the charge carriers. Subsequently, the electrons in the conduction of g-C₃N₄ transfer to both ZnO and AgCl while some are trapped by oxygen to form the radical species [392]. Electrons in the conduction band of ZnO (-0.34 eV) is not sufficiently negative to reduce oxygen while the conduction band electron in AgCl (-0.06 eV) cannot reduce oxygen at all due to less negative potential. However, both conduction band electrons can be captured by oxygen to form H₂O₂ which can capture an electron to form the hydroxyl radical. Accordingly, the valence band holes in g-C₃N₄ will directly oxidise the dye molecules to form the degradation products [392]. The electron and holes are kept at different parts of the ternary structure, ensuring efficient separation. Meanwhile the multiple semiconductors provides adequate sites where oxidising species can be formed.

Owing to the challenges associated with separation of the photocatalyst particles from the treated solution, several magnetic ternary nanocomposites such as g-C₃N₄/Fe₃O₄/BiOI [394], g-C₃N₄/AgBr/Fe₃O₄ [393], g-C₃N₄/Fe₃O₄/AgCl [395], g-C₃N₄/Fe₃O₄/AgVO₃ [396] and g-C₃N₄/MnFe₂O₄/TiO₂ [397] have recently emerged as attractive materials due to their magnetic properties. Mousavi and Habibi-Yangjeh reported remarkable photocatalytic activity of g-C₃N₄/Fe₃O₄/BiOI towards RhB, MB and

MO and its activity was 10, 22 and 21 times higher than that of g-C₃N₄ for RhB, MB and MO, respectively. Most importantly, the ternary nanostructure was magnetically separable and did not show any noticeable loss of activity and magnetism after 5 cycles of successive use [394]. A similar pattern of results has been reported for g-C₃N₄/AgBr/Fe₃O₄ [393], g-C₃N₄/Fe₃O₄/AgCl [395], g-C₃N₄/Fe₃O₄/AgVO₃ [396], g-C₃N₄/Fe₃O₄/Ag₂CrO₄ [398] g-C₃N₄/MnFe₂O₄/TiO₂ [397]. Formation of these ternary nanostructures has been found not only to enhance visible light utilisation and charge separation but also allows for easy separation and recycling of the photocatalyst using an external magnetic field (Fig. 23b, inset) [393–397]. Notably, in all the magnetic ternary nanostructures, the saturation magnetization (Fig. 23b) of the magnetite nanoparticles is significantly reduced upon formation of the ternary nanostructure which could be ascribed to the interaction of the magnetite nanoparticles with non-magnetic components of the heterostructures. However, all the nanocomposites could still retain enough magnetism to be efficiently separated from the solution using an external magnetic field (Fig. 23b, inset) [393–397].

In terms of charge transfer in these ternary nanostructures, it can be generalised that upon visible light absorption and excitation, the electrons transfer away from the conduction band of g-C₃N₄ while the holes transfer to the valence band of g-C₃N₄. The direction of transfer of electrons and holes is governed by the band potential structures of the materials involved. Notably, the magnetite and manganese ferrite nanoparticles have no significant photocatalytic role but their main function comes in the separation of the photocatalyst from solution [393–397]. The ability to efficiently separate the photocatalyst nanoparticles from solution could alleviate the fears of secondary pollution by the photocatalyst particles.

3. Summary remarks and perspective

Photocatalysis holds the key for the future in environmental decontamination and renewable energy generation from water splitting. A brief account of the fundamental principles of photocatalysis and the key steps involved in the photocatalytic degradation of organics had been presented in this review. Tremendous interest in graphitic carbon nitride as a photocatalyst has seen it emerging as fascinating materials in various scientific fields such as environmental pollution abatement, hydrogen evolution from water splitting, sensors, energy storage, etc. These applications exploit some of the fascinating properties of g-C₃N₄ which include visible light response, good oxidation power, environmental friendliness, good chemical and thermal stability, metal-free nature, easy fabrication from readily available precursors and its polymeric structure allows for easy modifications to alter its properties. A comprehensive discussion on the most recent developments towards engineering g-C₃N₄ heterostructures with improved photocatalytic properties towards organic and inorganic pollution remediation has been presented in this review. Such nanostructures include metal and non-metal doped g-C₃N₄, g-C₃N₄/carbon nanomaterials heterojunctions, binary and ternary nanocomposites. The charge transfer mechanisms involved in the various heterostructures have been discussed in detail. Improved visible light photocatalytic performance has been observed upon formation of the various heterostructures and this has been credited to improved specific surface area, efficient charge separation and transfer, improved generation of the oxidising species and efficient visible light harvesting.

Despite the wealth of graphitic carbon nitride based materials that have been fabricated thus far, there is still no single material that has been universally accepted as capable of functioning well across various photocatalytic applications. At the very least, no material has been shown to be versatile in degrading a wide

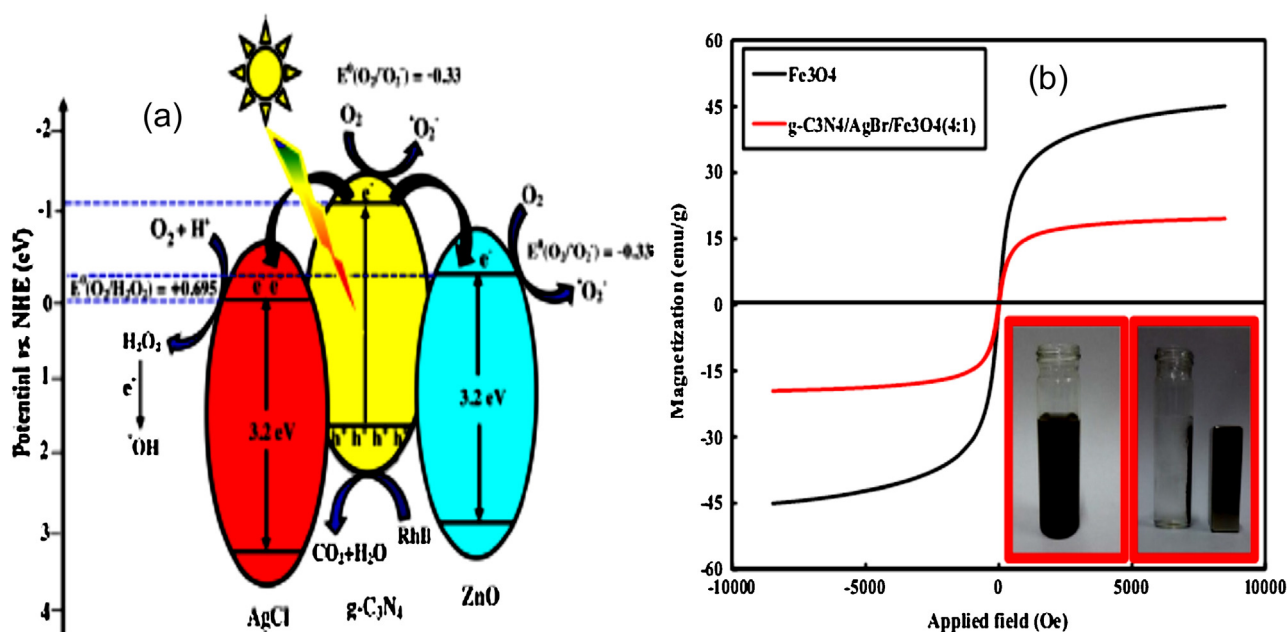


Fig. 23. (a) Heterojunction charge transfer mechanism in g-C₃N₄/ZnO/AgCl and (b) magnetization curves of properties of g-C₃N₄/AgBr/Fe₃O₄ and Fe₃O₄ and inset showing separation of the photocatalyst from solution using a magnet.

(a) Reproduced with permission from Ref. [392], Copyright 2015, Elsevier. (b) Reproduced with permission from Ref. [393], Copyright 2015, Elsevier.

spectrum of pollutants. For example, there is no single material capable of NO oxidation, CO₂ reduction, dye degradation, Cr(IV) reduction, pesticide/herbicide degradation, microbial inactivation and degradation of pharmaceuticals under visible/sunlight conditions. This means that the challenge of developing graphitic carbon nitride heterostructures for practical applications still lies ahead. The lack of a systematic protocol for evaluating the photocatalytic properties of the prepared materials contributes to the vast differences reported in the literature. Every researcher claims to have prepared a material that shows photocatalytic superiority over what is already out there. However, such claims are always misleading to some extent because different synthesis procedures and starting materials are used to prepare the materials and when it comes to evaluating the photocatalytic activity, different reactors and light sources are used. This is just to mention a few of those factors that can cause different sets of results from the same material. Therefore, development of a universal protocol for evaluating the photocatalytic properties could possibly paint a clearer picture on where we are in terms of photocatalysis for large scale applications.

This review has shown that there is a gradual shift in research exploration from pure g-C₃N₄ to doped g-C₃N₄, binary and ternary nanostructures and there is a general improvement in photocatalytic activity upon metal deposition, metal and non-metal doping, and formation of binary and complex heterostructures. However, as the photocatalyst become complex, so is the charge transfer mechanism involved and a good understanding of the charge transfer process is crucial in designing functional photocatalysts. For example, in a ternary nanostructure, more than one heterojunction is formed and the influence and effectiveness of each towards the overall photocatalytic process needs to be clearly understood. Furthermore, the loadings of each component of the ternary or binary nanocomposite needs to be carefully controlled in order to obtain optimum performance. Therefore, it is necessary to employ extensive theoretical tools to better understand how the various components of the complex nanostructure interact and get an insight regarding the efficiency of the heterojunctions formed in terms of charge transfer. Moreover, theoretical studies can help predict the optimum loading of each component of the heterostruc-

ture. This will ensure that while sufficient modifications in the band structure are achieved, high photocatalytic activity is retained.

A clear understanding of the band structure of the heterostructure is key in designing a photocatalyst for a particular purpose. However, for the most part, researchers have been emphasising on the importance of the band gap when preparing photocatalyst ignoring the utmost importance of the band position/potential. The band gap gives information about the photoresponse of the materials while not giving any information about the redox power of the conduction and valence bands of the material. Electron transfer and formation of the oxidising species responsible for decomposition of the pollutants are governed by the band potentials. Theoretical calculations can help predict the effect of coupling certain materials with graphitic carbon nitride or doping it with metals or non-metals on the band structure.

Lastly, when it comes to minimising secondary pollution by the photocatalyst nanoparticles, the fabrication of magnetic heterostructures seems to be providing an attractive solution. However, work still needs to be done in developing synthetic procedures that will ensure homogeneous distribution of the magnetic nanoparticles within the nanocomposite and ensure strong contact with the other materials. This is to minimise leaching out of the magnetic nanoparticles which will not only cause secondary pollution but will also compromise the recyclability of the photocatalyst.

Acknowledgement

Financial support from the College of Science, Engineering and Technology (CSET) of the University of South Africa is highly appreciated.

References

- [1] N. Serpone, A.V. Emeline, J. Phys. Chem. Lett. 3 (2012) 673–677.
- [2] M.A. Fox, M.T. Dulay, Chem. Rev. 93 (1993) 341–357.
- [3] K. Soutsas, V. Karayannis, I. Poullos, A. Riga, K. Ntamegliotis, X. Spiliotis, et al., Desalination 250 (2010) 345–350.

- [4] P.A. Pekakis, N.P. Xekoukoulotakis, D. Mantzavinos, *Water Res.* 40 (2006) 1276–1286.
- [5] I.K. Konstantinou, T.A. Albanis, *Appl. Catal. B: Environ.* 49 (2004) 1–14.
- [6] N. Mohammad, M. Arami, *J. Photochem. Photobiol. B: Biol.* 94 (2009) 20–24.
- [7] R. Molinari, M. Borgese, E. Drioli, L. Palmisano, M. Schiavello, *Catal. Today* 75 (2002) 77–85.
- [8] P. Kariyajanavar, N. Jogtappa, Y.A. Nayaka, *J. Hazard. Mater.* 190 (2011) 952–961.
- [9] K. Vinodgopal, I. Bedja, S. Hotchandani, P.V. Kamat, *Langmuir* 10 (1994) 1767–1771.
- [10] A. Sobczynski, A. Dobosz, *Pol. J. Environ. Stud.* 10 (2001) 195–205.
- [11] D. Bahnemann, *Sol. Energy* 77 (2004) 445–459.
- [12] A. Mills, R.H. Davies, D. Worsley, *Chem. Soc. Rev.* 22 (1993) 417.
- [13] X. Zhang, Y.L. Chen, R.-S. Liu, D.P. Tsai, *Rep. Prog. Phys.* 76 (2013) 046401.
- [14] A. Di Paola, E. Garcia-Lopez, G. Marci, L. Palmisano, *J. Hazard. Mater.* 211–212 (2012) 3–29.
- [15] D. Xu, X. Li, J. Liu, L. Huang, *J. Rare Earths* 31 (2013) 1085–1091.
- [16] W.Z. Tang, H. An, *Chemosphere* 31 (1995) 4171–4183.
- [17] D. Ravelli, D. Dondi, A. Albini, *Chem. Soc. Rev.* 38 (2011) 1999–2011.
- [18] M.D. Hernandez-Alonso, F. Fresno, S. Suarez, J.M. Coronado, *Energy Environ. Sci.* 2 (2009) 1231–1257.
- [19] L. Rizzo, J. Koch, V. Belgiorno, M.A. Anderson, *Desalination* 211 (2007) 1–9.
- [20] G. Rothenberger, J. Moser, M. Gratzel, N. Serpone, D.K. Sharma, *J. Am. Chem. Soc.* 107 (1985) 8054–8059.
- [21] A. Primo, A. Corma, H. Garcá, *Phys. Chem. Chem. Phys.* 13 (2011) 886–910.
- [22] A.L. Linsebigler, G. Lu, J.T. Yates, *Chem. Rev.* 95 (1995) 735–758.
- [23] W.Y. Teoh, J.A. Scott, R. Amal, *J. Phys. Chem. Lett.* 3 (2012) 629–639.
- [24] L.G. Devi, R. Kavitha, *Appl. Catal. B: Environ.* 140–141 (2013) 559–587.
- [25] K. Pirkanniemi, M. Sillanpää, *Chemosphere* 48 (2002) 1047–1060.
- [26] C.-H. Wu, C.-L. Chang, C.-Y. Kuo, *Dyes Pigm.* 76 (2008) 187–194.
- [27] T.K. Tseng, Y.S. Lin, Y.J. Chen, H. Chul, *Int. J. Mol. Sci.* 11 (2010) 2336–2361.
- [28] M.A. Henderson, *Surf. Sci. Rep.* 66 (2011) 185–297.
- [29] H.Y. Chen, O. Zahraa, M. Bouchy, F. Thomas, J.Y. Bottero, *J. Photochem. Photobiol. A: Chem.* 85 (1995) 179–186.
- [30] Y. Tseng, C. Kuo, C. Huang, Y.-Y. Li, P.-W. Chou, C.-L. Cheng, et al., *Nanotechnology* 17 (2006) 2490–2497.
- [31] H. Al-Ekabi, N. Serpone, *J. Phys. Chem.* 92 (1988) 5726–5731.
- [32] D. Chen, A.K. Ray, *Chem. Eng. Sci.* 56 (2001) 1561–1570.
- [33] A. Mills, S. Le Hunte, *J. Photochem. Photobiol. A: Chem.* 108 (1997) 1–35.
- [34] A. Nezamzadeh-Ejhi, M. Khorsandi, *Desalination* 262 (2010) 79–85.
- [35] M.R. Hoffmann, S.T. Martin, W. Choi, D.W. Bahnemann, *Chem. Rev.* 95 (1995) 69–96.
- [36] O. Legrini, E. Oliveros, A. Braun, *Chem. Rev.* 93 (1993) 671–698.
- [37] A. Primo, A. Corma, H. Garcia, *Phys. Chem. Chem. Phys.* 13 (2011) 886–910.
- [38] J. Zhao, T. Wu, K. Wu, K. Oikawa, H. Hidaka, N. Serpone, *Environ. Sci. Technol.* 32 (1998) 2394–2400.
- [39] V. Maurino, C. Minero, E. Pelizzetti, M. Vincenti, *Colloids Surf. A: Physicochem. Eng. Asp.* 151 (1999) 329–338.
- [40] K.T. Ranjit, I. Willner, S.H. Bossmann, A.M. Braun, *Environ. Sci. Technol.* 35 (2001) 1544–1549.
- [41] R. Leary, A. Westwood, *Carbon* 49 (2011) 741–772.
- [42] S. Rehman, R. Ullah, A.M. Butt, N.D. Gohar, *J. Hazard. Mater.* 170 (2009) 560–569.
- [43] Z.M. El-bahy, A.A. Ismail, R.M. Mohamed, *J. Hazard. Mater.* 166 (2009) 138–143.
- [44] I. Willner, Y. Eichen, *J. Am. Chem. Soc.* 111 (1989) 1884–1886.
- [45] A.J. Frank, I. Willner, Z. Goren, Y. Deganit, *J. Am. Chem. Soc.* 109 (1987) 3568–3573.
- [46] I. Willner, Y. Eichen, *J. Am. Chem. Soc.* 109 (1987) 6862–6863.
- [47] J. Herrmann, *Catal. Today* 53 (1999) 115–129.
- [48] M.N. Chong, B. Jin, C.W.K. Chow, C. Saint, *Water Res.* 44 (2010) 2997–3027.
- [49] J. Wirth, R. Neumann, M. Antonietti, P. Saalfrank, *Phys. Chem. Chem. Phys.* 16 (2014) 15917–15926.
- [50] F. Chang, Y. Xie, C. Li, J. Chen, J. Luo, X. Hu, et al., *Appl. Surf. Sci.* 280 (2013) 967–974.
- [51] S. Pany, K.M. Parida, *Phys. Chem. Chem. Phys.* 17 (2015) 8070–8077.
- [52] H. Zhang, Y. Huang, S. Hu, Q. Huang, C. Wei, W. Zhang, et al., *Electrochim. Acta* 176 (2015) 28–35.
- [53] L. Wang, F. Zhao, Q. Han, C. Hu, L. Lv, N. Chen, et al., *Nanoscale* 7 (2015) 9694–9702.
- [54] J. Tian, Q. Liu, A.M. Asiri, X. Sun, Y. He, *Sensor. Actuat. B: Chem.* 216 (2015) 453–460.
- [55] P. Wen, P. Gong, J. Sun, J. Wang, S. Yang, *J. Mater. Chem. A: Chem.* 3 (2015) 13874–13883.
- [56] Q. Chen, Y. Zhao, X. Huang, N. Chen, L. Qu, *J. Mater. Chem. A: Chem.* 3 (2015) 6761–6766.
- [57] M. Anbia, M. Haqshenas, *Int. J. Environ. Sci. Technol.* 12 (2015) 2649–2664.
- [58] R. Hu, X. Wang, S. Dai, D. Shao, T. Hayat, A. Alsaedi, *Chem. Eng. J.* 260 (2015) 469–477.
- [59] Y. Oh, V. Le, U.N. Maiti, J.O. Hwang, W.J. Park, J. Lim, *ACS Nano* 9 (2015) 9148–9157.
- [60] Y. Zhao, R. Tang, R. Huang, *Catal. Lett.* 145 (2015) 1961–1971.
- [61] Q. Yang, W. Wang, Y. Zhao, J. Zhu, Y. Zhu, L. Wang, *RSC Adv.* 5 (2015) 54978–54984.
- [62] J. Liu, Y. Liu, N. Liu, Y. Han, X. Zhang, H. Huang, et al., *Science* 347 (2015) 970–974.
- [63] Q. Liang, Z. Li, X. Yu, Z.-H. Huang, F. Kang, Q.-H. Yang, *Adv. Mater.* 27 (2015) 4634–4639.
- [64] L. Xu, W.-Q. Huang, L.-L. Wang, Z.-A. Tian, W. Hu, Y. Ma, et al., *Chem. Mater.* 27 (2015) 1612–1621.
- [65] R. Pawar, S. Kang, S.-H. Ahn, C. Lee, *RSC Adv.* 5 (2015) 24281–24292.
- [66] I. Papailias, T. Giannakopoulou, N. Todorova, D. Demotikali, T. Vaimakis, C. Trapalis, *Appl. Surf. Sci.* 358 (2015) 278–286.
- [67] M. Lan, G. Fan, L. Yang, F. Li, *RSC Adv.* 5 (2015) 5725–5734.
- [68] G. Li, X. Nie, J. Chen, Q. Jiang, T. An, P.K. Wong, et al., *Water Res.* 86 (2015) 17–24.
- [69] W. Ho, Z. Zhang, M. Xu, X. Zhang, X. Wang, Y. Huang, *Appl. Catal. B: Environ.* 179 (2015) 106–112.
- [70] Y.-C. Lu, J. Chen, A.-J. Wang, N. Bao, J.-J. Feng, W. Wang, et al., *J. Mater. Chem. C* 3 (2015) 73–78.
- [71] L. Zhao, L. Wang, P. Yu, D. Zhao, C. Tian, H. Feng, et al., *Chem. Commun.* 51 (2015) 12399–12402.
- [72] S. Liu, Y. Dong, Z. Wang, H. Huang, Z. Zhao, J. Qiu, *J. Mater. Chem. A* 3 (2015) 19657–19661.
- [73] W.-B. Luo, S.-L. Chou, J.-Z. Wang, Y.-C. Zhai, H.-K. Liu, *Small* 11 (2015) 2817–2824.
- [74] J. Yi, K. Liao, C. Zhang, T. Zhang, F. Li, H. Zhou, *ACS Appl. Mater. Interfaces* 7 (2015) 10823–10827.
- [75] P. Gai, R. Song, C. Zhu, Y. Ji, Y. Chen, J.-R. Zhang, et al., *Chem. Commun.* 51 (2015) 14735–14738.
- [76] J. Yang, H. Zhang, B. Chen, H. Tang, C. Li, Z. Zhang, *RSC Adv.* 5 (2015) 64254–64260.
- [77] R. Chen, J. Zhang, Y. Wang, X. Chen, J.A. Zapien, C. Lee, *Nanoscale* 7 (2015) 17299–17305.
- [78] Y. Wang, R. Ou, H. Wang, T. Xu, J. Membr. Sci. 475 (2015) 281–289.
- [79] J. Liebig, *Ann. Pharm.* 10 (1834) 10.
- [80] A.Y. Liu, M.L. Cohen, *Science* 245 (1989) 841–842.
- [81] C. Niu, Y.Z. Lu, C.M. Lieber, *Science* 261 (1993) 334–337.
- [82] A.V. Semench, L.N. Blinov, *Glass Phys. Chem.* 36 (2010) 199–208.
- [83] M. Mattesini, S.F. Matar, A. Snis, J. Etourneau, *J. Mater. Chem.* 9 (1999) 3151–3158.
- [84] X. Wang, K. Maeda, A. Thomas, K. Takanabe, G. Xin, J.M. Carlsson, et al., *Nat. Mater.* 8 (2009) 76–80.
- [85] F.H.A. El-kader, M.A. Moharram, M.G. Khafagia, F. Mamdouh, *Spectrochim. Acta A: Mol. Biomol. Spectrosc.* 97 (2012) 1115–1119.
- [86] A. Thomas, A. Fischer, F. Goettmann, M. Antonietti, J.-O. Muller, R. Schlögl, et al., *J. Mater. Chem.* 18 (2008) 4893.
- [87] K. Schwinghammer, M.B. Mesch, V. Duppel, C. Ziegler, J. Senker, B.V. Lotsch, *J. Am. Chem. Soc.* 136 (2014) 1730–1733.
- [88] S. Kumar, T. Surendar, B. Kumar, A. Baruah, V. Shanker, *RSC Adv.* 4 (2014) 8132.
- [89] G. Dong, Y. Zhang, Q. Pan, J. Qiu, *J. Photochem. Photobiol. C: Photochem. Rev.* 20 (2014) 33–50.
- [90] J. Yang, X. Wu, X. Li, Y. Liu, M. Gao, X. Liu, et al., *Appl. Phys. A* 105 (2011) 161–166.
- [91] Y. Wang, M.F. Ibad, H. Kosslick, J. Harloff, T. Beweries, J. Radnik, et al., *Microporous Mesoporous Mater.* 211 (2015) 182–191.
- [92] Q. Han, B. Wang, Y. Zhao, C. Hu, L. Qu, *Angew. Chem. Int. Ed.* 54 (2015) 11413–11437.
- [93] Y. Wang, J. Hong, W. Zhang, R. Xu, *Catal. Sci. Technol.* 3 (2013) 1703–1711.
- [94] D. Dontsova, S. Pronkin, M. Wehle, Z. Chen, C. Fettkenhauer, G. Clavel, et al., *Chem. Mater.* 27 (2015) 5170–5179.
- [95] M.J. Bojdys, J.-O. Muller, M. Antonietti, A. Thomas, *Chem. Eur. J.* 14 (2008) 8177–8182.
- [96] A. Sattler, S. Pagano, M. Zeuner, A. Zurawski, D. Gunzelmann, J. Senker, et al., *Chem. Eur. J.* 15 (2009) 13161–13170.
- [97] Y. Wang, X. Wang, M. Antonietti, *Angew. Chem. Int. Ed.* 51 (2012) 68–89.
- [98] Y. Gong, M. Li, H. Li, Y. Wang, *Green Chem.* 17 (2015) 715–736.
- [99] Y. Zheng, J. Liu, J. Liang, M. Jaroniec, S.Z. Qiao, *Energy Environ. Sci.* 5 (2012) 6717.
- [100] E. Kroke, M. Schwarz, E. Horath-Bordon, P. Kroll, B. Noll, A.D. Norman, *New J. Chem.* 26 (2002) 508–512.
- [101] X. Zhou, B. Jin, L. Li, F. Peng, H. Wang, H. Yu, et al., *J. Mater. Chem.* 22 (2012) 17900.
- [102] Q. Cai, J. Shen, Y. Feng, Q. Shen, H. Yang, *J. Alloys Compd.* 628 (2015) 372–378.
- [103] Q. Lin, L. Li, S. Liang, M. Liu, J. Bi, L. Wu, *Appl. Catal. B: Environ.* 163 (2015) 135–142.
- [104] S. Chen, C. Wang, B.R. Bunes, Y. Li, C. Wang, L. Zang, *Appl. Catal. A: Gen.* 498 (2015) 63–68.
- [105] Y. Cui, G. Zhang, Z. Lin, X. Wang, *Appl. Catal. B: Environ.* 181 (2015) 413–419.
- [106] X. Zhou, F. Peng, H. Wang, H. Yu, Y. Fang, *Chem. Commun.* 47 (2011) 10323–10325.
- [107] J. Zhang, S. Hu, Y. Wang, *RSC Adv.* 4 (2014) 62912–62919.
- [108] J. Di, J. Xia, S. Yin, H. Xu, M. He, H. Li, et al., *RSC Adv.* 3 (2013) 19624.
- [109] S. Dyjak, W. Kicinski, A. Huczko, *J. Mater. Chem. A* 3 (2015) 9621–9631.
- [110] X. Zhong, M. Jin, H. Dong, L. Liu, L. Wang, H. Yu, et al., *J. Solid State Chem.* 220 (2014) 54–59.
- [111] X.-S. Zhang, K. Tian, J.-Y. Hu, H. Jiang, *Chemosphere* 141 (2015) 127–133.
- [112] Z. Wang, W. Guan, Y. Sun, F. Dong, Y. Zhou, W.-K. Ho, *Nanoscale* 7 (2015) 2471–2479.

- [113] D. Chen, K. Wang, W. Hong, R. Zong, W. Yao, Y. Zhu, *Appl. Catal. B: Environ.* 166–167 (2015) 366–373.
- [114] B. Long, J. Lin, X. Wang, *J. Mater. Chem. A* 2 (2014) 2942.
- [115] S.-W. Bian, Z. Ma, W.-G. Song, *J. Phys. Chem. C* 113 (2009) 8668–8672.
- [116] D. Zheng, C. Pang, Y. Liu, X. Wang, *Chem. Commun.* 51 (2015) 9706–9709.
- [117] Y. Zhao, F. Zhao, X. Wang, C. Xu, Z. Zhang, G. Shi, et al., *Angew. Chem.* 126 (2014) 14154–14159.
- [118] P. Zhang, X. Li, C. Shao, Y. Liu, *J. Mater. Chem. A* 3 (2015) 3281–3284.
- [119] B. Yuan, Z. Chu, G. Li, Z. Jiang, T. Hu, Q. Wang, et al., *J. Mater. Chem. C* 2 (2014) 8212–8215.
- [120] L. Xu, J. Xia, L. Wang, H. Ji, J. Qian, H. Xu, et al., *Eur. J. Inorg. Chem.* (2014) 3665–3673.
- [121] X. Bai, C. Cao, X. Xu, *Mater. Sci. Eng. B* 175 (2010) 95–99.
- [122] X. Wu, C. Liu, X. Li, X. Zhang, C. Wang, Y. Liu, *Mater. Sci. Semicon. Proc.* 32 (2015) 76–81.
- [123] H.-J. Li, B.-W. Sun, L. Sui, D.-J. Qian, M. Chen, *Phys. Chem. Chem. Phys.* 17 (2015) 3309–3315.
- [124] Z. Zhao, Y. Dai, J. Lin, G. Wang, *Chem. Mater.* 26 (2014) 3151–3161.
- [125] H.-M. Zhao, C.-M. Di, L. Wang, Y. Chun, Q.-H. Xu, *Micropor. Mesopor. Mater.* 208 (2015) 98–104.
- [126] M. Zhang, J. Xu, R. Zong, Y. Zhu, *Appl. Catal. B: Environ.* 147 (2014) 229–235.
- [127] J. Xu, Y. Wang, Y. Zhu, *Langmuir* 29 (2013) 10566–10572.
- [128] P. Gibot, F. Schnell, D. Spitzer, *Microporous Mesoporous Mater.* 219 (2016) 42–47.
- [129] Z.P. Chen, M. Antonietti, D. Dontsova, *Chem. Eur. J.* 21 (2015) 10805–10811.
- [130] Z. Yang, A.E. Danks, J. Wang, Y. Zhang, Z. Schnepf, *APL Mater.* 4 (2016) 015706.
- [131] Z. Yang, Y. Zhang, Z. Schnepf, *J. Mater. Chem. A* 3 (2015) 14081–14092.
- [132] Z. Chen, P. Sun, B. Fan, Q. Liu, Z. Zhang, X. Fang, *Appl. Catal. B: Environ.* 170–171 (2015) 10–16.
- [133] W. Lu, T. Xu, Y. Wang, H. Hu, N. Li, X. Jiang, et al., *Appl. Catal. B: Environ.* 180 (2016) 20–28.
- [134] S. Hu, L. Ma, H. Wang, L. Zhang, Y. Zhao, G. Wu, *RSC Adv.* 5 (2015) 31947–31953.
- [135] H. Dai, S. Zhang, G. Xu, Y. Peng, L. Gong, X. Li, et al., *RSC Adv.* 4 (2014) 58226–58230.
- [136] F. He, G. Chen, Y. Yu, S. Hao, Y. Zhou, Y. Zheng, *ACS Appl. Mater. Interfaces* 6 (2014) 7171–7179.
- [137] Y. Sui, J. Liu, Y. Zhang, X. Tian, W. Chen, *Nanoscale* 5 (2013) 9150–9155.
- [138] L. Ge, C. Han, J. Liu, *J. Mater. Chem.* 22 (2012) 11843.
- [139] J. Xu, K.-Z. Long, Y. Wang, B. Xue, Y.-X. Li, *Appl. Catal. A: Gen.* 496 (2015) 1–8.
- [140] B. Yue, Q. Li, H. Iwai, T. Kako, J. Ye, *Sci. Technol. Adv. Mater.* 12 (2011) 034401.
- [141] A.S. Nair, R. Sundara, N. Anitha, *Int. J. Hydrogen Energy* 40 (2015) 3259–3267.
- [142] Q. Han, C. Hu, F. Zhao, Z. Zhang, N. Chen, L. Qu, *J. Mater. Chem. A* 3 (2015) 4612–4619.
- [143] C. Lu, R. Chen, X. Wu, M. Fan, Y. Liu, Z. Le, et al., *Appl. Surf. Sci.* 360 (2016) 1016–1022.
- [144] M. Zhang, X. Bai, D. Liu, J. Wang, Y. Zhu, *Appl. Catal. B: Environ.* 164 (2015) 77–81.
- [145] S. Hu, R. Jin, G. Lu, D. Liu, J. Gui, *RSC Adv.* 4 (2014) 24863.
- [146] Y. Wang, Y. Wang, Y. Li, H. Shi, Y. Xu, H. Qin, et al., *Catal. Commun.* 72 (2015) 24–28.
- [147] Y. Wang, Y. Xu, Y. Wang, H. Qin, X. Li, Y. Zuo, *Catal. Commun.* 74 (2016) 75–99.
- [148] R. Jin, S. Hu, J. Gui, D. Liu, *Bull. Korean Chem. Soc.* 36 (2015) 17–23.
- [149] Z. Li, J. Wang, K. Zhu, F. Ma, A. Meng, *Mater. Lett.* 145 (2015) 167–170.
- [150] Y. Fu, T. Huang, L. Zhang, J. Zhu, X. Wang, *Nanoscale* 7 (2015) 13723–13733.
- [151] M.J. Munoz-Batista, O. Fontelles-carceller, M. Ferrer, M. Fernández-garcía, A. Kubacka, *Appl. Catal. B: Environ.* 183 (2016) 86–95.
- [152] S. Ma, S. Zhan, Y. Jia, Q. Shi, Q. Zhou, *Appl. Catal. B: Environ.* 186 (2016) 77–87.
- [153] C. Liu, L. Wang, H. Xu, S. Wang, S. Gao, X. Ji, *Mater. Lett.* 164 (2016) 567–570.
- [154] O. Fontelles-Carceller, M.J. Munoz-Batista, M. Fernandez-Garcia, A. Kubacka, *ACS Appl. Mater. Interfaces* 8 (2016) 2617–2627.
- [155] L. Ge, C. Han, J. Liu, Y. Li, *Appl. Catal. A: Gen.* 409–410 (2011) 215–222.
- [156] Y. Yang, Y. Guo, F. Liu, X. Yuan, Y. Guo, S. Zhang, et al., *Appl. Catal. B: Environ.* 142–143 (2013) 828–837.
- [157] W. Bing, Z. Chen, H. Sun, P. Shi, N. Gao, J. Ren, et al., *Nano Res.* 8 (2015) 1648–1658.
- [158] X. Bai, R. Zong, C. Li, D. Liu, Y. Liu, Y. Zhu, *Appl. Catal. B: Environ.* 147 (2014) 82–91.
- [159] K. Tian, W.-J. Liu, H. Jiang, *ACS Sustain. Chem. Eng.* 3 (2015) 269–276.
- [160] J. Gao, J. Wang, X. Qian, Y. Dong, H. Xu, R. Song, et al., *J. Solid State Chem.* 228 (2015) 60–64.
- [161] J. Xue, S. Ma, Y. Zhou, Z. Zhang, M. He, *ACS Appl. Mater. Interfaces* 7 (2015) 9630–9637.
- [162] K. Li, Z. Zeng, L. Yan, S. Luo, X. Luo, M. Huo, et al., *Appl. Catal. B: Environ.* 165 (2015) 428–437.
- [163] N. Cheng, J. Tian, Q. Liu, C. Ge, A.H. Qusti, A.M. Asiri, et al., *ACS Appl. Mater. Interfaces* 5 (2013) 6815–6819.
- [164] S. Tonda, S. Kumar, V. Shanker, *Mater. Res. Bull.* 75 (2016) 51–58.
- [165] T. Bhowmik, M.K. Kundu, S. Barman, *RSC Adv.* 5 (2015) 38760–38773.
- [166] C. Chang, Y. Fu, M. Hu, C. Wang, G. Shan, L. Zhu, *Appl. Catal. B: Environ.* 142–143 (2013) 553–560.
- [167] F. Jiang, W. Tan, H. Chen, L. Tan, J. Liu, *RSC Adv.* 5 (2015) 51841–51851.
- [168] S. Bai, X. Wang, C. Hu, M. Xie, J. Jiang, Y. Xiong, *Chem. Commun.* 50 (2014) 6094–6097.
- [169] J. Yu, K. Wang, W. Xiao, B. Cheng, *Phys. Chem. Chem. Phys.* 16 (2014) 11492–11501.
- [170] X. Ma, Y. Lv, J. Xu, Y. Liu, R. Zhang, Y. Zhu, *J. Phys. Chem. C* 116 (2012) 23485–23493.
- [171] L. Zhang, X. Chen, J. Guan, Y. Jiang, T. Hou, X. Mu, *Mater. Res. Bull.* 48 (2013) 3485–3491.
- [172] S. Hu, L. Ma, J. You, F. Li, Z. Fan, F. Wang, et al., *RSC Adv.* 4 (2014) 21657.
- [173] Y. Zhou, L. Zhang, J. Liu, X. Fan, B. Wang, M. Wang, et al., *J. Mater. Chem. A* 3 (2015) 3862–3867.
- [174] K. Wang, Q. Li, B. Liu, B. Cheng, W. Ho, J. Yu, *Appl. Catal. B: Environ.* 176–177 (2015) 44–52.
- [175] Y. Li, S. Wu, L. Huang, J. Wang, H. Xu, H. Li, *Mater. Lett.* 137 (2014) 281–284.
- [176] B. Yang, H. Zhou, X. Zhang, M. Zhao, *J. Mater. Chem. C* 3 (2015) 10886–10891.
- [177] S.C. Yan, Z.S. Li, Z.G. Zou, *Langmuir* 26 (2010) 3894–3901.
- [178] G. Dong, Z. Ai, L. Zhang, *RSC Adv.* 4 (2014) 5553.
- [179] H. Ma, Y. Li, S. Li, N. Liu, *Appl. Surf. Sci.* 357 (2015) 131–138.
- [180] V.K.K. Upadhyayula, S. Deng, M.C. Mitchell, G.B. Smith, *Sci. Total Environ.* 408 (2009) 1–13.
- [181] X. Ren, C. Chen, M. Nagatsu, X. Wang, *Chem. Eng. J.* 170 (2011) 395–410.
- [182] D. Chen, H. Zhang, Y. Liu, J. Li, *Energy Environ. Sci.* 6 (2013) 1362.
- [183] S. Bai, X. Shen, *RSC Adv.* 2 (2012) 64.
- [184] G. Liao, S. Chen, X. Quan, H. Yu, H. Zhao, *J. Mater. Chem.* 22 (2012) 2721.
- [185] B. Ai, X. Duan, H. Sun, X. Qiu, S. Wang, *Catal. Today* 258 (2015) 668–675.
- [186] W.-J. Ong, L.-L. Tan, S.-P. Chai, S.-T. Yong, *Chem. Commun.* 51 (2015) 858–861.
- [187] W.-J. Ong, L.-L. Tan, S.-P. Chai, S.-T. Yong, A.R. Mohamed, *Nano Energy* 13 (2015) 757–770.
- [188] A. Du, S. Sanvito, Z. Li, D. Wang, Y. Jiao, T. Liao, et al., *J. Am. Chem. Soc.* 134 (2012) 4393–4397.
- [189] F. Jiang, T. Yan, H. Chen, A. Sun, C. Xu, X. Wang, *Appl. Surf. Sci.* 295 (2014) 164–172.
- [190] L. Ge, C. Han, *Appl. Catal. B: Environ.* 117–118 (2012) 268–274.
- [191] A. Suryawanshi, P. Dhanasekaran, D. Mhamane, S. Kelkar, S. Patil, N. Gupta, et al., *Int. J. Hydrogen Energy* 37 (2012) 9584–9589.
- [192] Y. Xu, H. Xu, L. Wang, J. Yan, H. Li, Y. Song, et al., *Dalton Trans.* 42 (2013) 7604–7613.
- [193] Q. Yu, J. Xu, C. Wu, L. Guan, *RSC Adv.* 5 (2015) 65303–65307.
- [194] S.S. Shinde, A. Sami, J. Lee, *Carbon* 96 (2016) 929–936.
- [195] Y. Guo, P. Yao, D. Zhu, C. Gu, *J. Mater. Chem. A* 3 (2015) 13189–13192.
- [196] S. Fang, Y. Xia, K. Lv, Q. Li, J. Sun, M. Li, *Appl. Catal. B: Environ.* 185 (2016) 225–232.
- [197] H. Sun, G. Zhou, Y. Wang, A. Suvorova, S. Wang, *ACS Appl. Mater. Interfaces* 6 (2014) 16745–16754.
- [198] B. Chai, X. Liao, F. Song, H. Zhou, *Dalton Trans.* 43 (2014) 982–989.
- [199] X. Bai, L. Wang, Y. Wang, W. Yao, Y. Zhu, *Appl. Catal. B: Environ.* 152–153 (2014) 262–270.
- [200] L. Pi, R. Jiang, W. Zhou, H. Zhu, W. Xiao, D. Wang, et al., *Appl. Surf. Sci.* 358 (2015) 231–239.
- [201] Z. Zhao, Y. Dai, J. Mater. Chem. A 2 (2014) 13442–13451.
- [202] Q. Yu, S. Guo, X. Li, M. Zhang, *Russian J. Phys. Chem. A* 88 (2014) 1643–1649.
- [203] Z. Tong, D. Yang, T. Xiao, Y. Tian, Z. Jiang, *Chem. Eng. J.* 260 (2015) 117–125.
- [204] G. Li, X. Nie, Y. Gao, T. An, *Appl. Catal. B: Environ.* 180 (2016) 726–732.
- [205] Z. Huang, Q. Sun, K. Lv, Z. Zhang, M. Li, B. Li, *Appl. Catal. B: Environ.* 164 (2015) 420–427.
- [206] J. Ma, C. Wang, H. He, *Appl. Catal. B: Environ.* 184 (2016) 28–34.
- [207] X. Song, Y. Hu, M. Zheng, C. Wei, *Appl. Catal. B: Environ.* 182 (2016) 587–597.
- [208] T. Giannakopoulou, I. Papailias, N. Todorova, N. Boukos, Y. Liu, J. Yu, et al., *Chem. Eng. J.* (2016), <http://dx.doi.org/10.1016/j.cej.2015.12.102>.
- [209] F. Dong, Z. Wang, Y. Li, W.-K. Ho, S.C. Lee, *Environ. Sci. Technol.* 48 (2014) 10345–10353.
- [210] K. Sridharan, E. Jang, T.J. Park, *Appl. Catal. B: Environ.* 142–143 (2013) 718–728.
- [211] R. Mohini, N. Lakshminarasimhan, *Mater. Res. Bull.* 76 (2016) 370–375.
- [212] Y. Zang, Y. Zuo, G. Li, *J. Mater. Chem. A* 2 (2014) 15774.
- [213] S. Ma, J. Xue, Y. Zhou, Z. Zhang, Z. Cai, D. Zhu, et al., *RSC Adv.* 5 (2015) 64976–64982.
- [214] J. Lei, Y. Chen, L. Wang, *J. Mater. Sci.* 50 (2015) 3467–3476.
- [215] Y. Li, J. Wang, Y. Yang, Y. Zhang, D. He, Q. An, et al., *J. Hazard. Mater.* 292 (2015) 79–89.
- [216] W.-K. Jo, T.S. Natarajan, *Chem. Eng. J.* 281 (2015) 549–565.
- [217] H. Li, L. Zhou, L. Wang, Y. Liu, J. Lei, J. Zhang, *Phys. Chem. Chem. Phys.* 17 (2015) 17406–17412.
- [218] J. Zhang, Y. Wang, S. Hu, *Bull. Korean Chem. Soc.* 36 (2015) 333–339.
- [219] Z. Jiang, C. Zhu, W. Wan, K. Qian, *J. Mater. Chem. A* 4 (2016) 1806–1818.
- [220] J. Lei, Y. Chen, F. Shen, L. Wang, Y. Liu, J. Zhang, *J. Alloys Compd.* 631 (2015) 328–334.
- [221] F. Raziq, C. Li, M. Humayun, Y. Qu, A. Zada, H. Yu, et al., *Mater. Res. Bull.* 70 (2015) 494–499.
- [222] D. Fu, G. Han, F. Liu, Y. Xiao, H. Wang, R. Liu, et al., *Mater. Sci. Semicon. Proc.* 27 (2014) 966–974.
- [223] C. Miranda, H. Mansilla, J. Yanez, S. Obregon, G. Colon, *J. Photochem. Photobiol. A: Chem.* 253 (2013) 16–21.

- [224] L. Zhang, D. Jing, X. She, H. Liu, D. Yang, Y. Lu, et al., *J. Mater. Chem. A* 2 (2014) 2071.
- [225] L. Gu, J. Wang, Z. Zou, X. Han, J. Hazard. Mater. 268 (2014) 216–223.
- [226] F. Chang, J. Zhang, Y. Xie, J. Chen, C. Li, J. Wang, et al., *Appl. Surf. Sci.* 311 (2014) 574–581.
- [227] G. Song, Z. Chu, W. Jin, H. Sun, *Chinese J. Chem. Eng.* 23 (2015) 1326–1334.
- [228] M.J. Munoz-Batista, A. Kubacka, M. Fernandez-Garcia, *Catal. Sci. Technol.* 4 (2014) 2006.
- [229] X. Li, M. Li, J. Yang, X. Li, T. Hu, J. Wang, et al., *J. Phys. Chem. Solids* 75 (2014) 441–446.
- [230] Y. Wang, R. Shi, J. Lin, Y. Zhu, *Energy Environ. Sci.* 4 (2011) 2922.
- [231] J.-X. Sun, Y.-P. Yuan, L.-G. Qiu, X. Jiang, A.-J. Xie, Y.-H. Shen, et al., *Dalton Trans.* 41 (2012) 6756.
- [232] J. Zhou, M. Zhang, Y. Zhu, *Phys. Chem. Chem. Phys.* 16 (2014) 17627–17633.
- [233] S. Pande, P. Fageria, R. Nazir, S. Gangopadhyay, H. Barshilia, *RSC Adv.* 5 (2015) 80397–80409.
- [234] K. Vignesh, S. Kang, B.S. Kwak, M. Kang, *Sep. Purif. Technol.* 147 (2015) 257–265.
- [235] W. Yu, D. Xu, T. Peng, *J. Mater. Chem. A* 3 (2015) 19936–19947.
- [236] Y. He, Y. Wang, L. Zhang, B. Teng, M. Fan, *Appl. Catal. B: Environ.* 168–169 (2015) 1–8.
- [237] S. Kumar, T. Surendar, A. Baruah, V. Shanker, *J. Mater. Chem. A* 1 (2013) 5333–5340.
- [238] F.J. Zhang, F.Z. Xie, S.F. Zhu, J. Liu, J. Zhang, S.F. Mei, et al., *Chem. Eng. J.* 228 (2013) 435–441.
- [239] X. Chen, X. Huang, Z. Yi, *Chem. Eur. J.* 20 (2014) 17590–17596.
- [240] S. Meng, X. Ning, T. Zhang, S.-F. Chen, X. Fu, *Phys. Chem. Chem. Phys.* 17 (2015) 11577–11585.
- [241] Y. Li, L. Fang, R. Jin, Y. Yang, X. Fang, Y. Xing, et al., *Nanoscale* 7 (2015) 758–764.
- [242] L. Shi, L. Liang, F. Wang, M. Liu, J. Sun, *J. Mater. Sci.* 50 (2015) 1718–1727.
- [243] S. Tonda, S. Kumar, V. Shanker, *J. Environ. Chem. Eng.* 3 (2015) 852–861.
- [244] N. Tian, H. Huang, Y. He, Y. Guo, Y. Zhang, *Colloids Surf. A: Physicochem. Eng. Asp.* 467 (2015) 188–194.
- [245] K. Wu, Y. Cui, X. Wei, X. Song, J. Huang, *J. Saudi Chem. Soc.* 19 (2015) 465–470.
- [246] Y. Feng, J. Shen, Q. Cai, H. Yang, Q. Shen, *New J. Chem.* 39 (2015) 1132–1138.
- [247] H. Xu, J. Yan, Y. Xu, Y. Song, H. Li, J. Xia, et al., *Appl. Catal. B: Environ.* 129 (2013) 182–193.
- [248] W.-J. Ong, L.K. Putri, L.-L. Tan, S.-P. Chai, S.-T. Yong, *Appl. Catal. B: Environ.* 180 (2016) 530–543.
- [249] L. Liu, Y. Qi, J. Yang, W. Cui, X. Li, Z. Zhang, *Appl. Surf. Sci.* 358 (2015) 319–327.
- [250] R.M. Mohamed, *Ceram. Int.* 41 (2015) 1197–1204.
- [251] L.K. Putri, W.-J. Ong, W.S. Chang, S.-P. Chai, *Catal. Sci. Technol.* 6 (2015) 744–754.
- [252] S. Ma, J. Xue, Y. Zhou, Z. Zhang, *RSC Adv.* 5 (2015) 40000–40006.
- [253] M. Xu, L. Han, S. Dong, *ACS Appl. Mater. Interfaces* 5 (2013) 12533–12540.
- [254] K. Vignesh, M. Kang, *Mater. Sci. Eng. B* 199 (2015) 30–36.
- [255] H. Shi, C. Zhang, C. Zhou, *RSC Adv.* 5 (2015) 50146–50154.
- [256] S. Ye, L.-G. Qiu, Y.-P. Yuan, Y.-J. Zhu, J. Xia, J.-F. Zhu, *J. Mater. Chem. A* 1 (2013) 3008.
- [257] X. Zhou, B. Jin, R. Chen, F. Peng, Y. Fang, *Mater. Res. Bull.* 48 (2013) 1447–1452.
- [258] S. Kumar, T. Surendar, B. Kumar, A. Baruah, V. Shanker, *J. Phys. Chem. C* 117 (2013) 26135–26143.
- [259] X. Liu, A. Jin, Y. Jia, J. Jiang, N. Hu, X. Chen, *RSC Adv.* 5 (2015) 92033–92041.
- [260] J. Theerthagiri, R.A. Senthil, A. Priya, J. Madhavan, R.J.V. Michael, M. Ashokkumar, *RSC Adv.* 4 (2014) 38222.
- [261] Y. Yao, F. Lu, Y. Zhu, F. Wei, X. Liu, C. Lian, et al., *J. Hazard. Mater.* 297 (2015) 224–233.
- [262] H. Ji, X. Jing, Y. Xu, J. Yan, H. Li, Y. Li, et al., *RSC Adv.* 5 (2015) 57960–57967.
- [263] Y. Yao, Y. Cai, F. Lu, J. Qin, F. Wei, C. Xu, et al., *Ind. Eng. Chem. Res.* 53 (2014) 17294–17302.
- [264] J. Fu, B. Chang, Y. Tian, F. Xi, X. Dong, *J. Mater. Chem. A* 1 (2013) 3083.
- [265] Y. Xu, W.-D. Zhang, *Eur. J. Inorg. Chem.* (2015) 1744–1751.
- [266] D. Wang, Z. Xu, Q. Luo, X. Li, J. An, R. Yin, et al., *J. Mater. Sci.* 51 (2016) 893–902.
- [267] M. Lu, Z. Pei, S. Weng, W. Feng, Z. Fang, Z. Zheng, et al., *Phys. Chem. Chem. Phys.* 16 (2014) 21280–21288.
- [268] L. Zhang, F. Huang, C. Liang, L. Zhou, X. Zhang, Q. Pang, *J. Taiwan Inst. Chem. Eng.* 000 (2015) 1–8, <http://dx.doi.org/10.1016/j.jtice.2015.11.013>.
- [269] L. Lei, H. Jin, Q. Zhang, J. Xu, D. Gao, Z. Fu, *Dalton Trans.* 44 (2015) 795–803.
- [270] Y. Bai, P.-Q. Wang, J.-Y. Liu, X.-J. Liu, *RSC Adv.* 4 (2014) 19456.
- [271] Y. Yang, F. Zhou, S. Zhan, Y. Liu, Y. Yin, *J. Inorg. Organomet. Polym. Mater.* 26 (2016) 91–99.
- [272] Q. Li, X. Zhao, J. Yang, C.-J. Jia, Z. Jin, W. Fan, *Nanoscale* 7 (2015) 18971–18983.
- [273] S. Shi, M.A. Gondal, A.A. Al-Saadi, R. Fajgar, J. Kupcik, X. Chang, et al., *J. Colloid Interface Sci.* 416 (2014) 212–219.
- [274] X.J. Wang, Q. Wang, F.T. Li, W.Y. Yang, Y. Zhao, Y.J. Hao, et al., *Chem. Eng. J.* 234 (2013) 361–371.
- [275] M. He, D. Zhao, J. Xia, L. Xu, J. Di, H. Xu, et al., *Mater. Sci. Semicon. Proc.* 32 (2015) 117–124.
- [276] L. Ye, J. Liu, Z. Jiang, T. Peng, L. Zan, *Appl. Catal. B: Environ.* 142–143 (2013) 1–7.
- [277] Z. Yang, J. Li, F. Cheng, Z. Chen, X. Dong, *J. Alloys Compd.* 634 (2015) 215–222.
- [278] Y. Sun, W. Zhang, T. Xiong, Z. Zhao, F. Dong, R. Wang, *J. Colloid Interface Sci.* 418 (2014) 317–323.
- [279] C. Chang, L. Zhu, S. Wang, X. Chu, L. Yue, *ACS Appl. Mater. Interfaces* 6 (2014) 5083–5093.
- [280] W. Wang, H. Cheng, B. Huang, X. Liu, X. Qin, X. Zhang, et al., *J. Colloid Interface Sci.* 442 (2015) 97–102.
- [281] N. Tian, H. Huang, Y. He, Y. Guo, Y. Zhang, *RSC Adv.* 4 (2014) 42716–42722.
- [282] J. Sun, J. Song, M.A. Gondal, S. Shi, Z. Lu, Q. Xu, et al., *Res. Chem. Intermed.* (2014) 6941–6955.
- [283] J.-C. Wang, H.-C. Yao, Z.-Y. Fan, L. Zhang, J.-S. Wang, S.-Q. Zang, et al., *ACS Appl. Mater. Interfaces* (2016), <http://dx.doi.org/10.1021/acsami.5b09901>.
- [284] N. Tian, H. Huang, Y. Guo, Y. He, *Appl. Surf. Sci.* 322 (2014) 249–254.
- [285] M. Xiong, L. Chen, Q. Yuan, J. He, S.-L. Luo, C.-T. Au, et al., *Dalton Trans.* 43 (2014) 8331–8337.
- [286] Q. Zhang, H. Wang, S. Hu, G. Lu, J. Bai, X. Kang, et al., *RSC Adv.* 5 (2015) 42736–42743.
- [287] M. Ou, Q. Zhong, S. Zhang, *J. Sol-Gel Sci. Technol.* 72 (2014) 443–454.
- [288] M. Yang, X. Jin, J. Wuhan Univ. Technol. Mater. Sci. Ed. 30 (2015) 217–222.
- [289] Y. Ji, J. Cao, L. Jiang, Y. Zhang, Z. Yi, *J. Alloys Compd.* 590 (2014) 9–14.
- [290] C. Li, S. Wang, T. Wang, Y. Wei, P. Zhang, J. Gong, *Small* 10 (2014) 2783–2790.
- [291] H. Li, J. Liu, W. Hou, N. Du, R. Zhang, X. Tao, *Appl. Catal. B: Environ.* 160–161 (2014) 89–97.
- [292] J. Lv, K. Dai, J. Zhang, L. Geng, C. Liang, Q. Liu, et al., *Appl. Surf. Sci.* 358 (2015) 377–384.
- [293] T. Yan, Q. Yan, X. Wang, H. Liu, M. Li, S. Lu, et al., *Dalton Trans.* 44 (2015) 1601–1611.
- [294] J. Zhang, Y. Hu, X. Jiang, S. Chen, S. Meng, X. Fu, *J. Hazard. Mater.* 280 (2014) 713–722.
- [295] M. Xiong, L. Chen, Q. Yuan, J. He, S.-L. Luo, C.-T. Au, et al., *Carbon* 86 (2015) 217–224.
- [296] N. Tian, Y. Zhang, C. Liu, S. Yu, M. Li, H. Huang, *RSC Adv.* 6 (2016) 10895–10903.
- [297] H. Wang, J. Lu, F. Wang, W. Wei, Y. Chang, S. Dong, *Ceram. Int.* 40 (2014) 9077–9086.
- [298] L. Ge, C. Han, J. Liu, *Appl. Catal. B: Environ.* 108–109 (2011) 100–107.
- [299] L. Liu, Y. Qi, J. Lu, S. Lin, W. An, J. Hu, et al., *RSC Adv.* 5 (2015) 99339–99346.
- [300] X. Rong, F. Qiu, J. Yan, H. Zhao, X. Zhu, D. Yang, *RSC Adv.* 5 (2015) 24944–24952.
- [301] Z. Xuan, Y. Shiyue, L. Yumei, W. Zuoshan, L. Weifeng, *Mater. Lett.* 145 (2015) 23–26.
- [302] X. Wang, W. Mao, J. Zhang, Y. Han, C. Quan, Q. Zhang, et al., *J. Colloid Interface Sci.* 448 (2015) 17–23.
- [303] S. Zhang, Y. Yang, Y. Guo, W. Guo, M. Wang, Y. Guo, et al., *J. Hazard. Mater.* 261 (2013) 235–245.
- [304] C. Zhao, G. Tan, J. Huang, W. Yang, H. Ren, A. Xia, *ACS Appl. Mater. Interfaces* 7 (2015) 23949–23957.
- [305] F. Dong, Z. Ni, P. Li, *New J. Chem.* 39 (2015) 4737–4744.
- [306] Z. Zhang, M. Xu, W. Ho, X. Zhang, Z. Yang, X. Wang, *Appl. Catal. B: Environ.* 184 (2016) 174–181.
- [307] G. Dong, L. Zhang, *J. Phys. Chem. C* 117 (2013) 4062–4068.
- [308] K.I. Katsumata, R. Motoyoshi, N. Matsushita, K. Okada, *J. Hazard. Mater.* 260 (2013) 475–482.
- [309] S.W. Cao, X.F. Liu, Y.P. Yuan, Z.Y. Zhang, Y.S. Liao, J. Fang, et al., *Appl. Catal. B: Environ.* 147 (2014) 940–946.
- [310] C. Pan, J. Xu, Y. Wang, D. Li, Y. Zhu, *Adv. Funct. Mater.* 22 (2012) 1518–1524.
- [311] D. Chen, K. Wang, D. Xiang, R. Zong, W. Yao, Y. Zhu, *Appl. Catal. B: Environ.* 147 (2014) 554–561.
- [312] J. Chen, Y. Chen, J. Fu, *RSC Adv.* 6 (2016) 2323–2336.
- [313] Z. Zhang, D. Jiang, D. Li, M. He, M. Chen, *Appl. Catal. B: Environ.* 183 (2016) 113–123.
- [314] M. Li, L.L. Zhang, M. Wu, Y. Du, X. Fan, M. Wang, et al., *Nano Energy* 19 (2016) 145–155.
- [315] Y. Liu, P. Chen, Y. Chen, H. Lu, J. Wang, Z. Yang, et al., *RSC Adv.* 6 (2016) 10802–10809.
- [316] P. Qiu, H. Chen, F. Jiang, *RSC Adv.* 4 (2014) 39969.
- [317] Z. Jin, N. Murakami, T. Tsubota, T. Ohno, *Appl. Catal. B: Environ.* 150–151 (2014) 479–485.
- [318] Z. Zhang, D. Jiang, D. Li, M. He, M. Chen, *Appl. Catal. B: Environ.* 183 (2016) 113–123.
- [319] X. She, H. Xu, H. Wang, J. Xia, Y. Song, J. Yan, et al., *Dalton Trans.* 44 (2015) 7021–7031.
- [320] C. Chen, Y. Zhou, N. Wang, L. Cheng, H. Ding, *RSC Adv.* 5 (2015) 95523–95531.
- [321] Y. He, J. Cai, T. Li, Y. Wu, H. Lin, L. Zhao, et al., *Chem. Eng. J.* 215–216 (2013) 721–730.
- [322] T. Xian, H. Yang, L.J. Di, J.F. Dai, *J. Alloys Compd.* 622 (2015) 1098–1104.
- [323] Y. He, L. Zhang, X. Wang, Y. Wu, H. Lin, L. Zhao, et al., *RSC Adv.* 4 (2014) 13610.
- [324] L. Zhang, X. Wang, Q. Nong, H. Lin, B. Teng, Y. Zhang, et al., *Appl. Surf. Sci.* 329 (2015) 143–149.
- [325] J. Wang, P. Guo, Q. Guo, P.G. Jonsson, Z. Zhao, *CrystEngComm* 16 (2014) 4485.
- [326] H. Liu, Z. Jin, Z. Xu, Z. Zhang, D. Ao, *RSC Adv.* 5 (2015) 97951–97961.
- [327] B. Lin, C. Xue, X. Yan, G. Yang, G. Yang, B. Yang, *Appl. Surf. Sci.* 357 (2015) 346–355.

- [328] C. Wen, H. Zhang, Q. Bo, T. Huang, Z. Lu, J. Lv, et al., *Chem. Eng. J.* 270 (2015) 405–410.
- [329] J. Zhao, Z. Ji, X. Shen, H. Zhou, L. Ma, *Ceram. Int.* 41 (2015) 5600–5606.
- [330] H. Liu, Z. Jin, Z. Xu, *Dalton Trans.* 44 (2015) 14368–14375.
- [331] C. Xing, Z. Wu, D. Jiang, M. Chen, *J. Colloid Interface Sci.* 433 (2014) 9–15.
- [332] H.-Y. Chen, L.-G. Qiu, J.-D. Xiao, S. Ye, X. Jiang, Y.-P. Yuan, *RSC Adv.* 4 (2014) 22491.
- [333] Y. Hong, Y. Jiang, C. Li, W. Fan, X. Yan, M. Yan, et al., *Appl. Catal. B: Environ.* 180 (2016) 663–673.
- [334] X. Cui, F. Zheng, Y. Yin, X. Chun, *Phys. Chem. Chem. Phys.* 17 (2015) 29354–29362.
- [335] Q. Liu, C. Fan, H. Tang, X. Sun, J. Yang, X. Cheng, *Appl. Surf. Sci.* 358 (2015) 188–195.
- [336] H. Wang, X. Yuan, H. Wang, X. Chen, Z. Wu, L. Jiang, et al., *RSC Adv.* 5 (2015) 95643–95648.
- [337] X. Zhang, L. Wang, Q. Du, Z. Wang, S. Ma, M. Yu, *J. Colloid Interface Sci.* 464 (2016) 89–95.
- [338] Y. Zang, L. Li, X. Li, R. Lin, G. Li, *Chem. Eng. J.* 246 (2014) 277–286.
- [339] X. Wang, L. Zhang, H. Lin, Q. Nong, Y. Wu, T. Wu, et al., *RSC Adv.* 4 (2014) 40029–40035.
- [340] C. Song, M. Fan, B. Hu, T. Chen, L. Wang, W. Shi, *CrystEngComm* 3 (2015) 4575–4583.
- [341] T. Jayaraman, S. Arumugam Raja, A. Priya, M. Jagannathan, M. Ashokkumar, *New J. Chem.* 39 (2015) 1367–1374.
- [342] Q. Wang, Y. Shi, Z. Du, J. He, J. Zhong, L. Zhao, et al., *Eur. J. Inorg. Chem.* 2015 (2015) 4108–4115.
- [343] Z. Zhang, J. Huang, M. Zhang, Q. Yuan, B. Dong, *Appl. Catal. B: Environ.* 163 (2015) 298–305.
- [344] Q. Liu, J. Ding, Y. Chai, J. Zhao, S. Cheng, B. Zong, et al., *J. Environ. Chem. Eng.* 3 (2015) 1072–1080.
- [345] Q. Wang, L. Zheng, Y. Bai, J. Zhao, F. Wang, R. Zhang, et al., *Appl. Surf. Sci.* 347 (2015) 602–609.
- [346] Y. He, L. Zhang, M. Fan, X. Wang, M.L. Walbridge, Q. Nong, et al., *Solar Energy Mater. Solar C* 137 (2015) 175–184.
- [347] Y. Wu, S. Chen, J. Zhao, X. Yue, W. Deng, Y. Li, et al., *J. Environ. Chem. Eng.* 4 (2015) 797–807.
- [348] C. Han, Y. Wang, Y. Lei, B. Wang, N. Wu, Q. Shi, et al., *Nano Res.* 8 (2015) 1199–1209.
- [349] X. Wang, W. Yang, F. Li, Y. Xue, R. Liu, Y. Hao, et al., *Ind. Eng. Chem. Res.* 52 (2013) 17140–17150.
- [350] W. Li, C. Li, B. Chen, X. Jiao, D. Chen, *RSC Adv.* 5 (2015) 34281–34291.
- [351] S. Zhou, Y. Liu, J. Li, Y. Wang, G. Jiang, Z. Zhao, et al., *Appl. Catal. B: Environ.* 158–159 (2014) 20–29.
- [352] Y.P. Zhu, M. Li, Y.L. Liu, T.Z. Ren, Z.Y. Yuan, *J. Phys. Chem. C* 118 (2014) 10963–10971.
- [353] K. Kondo, N. Murakami, C. Ye, T. Tsubota, T. Ohno, *Appl. Catal. B: Environ.* 142–143 (2013) 362–367.
- [354] S. Xue, X. Hou, W. Xie, X. Wei, D. He, *Mater. Lett.* 161 (2015) 640–643.
- [355] J. Luo, X. Zhou, L. Ma, X. Xu, *RSC Adv.* 5 (2015) 68728–68735.
- [356] K. Dai, L. Lu, C. Liang, Q. Liu, G. Zhu, *Appl. Catal. B: Environ.* 156–157 (2014) 331–340.
- [357] S. Kumar, S. Tonda, A. Baruah, B. Kumar, V. Shanker, *Dalton Trans.* 43 (2014) 16105–16114.
- [358] S. Sun, M. Sun, Y. Fang, Y. Wang, H. Wang, *RSC Adv.* 6 (2016) 13063–13071.
- [359] W. Chen, T. Liu, T. Huang, X. Liu, X. Yang, *Nanoscale* 8 (2016) 3711–3719.
- [360] S. Kumar, A. Baruah, S. Tonda, B. Kumar, V. Shanker, B. Sreedhar, *Nanoscale* 6 (2014) 4830–4842.
- [361] W. Zhao, Y. Guo, S. Wang, H. He, C. Sun, S. Yang, *Appl. Catal. B: Environ.* 165 (2015) 335–343.
- [362] Y. Yang, W. Guo, Y. Guo, Y. Zhao, X. Yuan, Y. Guo, *J. Hazard. Mater.* 271 (2014) 150–159.
- [363] Y. Wang, J. Liu, Y. Wang, C. Fan, G. Ding, *Mater. Sci. Semicon. Proc.* 25 (2014) 1–7.
- [364] X. Yao, X. Liu, X. Hu, *ChemCatChem* 6 (2014) 3409–3418.
- [365] S. Kang, Y. Fang, Y. Huang, L.-F. Cui, Y. Wang, H. Qin, et al., *Appl. Catal. B: Environ.* 168 (2015) 472–482.
- [366] Y. Bao, K. Chen, *Nano-Micro Lett.* (2015), <http://dx.doi.org/10.1007/s40820-015-0076-y>.
- [367] J. Xue, S. Ma, Y. Zhou, Z. Zhang, X. Liu, *RSC Adv.* 5 (2015) 58738–58745.
- [368] R.C. Pawar, Y. Pyo, S.H. Ahn, C.S. Lee, *Appl. Catal. B: Environ.* 176–177 (2015) 654–666.
- [369] Z. Jiang, J. Xie, *RSC Adv.* 6 (2016) 3186–3197.
- [370] S. Vadiel, V.P. Kamalakannan, N.P. Kavitha, T.S. Priya, N. Balasubramanian, *Mater. Sci. Semicon. Proc.* 41 (2016) 59–66.
- [371] K. Yang, C. Meng, L. Lin, X. Peng, X. Chen, X. Wang, et al., *Catal. Sci. Technol.* 6 (2016) 829–839.
- [372] Z. Zhu, Z. Lu, D. Wang, X. Tang, Y. Yan, W. Shi, et al., *Appl. Catal. B: Environ.* 182 (2016) 115–122.
- [373] H. Shi, C. Zhang, G. Chen, *RSC Adv.* 5 (2015) 93615–93622.
- [374] M. Zang, L. Shi, L. Liang, D. Li, J. Sun, *RSC Adv.* 5 (2015) 56136–56144.
- [375] S.P. Adhikari, H.R. Pant, J.H. Kim, H.J. Kim, C.H. Park, C.S. Kim, *Colloids Surf. A: Physicochem. Eng. Asp.* 482 (2015) 477–484.
- [376] W. Liao, M. Murugananthan, Y. Zhang, *Phys. Chem. Chem. Phys.* 17 (2015) 8877–8884.
- [377] X. Xin, J. Lang, T. Wang, Y. Su, Y. Zhao, X. Wang, *Appl. Catal. B: Environ.* 181 (2016) 197–209.
- [378] M. Yang, X. Jin, J. Wuhan Univ. Technol. Mater. Sci. Ed. 29 (2014) 1111–1116.
- [379] D. Lu, G. Zhang, Z. Wan, *Appl. Surf. Sci.* 358 (2015) 223–230.
- [380] S.W. Hu, L.W. Yang, Y. Tian, X.L. Wei, J.W. Ding, J.X. Zhong, et al., *Appl. Catal. B: Environ.* 163 (2015) 611–622.
- [381] W.-K. Jo, N. Clament, S. Selvam, *J. Hazard. Mater.* 299 (2015) 462–470.
- [382] N. Wang, Y. Zhou, C. Chen, L. Cheng, H. Ding, *Catal. Commun.* 73 (2016) 74–79.
- [383] R.C. Pawar, V. Khare, C.S. Lee, *Dalton Trans.* 43 (2014) 12514.
- [384] S.W. Hu, L.W. Yang, Y. Tian, X.L. Wei, J.W. Ding, J.X. Zhong, et al., *J. Colloid Interface Sci.* 431 (2014) 42–49.
- [385] D. Ma, J. Wu, M. Gao, Y. Xin, T. Ma, Y. Sun, *Chem. Eng. J.* 290 (2016) 136–146.
- [386] X. Lü, J. Shen, J. Wang, Z. Cui, J. Xie, *RSC Adv.* 5 (2015) 15993–15999.
- [387] Q. Liu, Y. Guo, Z. Chen, Z. Zhang, X. Fang, *Appl. Catal. B: Environ.* 183 (2016) 231–241.
- [388] W. Wang, J.C. Yu, D. Xia, P.K. Wong, Y. Li, *Environ. Sci. Technol.* 47 (2013) 8724–8732.
- [389] Y. Hou, Z. Wen, S. Cui, X. Guo, J. Chen, *Adv. Mater.* 25 (2013) 6291–6297.
- [390] H.-T. Ren, S.-Y. Jia, S.-H. Wu, T.-H. Zhang, X. Han, *Mater. Lett.* 142 (2015) 15–18.
- [391] M.J. Muñoz-Batista, M. Fernández-García, A. Kubacka, *Appl. Catal. B: Environ.* 164 (2015) 261–270.
- [392] A. Akhundi, A. Habibi-Yangjeh, *Appl. Surf. Sci.* 358 (2015) 261–269.
- [393] A. Akhundi, A. Habibi-Yangjeh, *Ceram. Int.* 41 (2015) 5634–5643.
- [394] M. Mousavi, A. Habibi-yangjeh, *J. Colloid Interface Sci.* 465 (2016) 83–92.
- [395] A. Akhundi, A. Habibi-Yangjeh, *Mater. Sci. Semicon. Proc.* 39 (2015) 162–171.
- [396] M. Mousavi, A. Habibi-Yangjeh, *Mater. Chem. Phys.* 163 (2015) 421–430.
- [397] K. Vignesh, A. Suganthi, B.-K. Min, M. Kang, *J. Mol. Catal. A: Chem.* 395 (2014) 373–383.
- [398] A. Habibi-yangjeh, A. Akhundi, *J. Mol. Catal. A: Chem.* 415 (2016) 122–130.